

ONSET VOLTAGE HASH AND ANODE SPOTS IN  
QUASI-STEADY MAGNETOPLASMA DYNAMIC  
THRUSTERS

LUKE URIBARRI

A DISSERTATION

PRESENTED TO THE FACULTY  
OF PRINCETON UNIVERSITY  
IN CANDIDACY FOR THE DEGREE  
OF DOCTOR OF PHILOSOPHY

RECOMMENDED FOR ACCEPTANCE  
BY THE DEPARTMENT OF  
MECHANICAL AND AEROSPACE ENGINEERING  
ADVISOR: EDGAR Y. CHOEIRI

NOVEMBER 2008

ONSET VOLTAGE HASH AND ANODE SPOTS IN  
QUASI-STEADY MAGNETOPLASMDYNAMIC  
THRUSTERS

Prepared by:

---

Luke Uribarri

Approved by:

---

Professor Edgar Choueiri  
Dissertation Advisor

---

Professor Emeritus Robert G. Jahn  
Dissertation Reader

---

Dr. Stewart Zweben  
Dissertation Reader

© Copyright by Luke Uribarri, 2008.

All Rights Reserved

# Abstract

An experimental investigation of the voltage noise (“hash”) and anode damage in a self-field, quasi-steady magnetoplasmadynamic thruster (MPDT) operating above onset is presented. “Onset” refers to an operating mode of the MPDT that occurs at high currents  $J$  and low mass flow rates  $\dot{m}$ , or equivalently at high  $J^2/\dot{m}$ , which is characterized by noisy, unrepeatable operation and which represents a performance ceiling for this particular plasma thruster.

Careful measurements of the thruster voltage are made while operating the thruster over a range of  $J^2/\dot{m}$  values and with three anode materials—lead, copper, and graphite. It is observed that the voltage hash is a random process, without a characteristic time scale, whose statistics evolve with  $J^2/\dot{m}$ , without a significant dependence on the anode material. The statistics of the hash—particularly, the first four moments of the probability density—are Gaussian at low  $J^2/\dot{m}$ , and evolve away from Gaussian until  $J^2/\dot{m} \sim 110 \text{ kA}^2\text{-s/g}$ , after which they return to Gaussian. Using an anode spot model, the reversal of the statistics trends at this value of  $J^2/\dot{m}$  is interpreted as a result of the formation of many anode spots. It is suggested that many anode spots are formed due to a filamentation instability which causes the current to fragment into many channels, irrespective of the anode material.

The damage caused by anode spots on the MPDT anode is investigated by analyzing the marks left behind on anodes subjected to operation at high  $J^2/\dot{m}$ . It is found that no characteristic size of damage marks exists, but that the sizes self-organize into a power-law distribution, such that the probability of spot damage of size  $d \sim 1/d^\delta$ , where  $\delta \geq 1$ . The severity of the damage is observed to be primarily dependent on the anode thermal properties and not  $J^2/\dot{m}$ . Lead anodes, for example, show spot damage at all  $J^2/\dot{m}$  values, while graphite anodes show no significant damage at any  $J^2/\dot{m}$ . Two insights follow: one, that the current conduction to the MPDT anode is, to some extent, spotty at all current levels, though it is for

the most part diffuse at low  $J^2/\dot{m}$ ; and two, that the  $J^2/\dot{m}$  value at which hash appears, and that at which significant damage appears, need not be the same if anode materials are properly chosen. The anode material is primarily a passive player in the discharge, responding to the action of anode spots but not significantly influencing their properties.

Optical diagnostics are used to study the effect of anode vapor on the voltage hash. It is shown that while hash of large magnitude can be accompanied by erosion, the hash is suppressed when the anode vapor is copious enough to bridge the gap between the anode and cathode. It is also shown that this effect is unsteady, which causes non-stationarity in the hash statistics. This concurs with the previous conclusions that the behavior of hash is not governed strictly by erosion, or vice versa.

Experiments with a constrained-attachment anode, which allows the arc to attach in only 0.5 mm discrete spots, show that the arc may be stabilized by forcing its attachment on small anode areas. It is found that the arc attachment stabilizes preferentially on the inner anode face, accompanied by a quiet voltage and significant anode erosion. Examination of the thruster behavior suggests that attachment stabilization precedes erosion. It is concluded that either voltage hash, or anode erosion, may be eliminated using the present constrained-attachment technique, and that eliminating both simultaneously may be accomplished with an appropriately refractory anode material.

# Acknowledgements

The many people and avenues of support that have helped me to endure and thrive while at Princeton are a disjointed group, many not familiar with the others; but all pulled together to bring me through, or put me through, the highest of highs and lowest of lows that life has yet brought my way. I would be remiss in not thanking those who have made such contributions.

How could I but thank Edgar Choueiri for making it possible to spend the last several years at Princeton? Aside from the research opportunity, and the advice and the time he put into helping me develop academically, his patience during my first years while teaching me to play, and love playing, a good game of squash quite literally changed my life. The lab he led introduced me to

Bob Jahn, Sergey Macheret, Richard Miles, Sam Cohen, Stewart Zweben, Bob Sorenson, Rob Murray, and Glenn Northey, each of whom, in his inimitable way, has enhanced my education. Lab students Slava Spektor, Jack Berkery, Lenny Cassady, Kurt Polzin, Andrea Kodys, Jimmy Cooley, and Kamesh Sankaran, all of whom were my elders, in that capacity took me by the hand and led me into the fascinating and sometimes troubling world of plasma physics. The younger generation of students—Ashley Hallock, Ben Jorns, and Danny Lev—helped to keep me sane during my last two years. Special thanks go to Danny for housing me in my last months, after beautiful Whitman was no longer my home. The aid that all of these gave me was supplemented by

Euan McLeod, Nick Kattamis, and Matt Brown—who shared their knowledge, and all too much of their time, with me as I learned to prepare surfaces and drill with lasers. I had the pleasure of working with Eric Whitman and Paul Giuliano, undergraduate researchers who, I fear, taught me more about building equipment, and being excited about doing so, than I taught them. Zhili Zhang provided me with more equipment on loan than perhaps any of my fellow students. Tim Ombrello was

a great a source of advice, encouragement, and conversation, from the first day I arrived at Princeton. I'm glad we finally got to golf Springdale and discuss life and physics while at it. Tim was one among the

2003 MAE cohort—including Mike, Pat, Tom, and Melissa—who eased my transition to Princeton and provided me outlets not possible on my own, whether TV time, flying time, or a couch hitched to a ride-on lawnmower. I should thank Mike in particular for his suggestion that we visit the art museum one Friday night, which is how I learned of

PEF, and so came to develop a family among these wonderful believers. In that context I have had the pleasure of being friends with Erik and Erin Nielsen, David and Christina Keddie, the one-time Amie Scott, and a multitude of undergraduates who gave of themselves for me, and at times allowed me to do the same for them. It was through this PEF family that I met

Carissa Gonzalez, whose contributions to my life during the final phases of my Princeton work cannot be measured by any metric I know. At one time I believed that Princeton was offering me its best with the Ph.D.; how wrong I was. Carissa is a well of love, peace, patience, and goodness who has transformed my last year at Princeton, the most phrenetic I have ever known, into the most blessed and memorable time imaginable. The only source of encouragement that rivals Carissa is

my family, who, despite having no idea what it is I do, so often believed in me far more than I did in myself, and whose irrational faith in my ability to see this work through helped, time and again, to inspire some of the same in me. How strange that all of this should start with my family on a southern California goat farm!

As I reflect on the unlikely sets of circumstances that guided my path to, and through, Princeton, the providential hand of God is plain to me, and to Him must go thanks beyond that which I could give to any other.

And now—as a wise man before me once said—on to my next life.

My time at Princeton was supported, in part, by the National Defense Science and Engineering Graduate Fellowship program through the Air Force Office of Scientific Research, the Princeton Upton Fellowship fund, the Princeton Program in Plasma Science and Technology, the NASA ALFA<sup>2</sup> project, and the Wallace Memorial Fellowship fund.

This dissertation carries the designation 3190-T in the records of the Department of Mechanical and Aerospace Engineering.



To Wendell P. Smith

# Contents

Abstract . . . . .	iii
Acknowledgements . . . . .	v
<b>1 Introduction</b>	<b>1</b>
1.1 A Broad Overview . . . . .	1
1.2 The Cost Motivation for Electric Propulsion . . . . .	1
1.3 The Magnetoplasmadynamic Thruster (MPDT) . . . . .	3
1.3.1 The Onset Phenomenon . . . . .	5
1.4 Goals of This Thesis . . . . .	12
1.5 Organization of This Thesis . . . . .	13
<b>2 Experimental Facility and Diagnostics</b>	<b>15</b>
2.1 Thruster and Facility . . . . .	15
2.1.1 The Princeton Benchmark MPDT . . . . .	15
2.1.2 Vacuum Facility . . . . .	18
2.1.3 Power Supply and Firing Control . . . . .	20
2.2 Diagnostics . . . . .	21
2.2.1 Automated Data Acquisition . . . . .	21
2.2.2 Voltage Measurement . . . . .	22
2.2.3 Spectroscopic measurements . . . . .	29
2.2.4 High-Speed Videography . . . . .	30

<b>3</b>	<b>Characterization of Voltage Hash</b>	<b>31</b>
3.1	Introduction . . . . .	31
3.2	Background . . . . .	32
3.3	The MPDT Voltage . . . . .	33
3.3.1	Overview . . . . .	33
3.4	Voltage Hash Statistics . . . . .	34
3.4.1	The Analysis of Random Fluctuations . . . . .	34
3.4.2	Hash Statistics for Varying $J^2/\dot{m}$ and Anode Materials . . . . .	38
3.5	Voltage Spectra . . . . .	43
3.6	The Origin of Voltage Hash . . . . .	45
3.6.1	Model of Random Superposition of Events . . . . .	45
3.6.2	Discussion . . . . .	52
3.7	A Further Word on Filamentation in the MPDT . . . . .	54
3.8	Summary of Results . . . . .	55
<b>4</b>	<b>Patterns of Anode Damage</b>	<b>57</b>
4.1	Introduction . . . . .	57
4.2	Background . . . . .	57
4.3	The Effect of Contamination and Boundaries . . . . .	58
4.3.1	Anode Damage Attractors . . . . .	59
4.4	Anode Spot Damage . . . . .	63
4.4.1	Anode Damage Severity . . . . .	64
4.5	Distribution of Anode Mark Sizes . . . . .	67
4.6	Time Evolution of Anode Damage . . . . .	69
4.6.1	Background . . . . .	69
4.6.2	Spot Evolution on the MPDT Anode . . . . .	73
4.7	Damage to Anodes of Extreme Materials . . . . .	78
4.7.1	Damage to a Lead Anode . . . . .	80

4.7.2	Damage to a Graphite Anode . . . . .	82
4.8	Summary of Observations on Anode Damage . . . . .	83
<b>5</b>	<b>The Relationship of Voltage Hash to Anode Erosion</b>	<b>85</b>
5.1	Introduction . . . . .	85
5.2	Optical Diagnostics . . . . .	87
5.2.1	Time-resolved spectral measurements . . . . .	87
5.2.2	High-Speed Video . . . . .	92
5.3	Summary of Results . . . . .	97
<b>6</b>	<b>Experiments with a Constrained-Attachment Anode</b>	<b>99</b>
6.1	Introduction . . . . .	99
6.2	The Constrained-Attachment Anode . . . . .	101
6.3	Operation and Voltage Behavior . . . . .	103
6.4	Erosion of the Constrained-Attachment Anode . . . . .	104
6.5	Voltage Hash with the Constrained-Attachment Anode . . . . .	107
6.6	Discussion . . . . .	108
6.7	Summary and Insights . . . . .	110
<b>7</b>	<b>Conclusion</b>	<b>112</b>
7.1	A Broad Overview . . . . .	112
7.2	Summary of Findings . . . . .	113
7.2.1	Voltage Hash . . . . .	113
7.2.2	Anode Damage . . . . .	114
7.2.3	Relationship Between Voltage Hash and Anode Damage . . . . .	115
7.2.4	Use of the Constrained-Attachment Anode . . . . .	115
7.3	Insight into Onset Phenomena . . . . .	116
7.4	Open Questions . . . . .	117

<b>A</b>	<b>Voltage Hash Influence on MPDT Current</b>	<b>120</b>
A.1	The MPDT Current . . . . .	120
A.1.1	Expectation . . . . .	120
A.1.2	Current Measurement . . . . .	122
<b>B</b>	<b>Cathode Tip Current Measurements</b>	<b>130</b>
B.1	Rogowski Coil . . . . .	131
B.2	Typical Results . . . . .	132
<b>C</b>	<b>Relationship Between Plasma Density Fluctuations and Voltage Hash</b>	<b>135</b>
C.1	Langmuir Probe Apparatus . . . . .	136
C.2	Simultaneous Density Fluctuation and Voltage Hash Observations . .	137
<b>D</b>	<b>Further Literature Review of Onset Phenomena</b>	<b>140</b>
D.1	Thruster design impact on $(J^2/\dot{m})^*$ . . . . .	140
D.2	Thruster behavior beyond $(J^2/\dot{m})^*$ . . . . .	142
D.3	Theoretical Prediction of $(J^2/\dot{m})^*$ . . . . .	146
D.4	Other Onset Theories . . . . .	150
D.4.1	Back-EMF Onset . . . . .	150
D.4.2	Unstable Current Channels . . . . .	151

# Chapter 1

## Introduction

### 1.1 A Broad Overview

It is our intention in this dissertation to develop an understanding of the unsteady behavior of the magnetoplasmadynamic thruster (MPDT) operated at high current. The MPDT is an electric propulsion system for spacecraft which promises to lower the propellant consumption, and so the cost, of interplanetary space missions. The MPDT has seen experimental, but not operational, flight for a number of reasons, primarily the lack of sufficient power on spacecraft. In high-current operation, the MPDT reaches an instability threshold at which the thruster's behavior is characterized by electrically noisy, unrepeatable operation and unacceptably high amounts of damage to thruster components. In what follows, we will take on the task of understanding better the characteristics of the MPDT's unstable behavior, as a first step toward eventually understanding how to stabilize its high-current operation.

### 1.2 The Cost Motivation for Electric Propulsion

It costs roughly \$11,000 per kilogram to launch a satellite to Low Earth Orbit, where most Earth-servicing satellites reside, on a standard Boeing Delta II-7920 launch

vehicle. To launch a spacecraft to an Earth-escaping orbit with no excess energy with the more appropriate Delta II-7925 costs about \$49,000 /kg [1]. Numbers of this magnitude necessitate mass savings wherever possible.

The spacecraft propulsion system is an attractive place to start. The average mass of the propellant used in typical communications satellites is, for example, nearly 17% of the spacecraft total mass, and can be much larger for spacecraft designed to be light [2]. A large required propellant fraction represents a significant drain on a space mission budget, for every kilogram of propellant that must be placed on the launch vehicle is a dead weight, taking the place of an otherwise useful kilogram of sensors, power, or communications equipment. The propulsion system cannot easily be miniaturized, however: the fundamental physics behind rocketry—the transfer of momentum—requires a given amount of propellant to accomplish a given mission with a given rocket. To reduce a spacecraft’s propellant mass requires a more fuel-efficient rocket.

A rocket’s mass usage is governed by the rocket equation. Newton’s second law for a spacecraft in zero-gravity free space is

$$m \frac{dv}{dt} = u_e \frac{dm}{dt} \quad (1.1)$$

where  $m$  is the spacecraft mass,  $v$  is the spacecraft velocity, and  $u_e$  is the velocity at which propellant is expelled from the spacecraft’s propulsion system. Rearranging and integrating this equation yields the well-known *rocket equation*

$$\frac{M_f}{M_i} = e^{-\frac{\Delta V}{u_e}} \quad (1.2)$$

in which  $M_f$  and  $M_i$  are the final and initial spacecraft masses after and before all the propulsion maneuvers required for the mission, and  $\Delta V$  is the index of energy expenditure required for the mission. The fraction on the left of equation 1.2 represents

the total useful mass of the spacecraft when all propellant is exhausted; this should be maximized to the greatest extent possible.  $\Delta V$  can be lowered by employing gravity assist or aerobrake maneuvers, but remains large for ambitious space missions such as those to the outer planets of the solar system. As an example, the Jupiter Icy Moons Orbiter (JIMO), a mission proposed as the first nuclear-powered spacecraft in the Prometheus project, had a  $\Delta V$  of at least 38 km/s [3].

If a standard rocket motor with a typical exhaust velocity of 3.5 km/s were used for JIMO, only 2 kg in 100,000 would be useful payload mass, the rest being propellant. The silver lining is that the useful mass fraction is an exponential function of the velocity ratio, so that small improvements in rocket exhaust velocity lead to large increases in the useful mass fraction. The well-developed and operational ion and Hall-effect thrusters have exhaust velocities ranging up to 34 km/s [2], and the JIMO useful mass fraction using such a thruster would be 32%. The dramatic rise in the useful mass fraction, and the attendant fall in the needed propellant mass and mission cost that this represents, are primary drivers for the development of high- $u_e$  electric propulsion systems.

### 1.3 The Magnetoplasmadynamic Thruster (MPDT)

The ion and Hall-effect thrusters, whose performance we just mentioned, are unsuitable for certain classes of missions. The ion thruster is a low-thrust-density engine and so is unsuitable for time-critical missions; the Hall thruster is a low-power engine which is suitable for most near-term missions but which is an unlikely candidate to process the large amounts of power available from, for example, a space-borne nuclear reactor. On the other hand, the magnetoplasmadynamic thruster (MPDT) is a simple device whose principle of operation allows it to operate at high plasma densities, and so process large amounts of power. Compared to conventional rockets, it achieves high



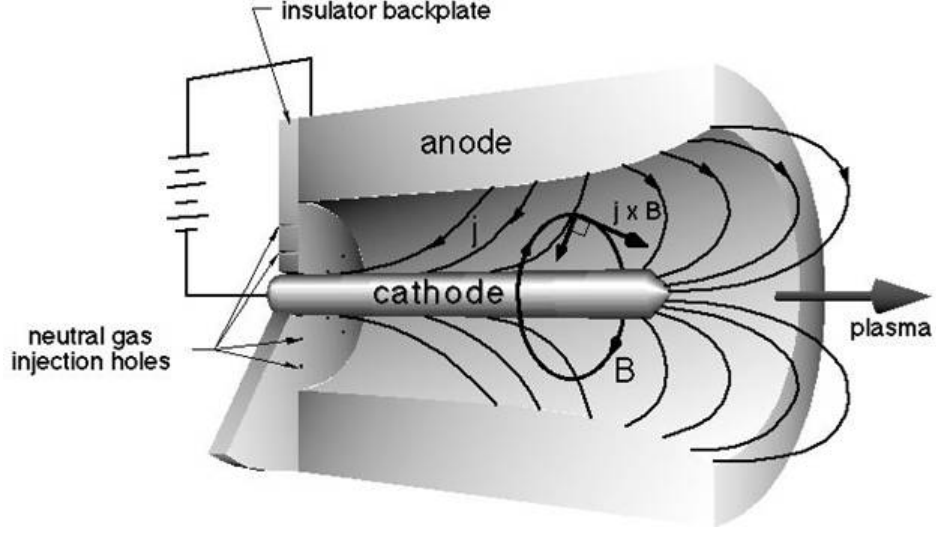


Figure 1.1: An artistic representation of the MPD thruster.

specific impulse; compared to other electric thrusters, it achieves high thrust density.

The relatively simple self-field MPDT principle of operation is shown schematically in Fig. 1.1. (The MPDT may be operated with an applied magnetic field as well, which serves to improve its performance at low powers. The self-field MPDT is ideal for high-power operation, with which we are most concerned in this work; we will therefore focus our attention on the MPDT without an applied field.) The arc cathode resides on the centerline of a coaxial geometry, surrounded by an anode which can either form the entirety of the thrust chamber, as in the figure, or only a ring that surrounds the exit plane, as in the case of the MPDT used in this work. The propellant, injected into the chamber through either the backplate as shown, or through a hollow cathode, is ionized by a voltage imposed across the electrodes and conducts a current imposed by an external power supply. The radial and axial current density profile  $\mathbf{j}$  creates an azimuthal magnetic field  $\mathbf{B}$ , and the interaction of the two results in the volumetric Lorentz force density

$$\mathbf{f}_L = \mathbf{j} \times \mathbf{B}. \quad (1.3)$$

If the Lorentz force density is integrated over the whole thrust chamber, the

magnitude of the total electromagnetic thrust produced by the MPDT is [4]

$$T_{EM} = \frac{\mu_0}{4\pi} \left( \ln \frac{r_a}{r_c} + \phi \right) J^2 \equiv bJ^2 \quad (1.4)$$

where  $\mu_0 = 4\pi \times 10^{-7}$  H/m is the permeability of free space,  $r_a$  and  $r_c$  are the radii of the anode (measured at the smallest point) and cathode, and  $\phi$  is a constant of order one that depends upon the specifics of the current attachment on the cathode tip.

The thrust of Eq. 1.4 increases with the square of the current  $J$ , and has no dependence on either the species or mass flow rate of the propellant. Following this ideal equation, the thrust can be made arbitrarily large by increasing  $J$ , while the specific impulse  $I_{sp}$  can be made arbitrarily large at any thrust level by decreasing the propellant feed  $\dot{m}$ :

$$I_{sp} = \frac{u_e}{g_o} = \frac{b}{g_o} \frac{J^2}{\dot{m}}. \quad (1.5)$$

From this point of view, the MPDT can in principle be operated with any desired combination of thrust and  $I_{sp}$  by simply specifying the parameter  $J^2/\dot{m}$ .

To achieve high thrust, high  $I_{sp}$ , and high thrust efficiency [5] with the MPDT,  $J^2/\dot{m}$  must be made large. It is in pursuing large  $J^2/\dot{m}$ , whether by raising  $J$  or lowering  $\dot{m}$ , that the “onset phenomenon”—the term for noisy, unrepeatable operation and unacceptable damage—is encountered. We will spend the remainder of this dissertation pursuing a greater understanding of the origin and properties of onset.

### 1.3.1 The Onset Phenomenon

#### Discovery and Properties

The MPDT evolved empirically from the electrothermal thrusters known as arcjets, beginning in 1964 [4, 6]. The evolution from the arcjet to the MPDT required only a decrease in the mass flow rate (by a factor of  $\sim 10^3$ ) and an increase in the

current from hundreds to thousands of Amperes. Because of these changes, the main mechanism of thrust generation becomes the previously discussed electromagnetic Lorentz force, which replaces the electrothermal thrust of the traditionally-operated arcjet. The main operational benefit of this “thermo-ionic” mode, as it was first called, was its ability to operate in “an interesting thrust and impulse range at reasonable efficiencies...and minimal electrode erosion.” [4]

In 1972, Malliaris et. al. [7] at AVCO Corporation first reported the performance limitation that would in time become known as the “onset phenomenon”, or simply onset. Following the desire to operate at ever-higher values of  $J^2/\dot{m}$ , they discovered a critical value,  $(J^2/\dot{m})^*$ , above which they observed that the thruster voltage became noisy, the magnitude of the voltage increased dramatically, and components (details unspecified) of the thruster began to erode. They found  $(J^2/\dot{m})^*$  to be roughly constant for a given thruster geometry and propellant; the dependence on propellant atomic mass was  $\sim M^{-1/2}$ , and, qualitatively speaking, the dependence on the thruster geometry was such that larger values of the anode-to-cathode radii ratio,  $r_a/r_c$ , led to smaller  $(J^2/\dot{m})^*$ .

The decades following the work of Malliaris saw a flurry of interest in the onset problem, but no experiment was able to pin down the reason for the transition to noisy, damaging behavior with increasing current. Effort was put into both calculating the value of  $J^2/\dot{m}$  at transition using theories mainly invoking plasma instabilities, and investigating the behavior of the voltage noise and component erosion. Appendix D describes much of the enormous body of literature that has so far contributed to our understanding of onset phenomena. To summarize that discussion, we can make the following three lists:

The critical value of  $J^2/\dot{m}$  is affected by thruster design in the following way:

- *Increasing the particle density of the propellant increases  $(J^2/\dot{m})^*$ .* Propellants with lower atomic weights reach onset at higher  $J^2/\dot{m}$ , because for the same  $\dot{m}$

the particle density is greater. The dependence of  $(J^2/\dot{m})^*$  on the propellant is  $\sim M^{-1/2}$ . [7].

- *Thruster geometry alterations that increase the particle density at large radii (near the anode) increase  $(J^2/\dot{m})^*$ .* These include lowering the radii ratio of anode to cathode  $r_a/r_c$  (smaller thruster volume increases particle density) [7]; lengthening the cathode (discouraging Lorentz body forces that move plasma away from the anode) [8]; and injecting propellant at a radius similar to the anode radius (forcing more propellant near the anode initially) [9].

The behavior of the thruster once  $(J^2/\dot{m})^*$  is exceeded can be summarized as follows:

- *With rising  $J^2/\dot{m}$ , voltage noise (hash) magnitude increases slowly at first, leaps to large values, then falls again.* [8] The characteristic frequency of the hash is frequently noted as hundreds of kHz [10–12].
- *With rising  $J^2/\dot{m}$ , the erosion of all thruster components increases, but the erosion of the anode rises dramatically with respect to the others.* The anode erosion rises steadily with increasing current, not displaying the rise-and-fall of the voltage hash. [13]
- *“Spots” appear on the anode above  $(J^2/\dot{m})^*$ , apparently conducting significant current and melting the anode at discrete sites.* Evidence for anode spots comes from both high-speed photography, which captures spots when they occur [10], and observations of the anode after firing, when the damage is visible [14].

Finally, attempts to explain the onset of the voltage hash describe  $(J^2/\dot{m})^*$  within the framework of either *anode starvation* or *plasma instabilities*:

- *The anode starvation model argues that the current conduction to the anode is sheath limited. Attempts to conduct current greater than the sheath-limited*

*current result in onset phenomena.* The value of the sheath-limited current is taken to be that carried by a random thermal flux of electrons across the sheath ( $n_e \bar{c}_e/4$ ) [14, 15]. Thus any increase in the anode-adjacent particle density, through propellant species or geometry changes, delays starvation.

- *The plasma instability models invoke a class of instabilities excited by large relative velocities between electrons and ions, known as drift instabilities. Large currents create large drift velocities and excite instabilities.* The criterion for instability is taken as a critical drift velocity, which the electrons attain when the driven current exceeds a threshold [16, 17].

Both the anode starvation and plasma instability models have had some success predicting, and explaining the trend in,  $(J^2/\dot{m})^*$ . In fact, the two are possibly related to one another. The anode starvation model has nothing to say about what occurs in the adjacent plasma when the anode is starved; presumably some sort of instability is excited. Meanwhile, the plasma instability model invokes a current threshold that is equivalent to a near-anode plasma density threshold. Classic examples are the papers of Baksht [15] (anode starvation) and Shubin [17] (plasma instability), which derive the same expression for  $(J^2/\dot{m})^*$ , within a numerical factor. Their two expressions are nearly identical because their criteria for  $(J^2/\dot{m})^*$  are the same—namely, that the current conducted to the anode be equal to the current from the random thermal flux of electrons given above—despite the fact that they invoke different models.

What neither of the models can predict, however, is the existence or behavior of the voltage hash, the erosion of the anode, or the spotty current attachment once  $(J^2/\dot{m})^*$  is exceeded. An “anode spot model” is sometimes invoked in its own right to explain the apparent relationship between spotty current attachment, voltage hash, and anode erosion [14, 18]. When this is done, the existence of anode spots is a postulate, without reference to how such spots of concentrated current arise out of an otherwise diffuse plasma. Instead, in this model, the voltage hash is a product of the

Table 1.1: Onset currents in the Stuttgart experiment

Anode gas fraction (%)	Onset Current (A)
0	4020
2	4090
5	4180
10	4230

formation, extinction, and movement of anode spots; the power that spots deposit in the anode is sufficient to sublime or melt anode material, leading to the observed damage; and the evaporated anode material serves to solve the starvation crisis that triggered the spots in the first place. The work of Diamant et. al. [19] supports this thesis, though in a phenomenological rather than an analytical manner.

### Onset Suppression

Because there is not a complete understanding of what drives the thruster behavior above  $(J^2/\dot{m})^*$ , attempts to circumvent the deleterious effects of onset have met with only qualified success. Indeed, many of the factors that influence  $(J^2/\dot{m})^*$  discussed in the last section were discovered while pursuing a method of onset suppression, especially as regards the thruster geometry.

The only reported onset suppression schemes involve artificially solving the anode starvation crisis. One such scheme, reported in 1987 at the Universität Stuttgart, diverted a portion of the propellant flow to orifices on the thruster anode, relieving the starvation crisis by a judicious choice of injection site [12]. The voltage-current characteristics for their experiment are shown in Fig. 1.2. The increasing slope in the characteristic, which the authors use to determine when onset is reached, is delayed by a small amount when propellant is diverted to the anode. Table 1.1 shows the onset currents determined for several anode gas injection fractions.

The lesson from the Stuttgart experiment is clear:  $(J^2/\dot{m})^*$  can be raised by injecting a portion of the propellant at the anode in an effort to artificially avert

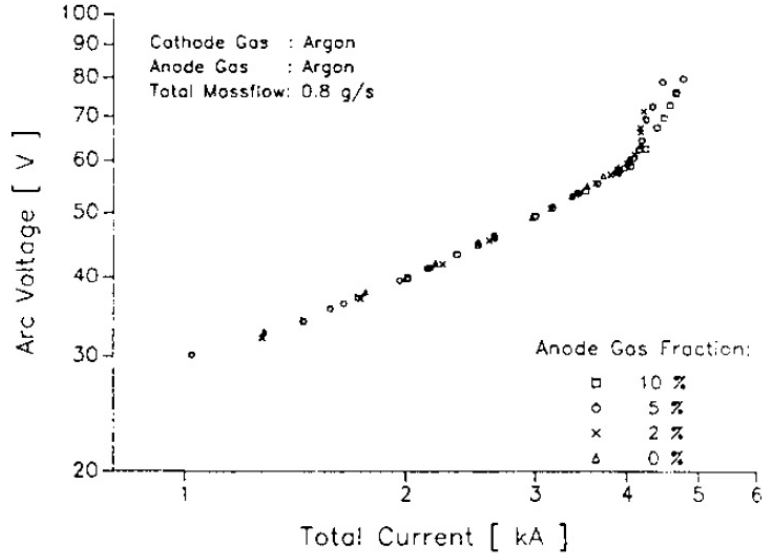


Figure 1.2: The voltage-current characteristics of the Stuttgart anode gas injection experiments.

anode starvation. What is also clear is the effectiveness of this approach: with 10% of the propellant injected at the anode, the onset current rose by only 5%. Continuing this trend would yield small increases in onset current, and large waste of propellant that is, because of its injection location, exempt from effective acceleration by the body forces that operate predominantly near the cathode.

Another onset suppression mechanism, called the “stinger” effect, was reported at Princeton in 1978 [20]. In this case, Rudolph et. al. noted that diagnostic probes inserted into the thruster somewhat suppressed voltage hash. Affixing a plexiglas rod (“stinger”) in the thrust chamber, as in Fig. 1.3, produced the same result. A stinger of any length (three were tried) produced identical results, a suppression of the voltage hash magnitude as seen in the same figure.

The light emission spectra of the thruster plume indicate, in this experiment, that the stinger ablates significantly. The authors therefore conclude that the stinger adds additional mass to the discharge—tantamount to increasing  $\dot{m}$ .

We are not aware of any successful attempt at onset suppression that cannot in some manner be understood as a way to increase the near-anode plasma density.

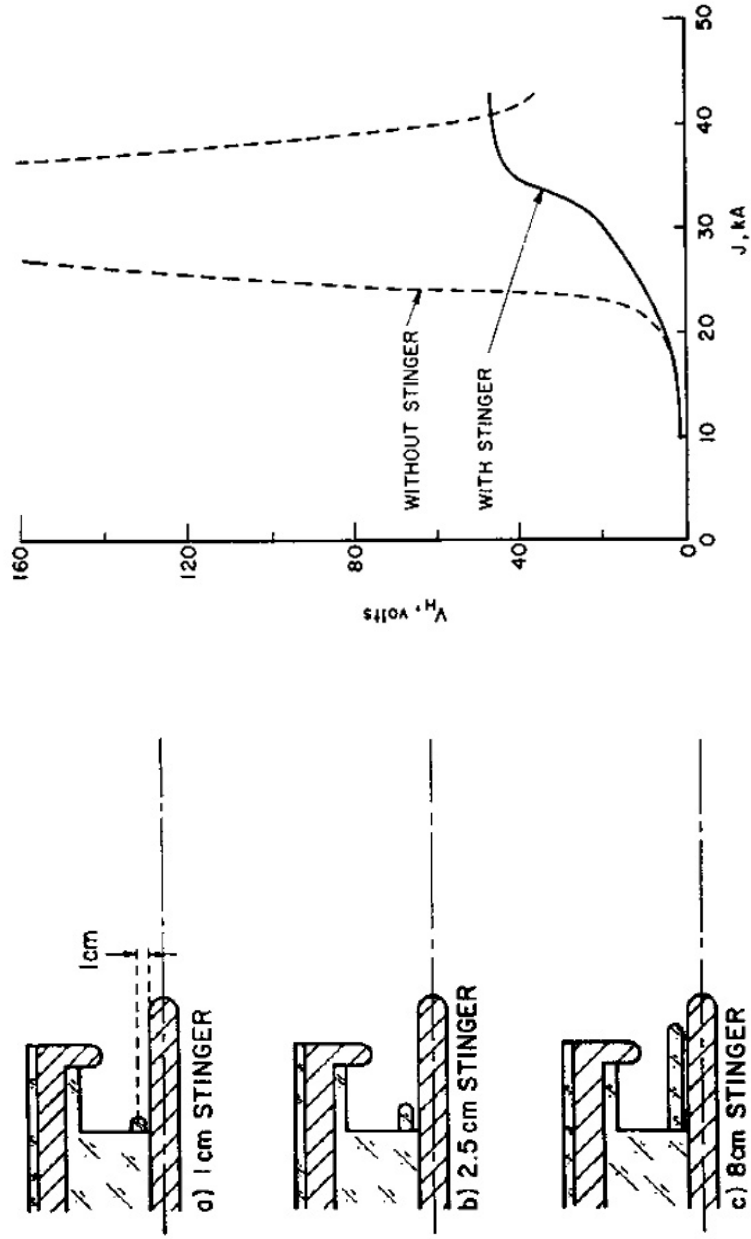


Figure 1.3: The “stinger” used in the Princeton suppression scheme (left); suppression of voltage hash using the stinger (right).



All of the geometry alterations mentioned in the previous section are of this type; diverting mass to the anode region by selective injection also is, most obviously; adding additional discharge mass, whether through an ablation process or simply increasing the propellant flow rate accomplishes the same goal. Adding mass to the discharge, however, raises the onset current but does not necessarily raise  $(J^2/\dot{m})^*$ ; geometry alterations also eventually reach a limit of efficacy. The Princeton Full-Scale Benchmark Thruster (FSBT), which we use as the testbed in this work, incorporates many of the beneficial geometry changes.

## 1.4 Goals of This Thesis

The ultimate goal of onset studies in general is to raise  $(J^2/\dot{m})^*$ . It seems clear, however, that the fundamental understanding of the processes at work in the thruster operating above  $(J^2/\dot{m})^*$  is not at present sufficient to inspire creative ways to accomplish this goal. What we have undertaken to accomplish in this work, therefore, is to gain a better grasp of the phenomenology of onset, especially of the voltage hash and the anode damage so often observed above  $(J^2/\dot{m})^*$ .

To that end, we have asked the following questions:

- *What are the characteristics of voltage hash at thruster operation above  $(J^2/\dot{m})^*$ ?*  
Specifically, what—if any—timescales are important in the voltage fluctuation, and how do these—and the hash magnitude—depend upon the anode material? What insights can we draw about the physical processes that give rise to the hash based on these observations?
- *What are the characteristics of the damage suffered by the anode at thruster operation above  $(J^2/\dot{m})^*$ ?* Specifically, what are the characteristic sizes of the observed damage? How does the extent of the damage depend upon the anode

material? And again, what insights can we draw from these observations about the physical processes that give rise to the damage?

- *How are the voltage hash and the anode damage related to one another?* Based upon the phenomenology uncovered in answering the previous two questions, what can we say, in particular, about the influence of the anode damage upon voltage hash?
- *Can we use our insights into the onset phenomena to devise a method of exerting control over thruster behavior beyond  $(J^2/\dot{m})^*$ ?*

Our approach will be empirical and phenomenological. We will use the Princeton Full-Scale Benchmark Thruster (FSBT), making a number of careful modifications and observing and analyzing the response of the onset behavior. From these observations, we will draw specific conclusions regarding each of the above questions.

## 1.5 Organization of This Thesis

We will begin in Chapter 2 by describing the experimental facility, methods, and diagnostics used in our investigation. We will focus especially on the interpretation of thruster voltage measurements, which can easily be corrupted by noise from the power supply. We then move on, in Chapter 3, to a description of voltage hash, its properties, and the effect of anode material variation on those properties—answering the first question above. We perform the same investigation, in Chapter 4, of the anode damage, in order to answer our second question. In Chapter 5, we answer the third question with a discussion of the previous chapters’ results, and several optical diagnostics. Finally, in Chapter 6, we describe an experiment designed, with the insight of the previous chapters, to assess the effect of stable anode attachment on voltage hash. In each chapter, we distill our observations into collections of salient

physical insights. We wrap up the discussion in Chapter 7 with a summary of the important results of our work and a discussion of questions we left open in the process.

# Chapter 2

## Experimental Facility and Diagnostics

### 2.1 Thruster and Facility

#### 2.1.1 The Princeton Benchmark MPDT

The Princeton Full-Scale Benchmark MPDT (FSBT) forms the basis of the experimental work reported in this thesis. The FSBT is a geometry that has been empirically optimized using data gathered over many years of use [8, 9, 13] and for which a large database of performance data has been assembled [5, 21]. It is also the thruster geometry used in Diamant’s work on anode spotting [14, 19]. We use this thruster design because its performance characteristics are well-known, and the effects of modifications are therefore more clear than they would be in any new thruster design. Information on the original incarnations of the FSBT, beyond what is provided in this section, can be found in the references just cited.

The thruster consists of a tungsten cathode 1.8 cm in diameter and 10 cm long, and a ring anode 10 cm i.d., 19 cm o.d., and 1 cm thick. The outer face of the anode is entirely exposed to the discharge, while only 1 cm of the inner face is exposed; a

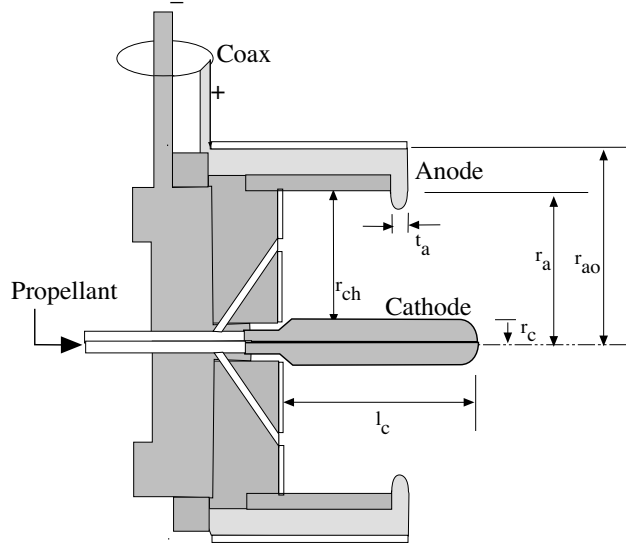


Figure 2.1: The Princeton Benchmark MPDT.  $r_c = 0.95$  cm,  $r_a = 5.1$  cm,  $r_{ao} = 9.3$  cm,  $r_{ch} = 6.4$  cm,  $t_a = 0.95$  cm, and  $l_c = 10$  cm.

semicircular lip connects the two faces. The inner wall of the thrust chamber is a quartz cylinder of 12.6 cm diameter, and the back wall, into which the cathode is fixed, is a boron nitride disc. A schematic of the FSBT is shown in Fig. (2.1).

The thrust chamber receives propellant through an annulus at the base of the cathode and twelve holes forming a circle of 3.8 cm diameter in the boron nitride back wall. The propellant enters these supply lines in roughly equal (54%/46%) proportions through a sonic orifice; the pressure behind the orifice regulates the flow rate. A plenum sits behind the back wall to supply the propellant, separated from the vacuum by a solenoid valve. This valve we open quickly using the fast discharge of a capacitor triggered by a transistor. In this work, only results using argon propellant are reported.

## The Anode

Among the various thruster components, we focus our attention nearly exclusively on the anode. In past studies, the anode ring was machined of readily available copper,

aluminum, or steel alloys. We have found it instructive to employ both the standard aluminum and copper anodes, but these materials have thermal properties that are not very different from one another. To check the dependence of onset phenomena on anode materials, we have supplemented our anode collection with anodes of lead and graphite, two materials with extreme thermal properties. The anodes were machined in identical fashion, so that the observed differences of thruster behavior when using any of the four materials can be attributed to the material differences. We will discuss the anode material influence more extensively in Chapter 4, but for now we should note that, as regards the interaction of the anode with the discharge, the most relevant measure of the difference between materials is the erosion rate. The erosion rate into vacuum of any material is a function of the temperature—derivable from kinetic theory—and is given in SI units by the Hertz-Knudsen formula [22]

$$\Gamma = p_{sat} \sqrt{\frac{M}{2\pi kT}}, \quad (2.1)$$

where  $p_{sat}$  is the equilibrium vapor pressure. Empirical curves are available for  $p_{sat}$  for all of the above four materials [23, 24]; using these (with the three metals in the liquid phase, and graphite solid), we calculate the erosion rate  $\Gamma$  for each as plotted in Fig. 4.13.

It is clear that copper and aluminum have very similar erosion rates over the range of temperatures that the anode experiences in the FSBT, in comparison to the difference between lead and graphite. An FSBT operating with a lead anode will have significantly more interaction between the arc and the anode than one operating with a graphite anode.

We have also, as noted in the relevant locations throughout this thesis, observed the thruster behavior using anodes that are carefully polished and cleaned, and intentionally roughened and contaminated. The nomenclature used in later chapters

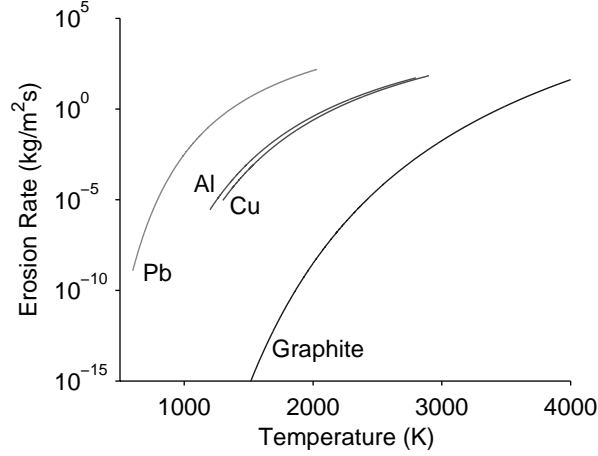


Figure 2.2: The erosion rate of four anode materials as a function of temperature.

when referring to certain sections of the anode surface is shown in Fig. 2.3.

### 2.1.2 Vacuum Facility

The thruster is mounted at one end of a fiberglass vacuum chamber of approximately 2 m diameter and 5 m length. The chamber is evacuated by two diffusion pumps backed by one roots blower and one mechanical pump; this setup maintains a back pressure on the order of  $10^{-4}$  Torr. The fiberglass construction of the tank allows the thruster and diagnostics to float electrically off of ground potential. Conductive items in the tank, such as the aluminum table on which the thruster is mounted, are covered in Mylar to prevent them from participating in the current path of the MPDT arc. Feedthroughs in one window of the vacuum tank provide power to the thruster and connections for shielded cables carrying power to, and diagnostic signals from, instrumentation located within the tank. A to-scale sketch of the facility is shown in Fig. 2.4.

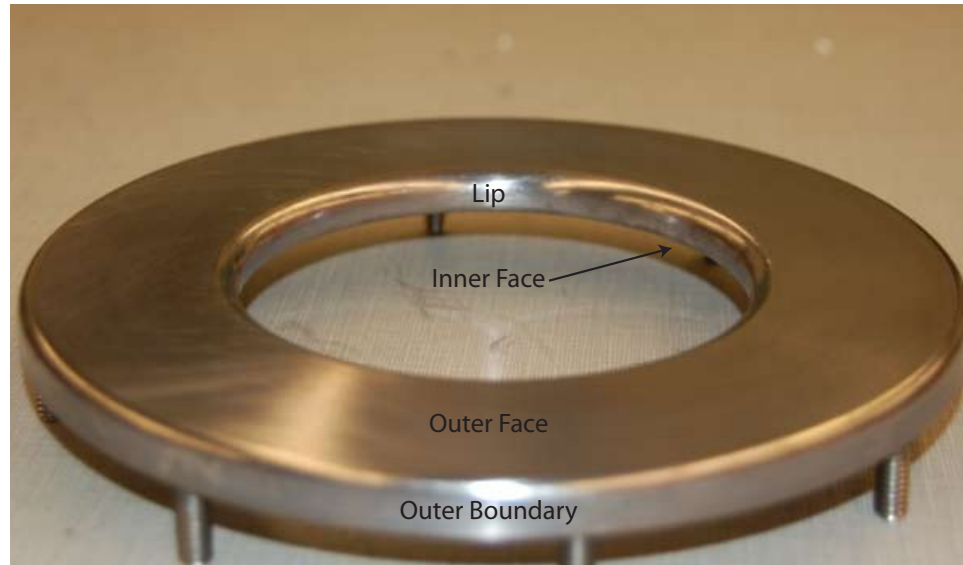


Figure 2.3: Definitions for anode locations referred to in later chapters.

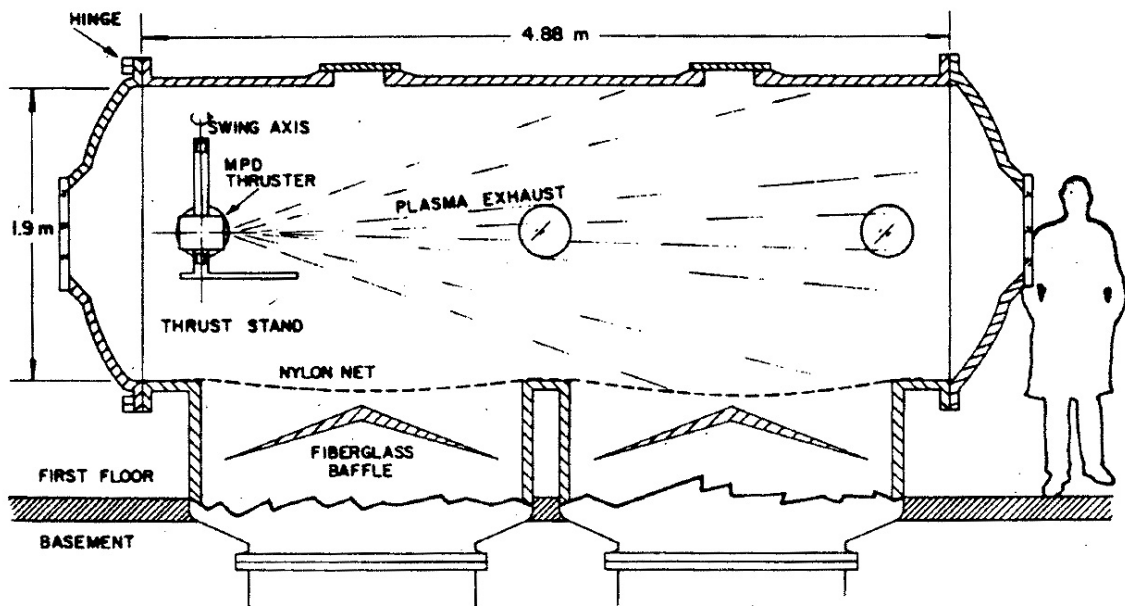


Figure 2.4: A sketch of the vacuum facility, with size comparison to the typical operator. After Burton [21].



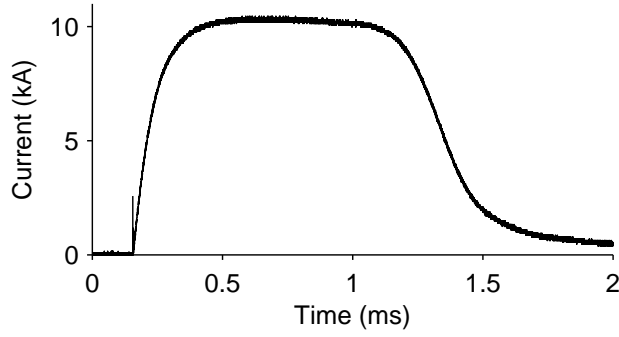


Figure 2.5: An example of the quasi-steady current output from the PFN used in this study.

### 2.1.3 Power Supply and Firing Control

The FSBT is powered by 1 ms pulses of current supplied by a 120 kJ pulse-forming *LC* ladder network (PFN). The 6.44 mF PFN is described in detail by Burton [21]. The PFN can provide approximately rectangular current pulses with a flat top of 1 ms duration, at current levels of 8 to 30 kA; an example is shown in Fig. 2.5. Because startup transients last less than 200  $\mu$ s, the current pulse provides an approximation to steady-state operation known as “quasisteady” operation [25]. Power from the PFN is switched to the thruster through a parallel-plate vacuum switch, evacuated by a mechanical pump and triggered to break down by the sudden introduction of air through a fast-acting solenoid valve.

The firing sequence for the FSBT is automated by a custom Visual Basic PC graphical interface communicating with the thruster hardware through two PC parallel ports. One parallel port controls switching of each firing subsystem with transistor-transistor logic (TTL) signals; the other is fed through a digital-to-analog converter and the signal is sent to the PFN charging electronics to govern the initial charge on the capacitors. A typical firing sequence first charges the pulse-forming network to a desired voltage (between 500 and 2000 V), within about one second. After a short delay, a trigger is then sent to the thruster propellant solenoid valve, releasing propellant into the thruster. The flow of propellant is given 25 ms to stabilize

before a trigger is sent to the vacuum switch solenoid valve, which allows air to enter the switch. Upon breakdown of the air, the circuit is closed, the propellant in the thruster breaks down, and approximately 16 amps of current flow to the FSBT for every volt across the PFN.

The automated firing process will perform a specified number of firings, at specified currents, with no operator interaction after setup. Combined with automated data acquisition, this greatly simplifies the process of acquiring large amounts of data.

## **2.2 Diagnostics**

The work in this dissertation is supported by measurements of the terminal characteristics of the FSBT (current and voltage) and plasma luminosity (using spectroscopy, photography, and video). All data, excepting photographs and videos, were recorded on Tektronix TDS5000 series oscilloscopes via an automated data acquisition system realized in Matlab.

### **2.2.1 Automated Data Acquisition**

To expedite our acquisition of large data sets, we created a data acquisition environment to identify when the thruster is fired, and to acquire, preprocess, and save the data in a usable format. The same PC used to automate the firing sequence communicates with the Tektronix oscilloscope using the open-standard VISA protocol, through a Matlab script that downloads waveforms over the Princeton network each time the oscilloscope triggers. The binary files acquired are stripped of all but the waveform and timebase information, which are then stored in memory as Matlab variables, and transferred to network storage for backup and postprocessing.

## 2.2.2 Voltage Measurement

As discussed in Chapter 1, the voltage hash is a fundamental feature of MPDT operation above  $(J^2/\dot{m})^*$ . As we wish to make a careful study of the hash properties, it is essential that the MPDT voltage signal—which, as will be shown later, contains frequency components up into the MHz—be accurately measured. Only in this way can the voltage measurement be confidently called indicative of physics occurring within the thruster. This section details the steps taken to ensure that the voltage hash measured for this dissertation is free from corruption arising from sources outside the thruster [26].

### Analysis of cabling resonances

The MPDT voltage measurement is susceptible to corruption arising from resonances in the power transmission lines connecting the PFN to the thruster. In this section we derive the response of a transmission line to a general voltage excitation in a form useful for our particular discussion; we will then use this model to understand how these resonances arise, and by what means they can best be eliminated. We model a lossless transmission line as shown in Fig. 2.6, a ladder network of  $\ell$  inductors and capacitors that approximate distributed parameters as their numbers increase and their values decrease, keeping the total inductance and capacitance ( $\ell L$  and  $\ell C$ ) constant. For this model to provide an accurate approximation to a real transmission line, the length of line lumped into a single  $L$ - $C$  station must be short compared to a quarter-wavelength of the highest frequency in the general driving signal  $V(t)$  [27]. The restriction this places on the number of  $L$ - $C$  stations is  $\ell \gg 4x/\lambda_{min}$ , where  $x$  and  $\lambda_{min}$  are the length of the line and the smallest wavelength in  $V(t)$ , respectively. Values of  $L$  and  $C$  are then chosen so that  $\ell L$  and  $\ell C$  equal the inductance and capacitance of the line being considered.

We derive the response of the transmission line using the relationship between

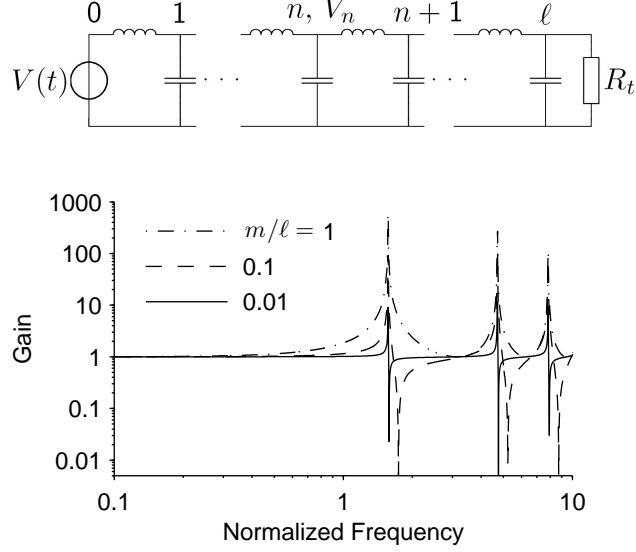


Figure 2.6: (Top) The lumped-element circuit used to approximate the response of a transmission line to a general excitation  $V(t)$ . (Bottom) Plots of the transfer function gain  $|\tilde{V}_n/\tilde{V}_0|$  from Eq. (2.11) versus the normalized excitation frequency  $\omega\sqrt{\ell^2 LC}$  for various values of  $m/\ell$ , where  $0 \leq m \leq \ell$  is the node at which the measurement is taken. The significance of the transmission line effects decreases as  $m/\ell \rightarrow 0$ .

the voltage at any two adjacent nodes and the current flowing through any two adjacent inductors:

$$\begin{aligned} V_n - V_{n+1} &= L \frac{dI_{n+1}}{dt} \\ I_n - I_{n+1} &= C \frac{dV_n}{dt}. \end{aligned} \tag{2.2}$$

These first-order equations are purely algebraic in Laplace space; therefore, we take the Laplace transform of each and combine the two to obtain a single equation relating the voltage at node  $n$  to that at the two adjacent nodes. The resulting equation is a first-order difference equation in  $n$ ,

$$\tilde{V}_{n+1} - (2 + s^2 LC)\tilde{V}_n + \tilde{V}_{n-1} = 0, \tag{2.3}$$

whose characteristic equation in the difference operator  $E$  is

$$[E^2 - (2 + s^2 LC)E + 1] V_n = 0. \quad (2.4)$$

The roots of the characteristic equation are

$$E_{1,2} = 1 + \frac{s^2 LC}{2} \mp s\sqrt{LC} \sqrt{1 + \frac{s^2 LC}{4}}, \quad (2.5)$$

so that the solution to Eq. (2.3), giving the voltage at any node  $n$ , is

$$\tilde{V}_n = AE_1^n + BE_2^n, \quad (2.6)$$

with  $A$  and  $B$  constants in  $n$  (though not in  $s$ ). The values of these constants are found by application of the boundary conditions. The first of these is at node  $n = 0$ , at which the voltage is equal to the applied value, so that

$$\tilde{V}_0 = A + B. \quad (2.7)$$

The second boundary condition states that the voltage at node  $n = \ell$  must be equal to the voltage across the terminating resistance  $R_t$ :

$$\tilde{V}_\ell = R_t(\tilde{I}_\ell - sC\tilde{V}_\ell). \quad (2.8)$$

With the simplifying definition  $\kappa \equiv 1 + sL/R_t + s^2 LC$ , this boundary condition gives the ratio

$$\frac{A}{B} = -\frac{\kappa E_2 - 1}{\kappa E_1 - 1} \left( \frac{E_2}{E_1} \right)^{\ell-1} \equiv \phi \quad (2.9)$$

so that

$$\begin{aligned} A &= \frac{\phi}{1+\phi} \tilde{V}_0 \text{ and} \\ B &= \frac{1}{1+\phi} \tilde{V}_0. \end{aligned} \tag{2.10}$$

Finally, the relationship between the input voltage,  $\tilde{V}_0$ , and the voltage at any node  $n$ ,  $\tilde{V}_n$ , is

$$\frac{\tilde{V}_n}{\tilde{V}_0} = \frac{1}{1+\phi} (\phi E_1^n + E_2^n). \tag{2.11}$$

The solution in Eq. (2.11) accurately reproduces such phenomena as cable resonances due to standing waves, termination phenomena, and phase shift. Because it allows a simple calculation of the voltage at any node  $n$ , it readily facilitates our discussion of the transmission line's effect on voltage measurements.

### **Application to thruster voltage measurements**

Any pulsed electric thruster is connected to its power supply through some length of transmission line that can be modeled as in the previous section. The thruster itself corresponds to the voltage source  $V(t)$  in the model of the last section, and the thruster voltage measurement must be located at some point  $m$  along the transmission line. Physical constraints often dictate that this point be some distance from the thruster. The measurement is therefore not, practically speaking, taken at node 0, where it ideally ought to be, but at some node  $0 \leq m \leq \ell$ . The terminating resistance,  $R_t$ , is a large value—the transmission line is essentially open-circuited when connected to the passive supply. We will now discuss the important consequences of this arrangement.

The plot in Fig. 2.6 shows the transfer function of Eq. (2.11) relating a voltage measurement taken at various values of  $m/\ell$  to the input voltage  $V_0$ . The frequency  $\omega$  ( $= is$ ) is shown normalized to the  $L$ - $C$  resonance frequency of the total line parameters

$\ell L$  and  $\ell C$ . This plot shows that transmission line resonances appearing in the transfer function significantly emphasize certain frequency components of the input signal, even for voltage measurements made relatively close to the source (e.g.,  $m/\ell = 0.01$ ). The bandwidth of affected frequencies and the magnitude of the resonances are both decreased as  $m/\ell \rightarrow 0$ , and the transfer function approaches the ideal of a flat line with unity gain. The most important insight to be gained from Eq. (2.11) and Fig. 2.6 is the extent to which a measurement of  $V(t)$  can be altered by a measurement location at even a small distance away from the source along the transmission line.

### Experimental verification

The pulsed MPDT is particularly susceptible to the problem discussed in the last section. It typically is powered by a high-energy PFN that, because of practical constraints, is located some distance from the thruster: relatively long pulse times, on the order of 1 ms, do not require particularly low-inductance configurations. The cabling is therefore usually long, and the voltage measurement easier to take at a point distant from the thruster. In this section, we demonstrate the principles of the last section using the FSBT [5, 21]. The FSBT voltage contains large transients during operation at high currents, at and above the onset current [5]. The power transmission line for this particular thruster is  $\sim 11$  m of 40 parallel RG-8 coaxial cables and other parts (e.g., gas switch, thrust stand, ballast resistor) whose combined inductance and capacitance place the fundamental resonance frequency at 1.3 MHz.

For this demonstration, we simultaneously measured the voltage at two locations with identical voltage probes, the first (the “inner” measurement) at 7.5 cm behind the upstream end of the discharge chamber—the closest feasible location to the FSBT discharge—and the second 1 m from the thruster body, at the power feedthrough on the vacuum tank (the “outer” measurement), where such measurements are commonly taken. The  $m/\ell$  values for these two locations are  $10^{-4}$  and 0.05, respectively. These

values were calculated by taking the ratio of the inductance between the discharge and the measurement location—which in the first case included only the thruster body, and in the second the thruster body, thrust stand, and vacuum feedthrough—to the inductance of the entire power transmission line. This method of calculating  $m/\ell$  is necessary because the distributed capacitance and inductance of the various components are not equal to one another, as assumed in the model of the last section; however, since the physical extent of these components is much smaller than wavelengths of interest in the voltage signal, their inductance and capacitance contributions can be lumped into  $L$ - $C$  stations in the model of Sec. 2.2.2 in the same way as lengths of constant-parameter transmission line.

We show, in Fig. 2.7, a comparison between the inner and outer voltage measurements, for the case of the FSBT firing at  $J^2/\dot{m} = 108 \text{ kA}^2\text{-s/g}$ . This is a condition well above onset ( $J^2/\dot{m} \sim 60 \text{ kA}^2\text{-s/g}$ ), and significant voltage transients appear on both traces. However, the most prominent feature on the outer measurement is a large-amplitude sinusoidal *oscillation* around a mean of 350 V with a frequency of 1.3 MHz, whereas what appears most prominently on the inner measurement is a series of voltage peaks rising several hundred volts from a 350 V baseline, each lasting several  $\mu\text{s}$ . These peaks, and not the oscillations, represent the true nature of the fluctuating voltage.

Power spectra of the two measurements, each showing the effect of the resonance, are also shown in Fig. 2.7. The peak of the resonance on the inner measurement is six times smaller, and much narrower, than that of the outer measurement. Each of these empirical observations was predicted by the trends seen in Fig. 2.6. Because the resonance on the outer measurement is so large and broad, attempts to filter out the 1.3 MHz oscillation would affect frequencies well down into the hundreds of kHz, leaving the filtered waveform bearing only a loose resemblance to the true waveform.

The voltage measurements presented in this work are all performed near the



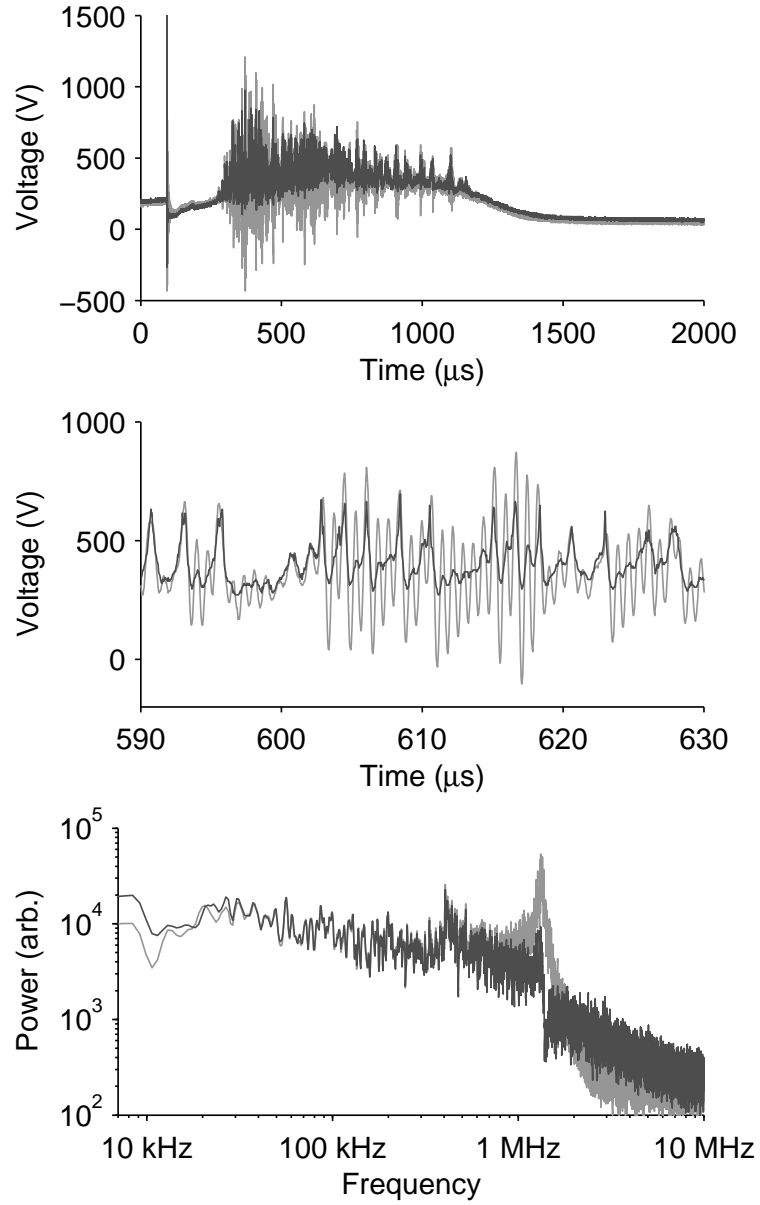


Figure 2.7: Plots of the FSBT voltage for a firing at  $J^2/\dot{m} = 108 \text{ kA}^2\text{-s/g}$ . In both the full (upper) and expanded (middle) views, the grey trace is the “outside” ( $m/\ell = 0.05$ ) measurement and the black trace the “inside” ( $m/\ell = 10^{-4}$ ) measurement. The effect of the resonance at 1.3 MHz is to distort the signal sufficiently that the true structure is unidentifiable. The theoretically expected resonance is manifest in the power spectra of these two signals (bottom).

thruster electrodes, to eliminate the source of measurement corruption that this section has illustrated.

### 2.2.3 Spectroscopic measurements

We measured the luminosity of the FSBT plume using an RCA 1P28 photomultiplier tube (PMT) placed at the output slit of a 1 m Spex 710 spectrometer. The Spex is equipped with a diffraction grating optimized for visible wavelengths. We chose a configuration of collecting optics and input/output slit width combination to collect light at a position directly downstream of the thruster, from a section of the thruster face roughly 2 cm wide, centered on the thruster's axis of symmetry. The positioning of the optics was previously used to obtain time-integrated spectra of the thruster discharge, in which anode erosion was detected [8]. With this configuration, the wavelength resolution was about  $\pm 5 \text{ \AA}$ .

We made optical measurements of the thruster luminosity at two wavelengths: 4727  $\text{\AA}$ , a line in the spectrum of ArII, and 5039  $\text{\AA}$ , in the spectrum of CuII. [28] These lines are sufficiently far removed from other lines in the combined spectrum of Ar, Cu, and W that they can be singled out with the given resolution of the spectrometer. In this way, we are able to distinguish the independent behavior of argon and copper in the discharge. Measurements with this spectrometer setup were only made using a copper anode on the FSBT.

The PMT signal is buffered at its output through a 100 k $\Omega$  resistor and an Analog Devices AD818 video amplifier. The frequency response of this system is flat to above 1 MHz. We digitally filter the signal in post-processing to remove power supply noise to which the PMT is sensitive.

### 2.2.4 High-Speed Videography

High-speed videos of the thruster during operation were taken with a Photron Ultima APX high-speed video camera. In order to capture the behavior of the arc with sufficient time resolution, the camera's adjustable frame rate was set at 20,000 frames per second or greater, allowing for 20 or more frames to be taken during a 1 ms firing. The relatively low resolution of the camera at high speeds—256 by 64 pixels at 50,000 fps, for example—make the video appear pixelated, but spatial resolution was sufficient to identify important components of the discharge. In many cases, the discharge appears exceedingly dim at higher frame rates, due to the low exposure time; in these cases, the videos were observed in negative, with enhanced contrast. The light entering the camera was bandpass filtered to observe only light emitted by species of interest (such as anode-material ions) in the arc. The camera was triggered by an auxiliary output of the recording oscilloscope, so that the videos were synchronized with the other data acquired.

# Chapter 3

## Characterization of Voltage Hash

### 3.1 Introduction

In Chapter 1, we described the main goal of onset research in general as devising a way to manipulate the onset behavior beyond  $(J^2/\dot{m})^*$ . In that chapter, we pointed out that, in working toward devising a creative way of doing so, we need to begin with a better understanding of the phenomenology of onset than we have at present, including specifically of the details of voltage hash and anode erosion. We begin our study with voltage hash, which we address in this chapter. We start with a short review of what is already known, and then build on this base with observations—of the hash statistics and power spectra—of our own. We will look at how the voltage hash behaves when the anode is made of lead and graphite—materials with extreme thermal properties. The difference between the two will suggest how the anode influences the processes that lead to the hash. Finally, we will discuss an anode spot model that describes how voltage hash can be generated with the properties we observe, and use this model to interpret the experimental observations.

## 3.2 Background

Prior study of voltage hash has been limited by the available technology. The greatest research interest in onset phenomena occurred in years before the availability of digital signal acquisition and the large amounts of computing power needed to process the data. Most studies stop at noting that oscillations in the thruster terminal voltage exist, for example [7, 29, 30], before moving on to discuss other onset features, such as  $(J^2/\dot{m})^*$  or simultaneous fluctuations in other plasma properties. Other studies go further, by noting that some characteristic frequency appears to exist in the fluctuations, such as in [10, 12, 13]; this frequency is universally noted to be on the order of hundreds of kHz, though this is estimated by visual observation rather than by more rigorous methods. More detailed investigations, the results of which were summarized in Chapter 1, show that the hash magnitude grows as  $(J^2/\dot{m})^*$  is exceeded, up to a certain current; after this current, the magnitude of the hash drops again to a constant level (though the erosion of thruster components continues to increase as the current is raised) [8, 9]. Finally, one study by Kuriki and Iida [11] calculated the power spectra of the voltage hash, and noted weak peaks in the spectra in a number of frequency ranges, including the hundreds of kHz and MHz ranges.

Other devices in which voltage hash appears above a current threshold (such as low-pressure arcs and vacuum arcs, both of which share much in common with the MPDT aside from the coaxial geometry) have been studied in slightly more detail. In these devices, it is generally noted that the fluctuation appears (by visual estimation) to have a characteristic frequency on the order of hundreds of kHz; however, what power spectra are available indicate that there is actually no preferred frequency in the fluctuation, but rather that it is a Brownian motion (characterized by a power spectrum that falls off like  $1/f^\beta$ , where  $1 \leq \beta \leq 2$ ) [31–36].

It is against this backdrop that we conduct the study of voltage hash that takes up the remainder of this chapter. We aim to identify relevant properties of the

hash that have been given little notice in the literature, and to use our knowledge of these properties to infer something about the process that generates the voltage hash. In doing so, we will first inspect the experimental voltage hash, and then introduce a model that is able to satisfactorily reproduce the properties of the hash. By comparing the two, we will draw conclusions about the plasma current conduction behavior that produces of the hash.

### 3.3 The MPDT Voltage

#### 3.3.1 Overview

When the firing sequence described in Chapter 2 is carried out, switching a 1 ms flat-topped pulse of current through the MPDT, the thruster responds as a nonideal circuit element driven by a stiff source. The stiffness of the source—the PFN—is due to its large inductance. Any changes in the load (the thruster) result in only small changes in current from the source, and the changes are smaller still as the load changes become higher in frequency. We therefore refer to the current as constant throughout the pulse, ignoring small changes caused by fluctuations in the thruster impedance. (For further discussion, see Appendix A.)

The voltage across the thruster self-adjusts to the current imposed by the PFN. At low values of  $J^2/\dot{m}$ , the thruster behaves as an ideal resistor, with the voltage settling to a constant value over the duration of a firing. This is the case in Fig. 3.1(a), where the voltage signal is shown without the corresponding current signal (which we introduced in Fig. 2.5). Until values of  $J^2/\dot{m} \sim 60 \text{ kA}^2\text{-s/g}$ , this behavior holds approximately true. The thruster presents an impedance of  $\sim 10 \text{ m}\Omega$  in this case.

After  $J^2/\dot{m} \sim 60 \text{ kA}^2\text{-s/g}$ , the thruster voltage begins to exhibit behavior typical of onset as described in the literature. The thruster impedance is no longer a

constant with time, but changes in such a way that the voltage fluctuates in a random fashion. This is shown in Fig. 3.1(b). The magnitude of this fluctuation grows rapidly at a higher value of  $J^2/\dot{m} \sim 80\text{--}100 \text{ kA}^2\text{-s/g}$ , so that the fluctuation resembles that shown in Fig. 3.1(c). An expanded view of the voltages from Fig. 3.1 is shown in Fig. 3.2.

Our analysis of the fluctuating voltage proceeds as follows. Each voltage trace obtained is a 2 ms sample centered on the flat-topped portion of the current trace. We take only the portion of the trace between 0.4 and 1.2 ms—which corresponds to the duration of the quasi-steady current. Because the measured voltage is a randomly fluctuating variable, we apply statistical methods to analyze the extracted sample—the mean, standard deviation, and measures, such as the skewness, of the variable’s departure from normality. We also use this sample to calculate the power spectrum of the hash, using a periodogram method and a Parzen window to obtain our estimate. To reduce spectral noise, we average these spectra over all available sample records taken with similar experimental conditions. Error bars on all quantities are representative of the scatter in the data.

## 3.4 Voltage Hash Statistics

### 3.4.1 The Analysis of Random Fluctuations

In referring to the voltage hash as “random fluctuations”, we have not done so for lack of a proper descriptor, but because this is a technically accurate description of the character of the hash. To motivate our analysis, in this section we will describe the characteristics of random fluctuations, following the classic treatment of Bendat and Piersol [37]. Then, having done so, we will apply this treatment to the voltage hash.

In the field of data analysis, a time trace (or time series)—such as our voltage

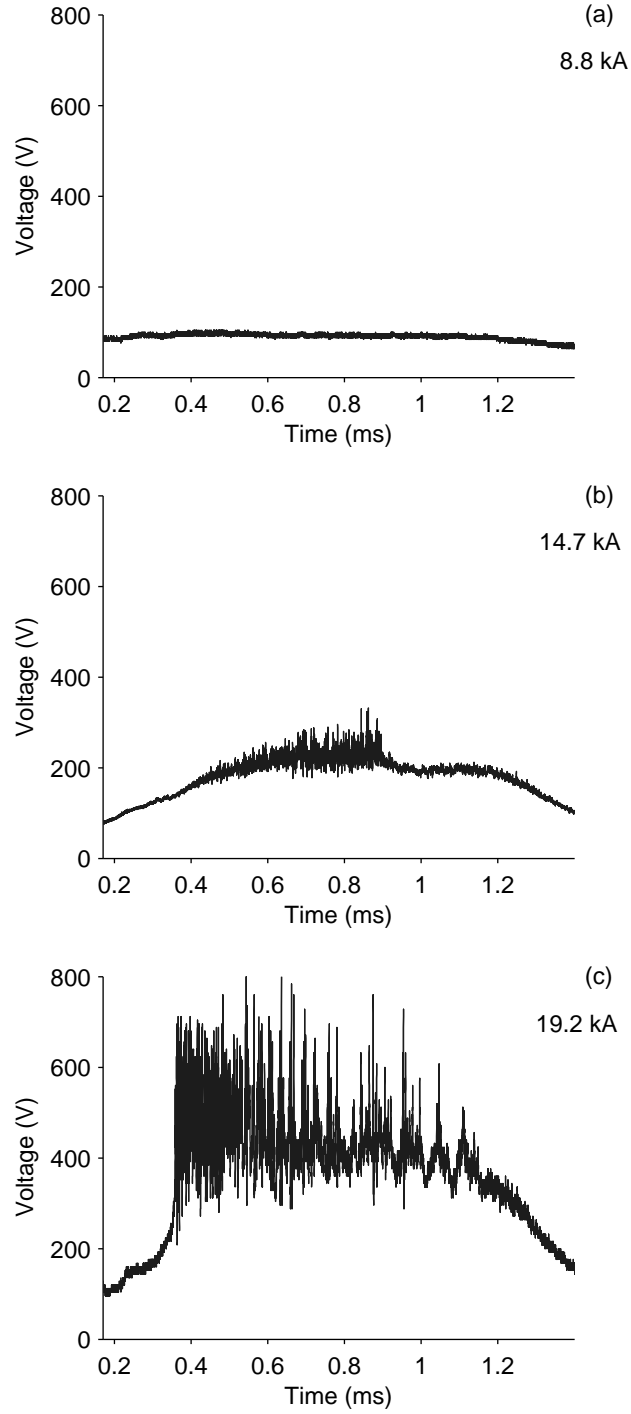


Figure 3.1: The quasi-steady voltage traces for  $\dot{m} = 3$  g/s argon, at three currents, showing the progression of the voltage hash with rising current. The currents correspond to  $J^2/\dot{m} = 26, 72$ , and  $123$  kA<sup>2</sup>-s/g, respectively.



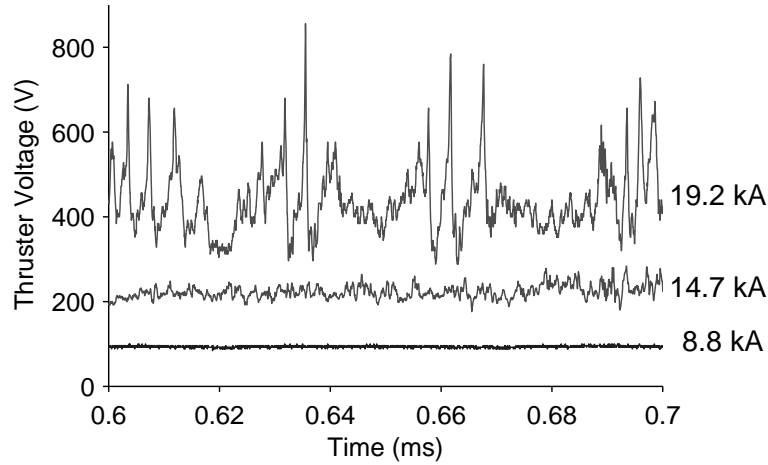


Figure 3.2: A 100  $\mu\text{s}$  portion of the three voltage traces of Fig. 3.1, plotted on the same axes.

measurement—is termed a “signal”. Signals fall into two broad categories, depending upon whether the experiment that produced them can be repeated to yield exactly the same measurement multiple times. In the case where it can, the signal is called “deterministic”; otherwise, it is called “random”. Random and deterministic signals are further classified according to their nature: deterministic signals can be either periodic or nonperiodic, and random signals can either be stationary or nonstationary (according to whether their statistical properties remain constant over time). Deterministic signals are classed as “periodic”, in one sense or another, if their Fourier spectra consist of distinct frequencies, or transient if their spectra are continuous functions of frequency. Stationary random signals are “ergodic” if statistical properties calculated by ensemble averaging over many signals are the same as those computed by averaging over a single signal (generally the case for stationary physical phenomena). Nonstationary signals must be classified according to the individual contexts from which they arise. This breakdown of signals is summarized by the chart in Fig. 3.3.

Having thus summarized the possible classifications of general signals, it is apparent that the voltage hash is a random signal. The distinction between deterministic and random signals can be based almost exclusively on the power spectrum of the

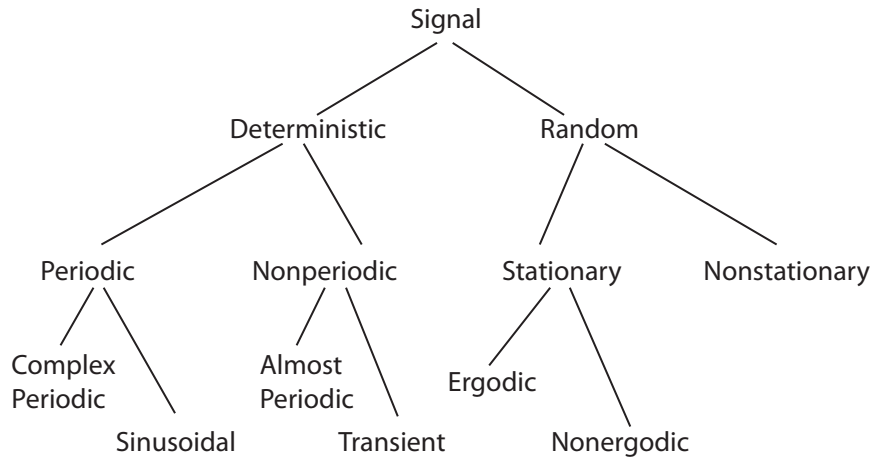


Figure 3.3: Flowchart depicting the breakdown of possible signals generated by physical processes.

signal. Referring forward to Sec. 3.5, we see that the power spectra of our voltage signals are continuous functions of frequency, rather than a set of individual peaks, which would indicate a periodic signal of some sort. And again, referring back to Fig. 3.2, it is apparent that no deterministic function of time can be assigned to the voltage signals shown therein (with the exception of the lowest current signal—below onset—which is a constant). Using these criteria, the voltage hash can be easily classed as a random, rather than a deterministic, signal.

The analysis of random signals is more complex than the corresponding analysis of deterministic signals. Whereas a deterministic signal is described by an equation with parameters that can be determined by analysis of the signal—and presumably varied by alterations to the experiment—random data must be analyzed in a statistical sense. Statistics generally calculated in the process are the mean, the spectral density (which is useful first for determining whether the signal contains any periodicity), and the probability density of the signal (which is often Gaussian about the mean, but can differ significantly from this baseline).

Applying these measures to the analysis of voltage hash presents unique challenges because each signal is nonstationary, and the statistics are therefore not constant over

the duration of each signal. For example, perhaps the most obvious feature of the voltage trace of Fig. 3.1(b) is that the voltage hash is not of constant amplitude over the course of the firing, but falls to a fraction of its original magnitude about halfway through the firing. This is not the normal behavior of hash amplitude during a firing—in fact, there is no “normal” behavior that we can ascribe to the time variation of the hash amplitude. In a series of firings under identical experimental conditions, the hash may last for the entire quasi-steady portion of the firing, or may begin and end one or more times in bursts throughout the firing. We understand, from our discussion in Chapter 5, that this behavior has to do with the release of vaporized anode material into the discharge. We cannot, however, control this behavior by any standard modifications to the MPDT—its circuit elements, anode condition, or propellant. As a result of this variability, the statistics that we calculate for the voltage hash exhibit a degree of scatter.

An example of the voltage hash statistics is shown in Fig. 3.4. This figure shows the particular voltage trace on which the statistics are calculated (with the mean subtracted), and the standard deviation, skewness, and kurtosis of the signal for 20 subdivisions, as demarcated by the dashed vertical lines in the top pane. It is clear that the statistics, whose significance we will discuss next, change throughout the course of a firing.

The positive skewness of the signal distribution is due to the tendency of the hash to spend more time above the mean value than below; the positive kurtosis occurs because the signal spends more time near the mean than it would if it were simply Gaussian distributed.

### 3.4.2 Hash Statistics for Varying $J^2/\dot{m}$ and Anode Materials

Based on our discussion in the last section, we carry out our analysis as follows. For each voltage hash trace such as that in Fig. 3.1, we extract the portion of the trace

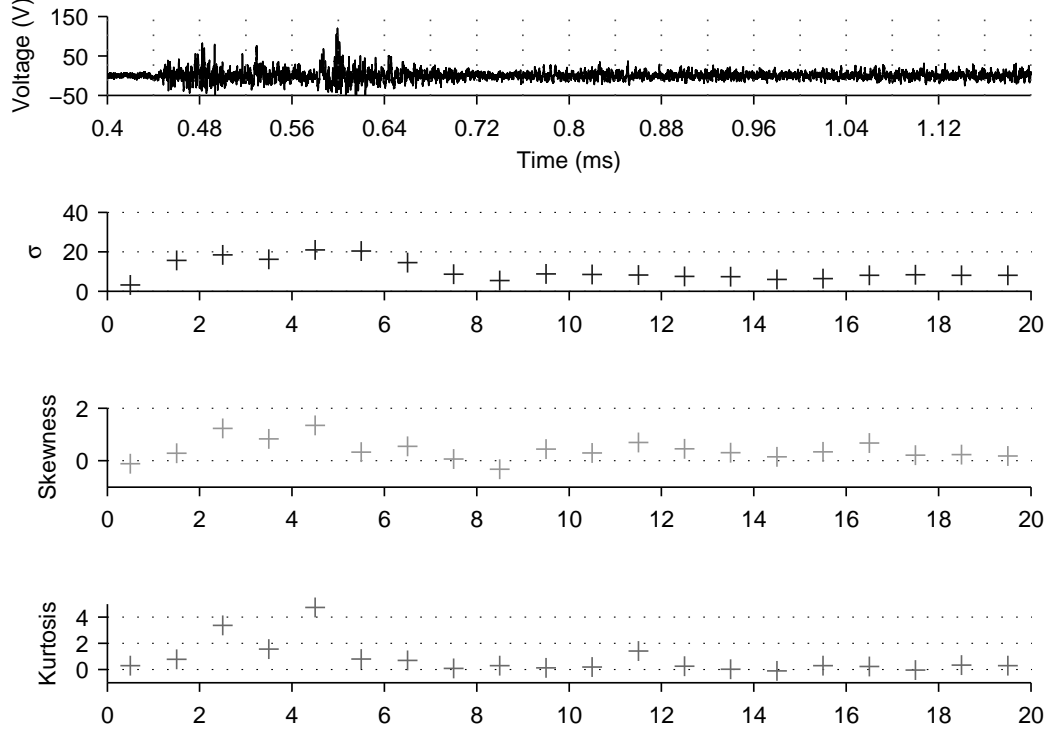


Figure 3.4: Sample statistical analysis of a signal with voltage hash.

corresponding to the time of the quasi-steady current, which lies between 0.4 and 1.2 ms. We then calculate the probability distribution of the signal during a 0.3 ms portion of this time. (Doing so is important to avoid startup and shutdown transients, which can be longer in the voltage signal than they are in the current, and can cause significant scatter in the statistics). For better spectral resolution, we calculate the power spectra using the entire quasi-steady period. The statistics and spectrum of each signal are then averaged over several identical firings. Error bars on all such quantities represent the scatter in the data. The exception to this rule is data taken with a lead anode, which sustains significant damage on each firing. Only a single firing was taken with lead at each  $J^2/\dot{m}$ , so that these data lack error bars and the power spectra have greater spectral noise.

The mean, standard deviation, skewness, and kurtosis (the first four standardized moments) of the voltage hash obtained with copper, lead, and graphite anodes are

shown as functions of  $J^2/\dot{m}$  in Fig. 3.5. The signal mean is the average voltage over the course of a firing. The standard deviation is a quantitative measure of the amplitude of the hash: for a Gaussian distribution, 95% of the voltage signal would be contained within two standard deviations of the mean. Using this measure, rather than a peak amplitude, guards against overestimating the hash magnitude in cases where an outlying fluctuation is much larger than the typical fluctuations.

The skewness is the measure of any “long tails” on either the positive or negative side of the distribution average. A positive skewness indicates that a signal spends more time above the mean value than a Gaussian signal would. (A Gaussian distribution, which has no long tails, has a skewness of zero.) The kurtosis of the signal is the measure of how “peaked” the distribution is, or how biased toward small values the signal is. A signal which spends much time near the mean, with short-duration, large excursions away will have a positive kurtosis. (Again, a Gaussian distribution has a kurtosis of zero, in our definition; other definitions assign a Gaussian a kurtosis of 3.)

The plot of the mean values is a classic voltage-current characteristic of the self-field FSBT [5]. We will not dwell on this, except to mention that at the highest currents, a lead anode appears to operate at a lower voltage than the others. Because lead provides a more copious supply of evaporated material to the discharge than the other anodes, the plasma density near a lead anode will likely be larger than that near an anode of another material, and lower voltages would be necessary to drive equivalent current through this more-conductive plasma.

The standard deviation of the voltage signals follows the same trend over the range of current for all three anodes. It is somewhat surprising that the magnitude of the hash, or the  $J^2/\dot{m}$  level at which it grows significantly, is apparently insensitive to very different anode materials. Anode evaporation, after all, has been associated with voltage hash many times in the past, and it is reasonable to think that the

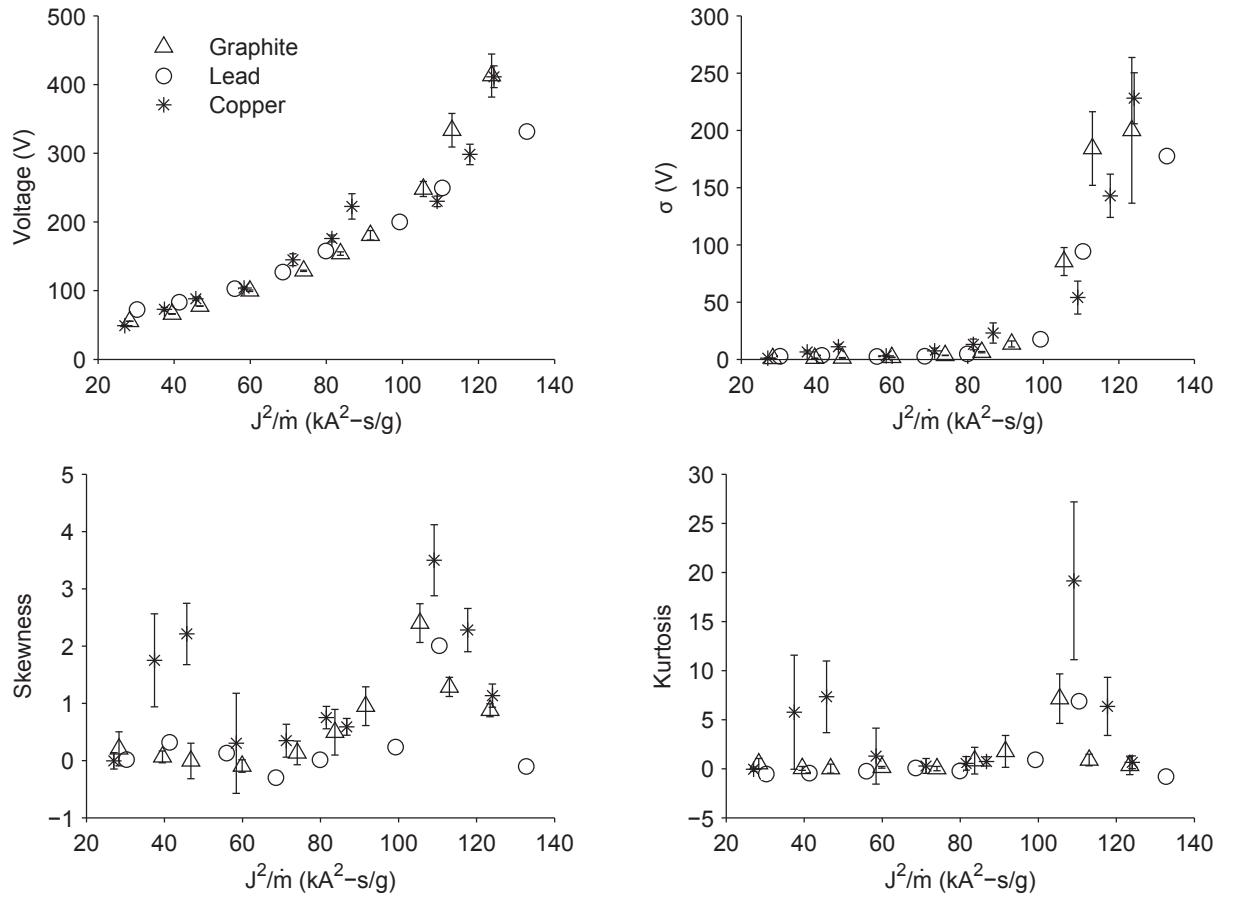


Figure 3.5: Voltage statistics for three anode materials.

one affects the other. On the other hand, it is also possible that the voltage hash arises independently of the anode damage, which is itself a passive thermal response of the anode to the mechanism behind the hash. We will explore one such possible mechanism in Sec. 3.6.

The skewness and kurtosis of the hash also follow similar trends among the materials. Each hovers around zero over most of the  $J^2/\dot{m}$  range, before rising to large positive values at the  $J^2/\dot{m}$  at which the standard deviation begins rising significantly. This happens because, as the hash grows between the magnitude levels of Fig. 3.1(b) and (c), the fluctuations first resemble infrequent, large positive excursions away from the mean. As  $J^2/\dot{m}$  rises further, these excursions become more frequent and begin to overlap, bringing the skewness and kurtosis statistics back toward their Gaussian levels. That the excursions occur above the mean gives rise to the positive skewness; the positive kurtosis occurs because the excursions rise and fall quickly. This behavior indicates that the random fluctuations in the voltage arise from ascending spikes, which relax quickly to small values. Again, we will discuss one possible origin for this behavior in Sec. 3.6.

The skewness and kurtosis for copper have a brief excursion away from zero at low  $J^2/\dot{m}$  values. This is because hash with a copper anode, unlike that with lead and graphite, does not arise smoothly out of low-current quiescent operation, but first occurs in short bursts during a single firing. This is likely due to the influence of anode erosion, which we will see in Chapter 5. Refractory graphite may not erode enough to affect the hash in the same way; lead may erode more continuously, so that the effect on the hash does not change during the firing. Copper, which as we will see erodes in bursts, lies in the middle of those two extremes.

## 3.5 Voltage Spectra

The power spectra of the MPDT voltage, whose statistics we discussed in the last section, are shown in Fig. 3.6. We have already referred to these spectra in our discussion of the random—i.e., non-periodic—nature of the voltage fluctuations.

We have already discussed, in Chapter 2, a source of corruption to which the voltage measurement is susceptible. What small portion of this corruption remains in the signal appears as a sharp peak and dip at 1.3 MHz. From the point of view of our inquiry into the physics of onset, we are uninterested in this artifact.

The spectra corresponding to firings with a lead anode display significantly more spectral noise than the others. In the case of lead, the anode sustains such significant damage with every firing that we have only taken one shot at each condition. We have therefore used no averaging in this case.

The similarity which we saw among the statistics of the three anodes in the last section is paralleled in the similarity of the power spectra for the same three anodes, an example of which we give in Fig. 3.6. All three spectra display a  $1/f^\beta$  characteristic fall over a range of frequencies above  $\sim 10$  kHz, with  $1 < \beta < 2$ . The spectra deviate from this trend at lower frequencies, but these deviations are of less interest to us than the spectra behavior at higher frequencies. A look back at Fig. 3.2, whose abscissa spans 0.1 ms, shows that the fluctuations that we associate with voltage hash happen much faster than 10 kHz: it is therefore the higher-frequency range of the spectra, with its  $1/f^\beta$  fall, that describes the hash. It is likely the case that any lower-frequency almost-periodic content is related to anode erosion, which we will discuss in Chapter 5.

Of course, in stating that the interesting part of the voltage spectra is the  $1/f^\beta$  fall shared by each spectrum in Fig. 3.6, we imply that we are less interested in deviations from a strictly straight, downward-sloping line than we are in the general downward-sloping character that we have emphasized. And while it is clear that the



$1/f^\beta$  fall is the dominant characteristic of these spectra, it is worth a few words to suggest why deviations from an ideal downward slope may exist. The most obvious deviation from an ideal line in the spectra we present here is spectral noise, which is reduced by averaging the spectra of multiple hash signals (cf. the unaveraged lead anode spectra and the averaged copper and graphite spectra). Because completely eliminating spectral noise requires computing the average over many (ideally, infinitely many) spectra, we expect that our spectra, averaged over 7–10 shots each, still contain a level of noise, which is clearly in evidence. It is possible, however, that within the spectral noise lie signatures of other processes that may occur in the self-field MPDT plasma. Tilley et. al. have shown [38] that the MPDT thruster plume is susceptible to cross-field current-driven instabilities, in particular the generalized lower-hybrid drift instability and the electron cyclotron drift instability. In their study, power spectra of ion density and temperature measurements show clear periodic content (strong peaks) that correspond to the saturated state of each of these instabilities. While such instabilities will not necessarily manifest themselves as strong periodic content in the thruster voltage signal—the voltage is a measurement averaged over the entire thruster plasma, whereas density and temperature are local quantities—it is possible that these instabilities, and others like them, may contribute to some of the deviation from ideal  $1/f^\beta$  voltage hash spectra. Whether or not this is the case, however, these instabilities were shown by Tilley et. al. to exist *below*  $(J^2/\dot{m})^*$ —and so are not fundamentally related to the voltage hash. Neither of these two—the most likely two—sources of deviation from ideal  $1/f^\beta$  behavior in the voltage hash spectra bears directly on our study of onset, and we therefore choose to focus our attention on the consequences of the power-law behavior.

The  $1/f^\beta$  characteristic fall in the spectra is characteristic of a Brownian motion ( $\beta = 2$  is true Brownian motion, while  $\beta < 2$  is a fractional Brownian motion), and is revealing with regard to the mechanism underlying the hash [39, 40].

Whereas a white noise process, which has a flat spectrum, is generated by choosing a random value for each point in the signal, a Brownian motion (specifically, for  $\beta = 2$ ) is generated by choosing a random value for the *slope* between each two points in the signal—and hence the Brownian motion is the integration of white noise. The spectrum of an integrated white noise signal falls off with a slope  $\beta = 2$ . As we consider the physical process behind the voltage hash, therefore, we must keep in mind that the underlying randomness in the signal is not in the sampled voltage values themselves, but in the voltage change between consecutive samples. We will use this insight in Sec. 3.6 to develop a random model for the hash.

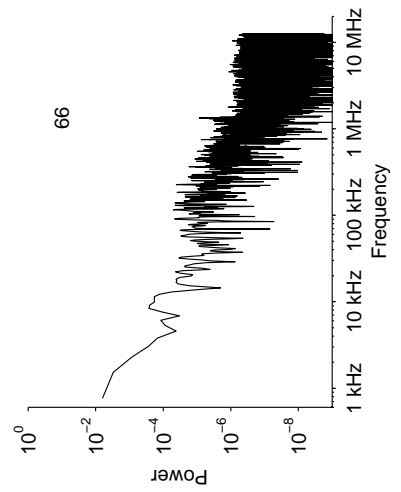
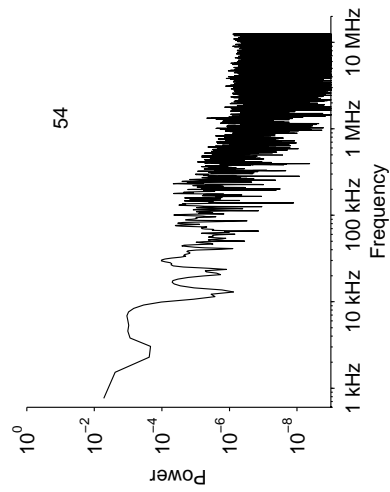
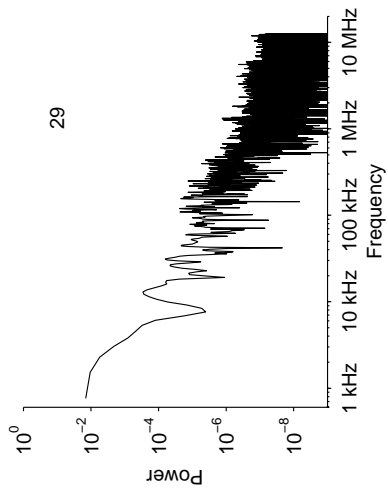
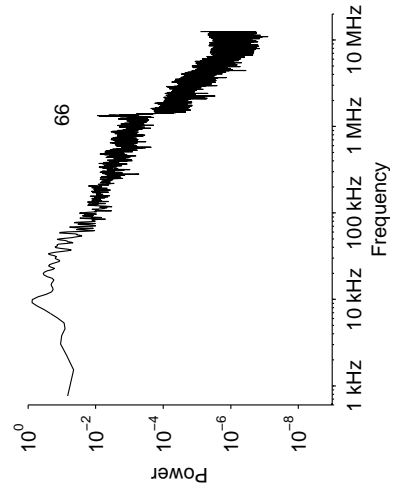
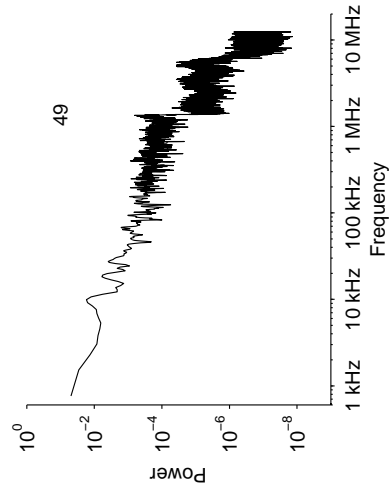
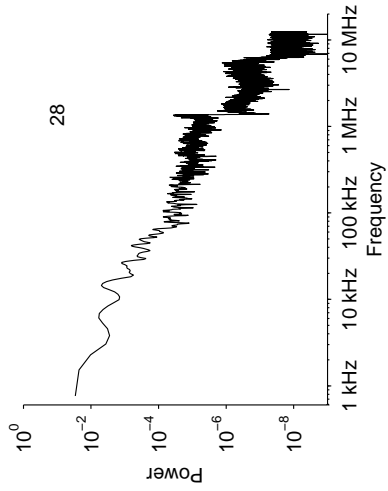
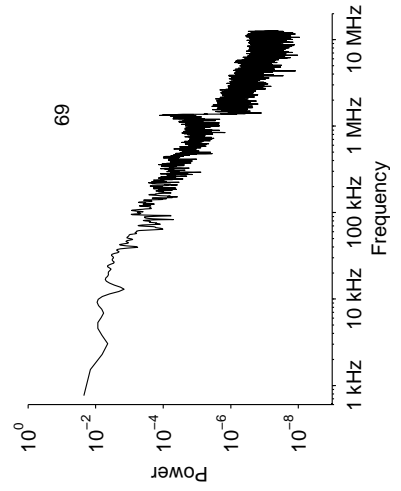
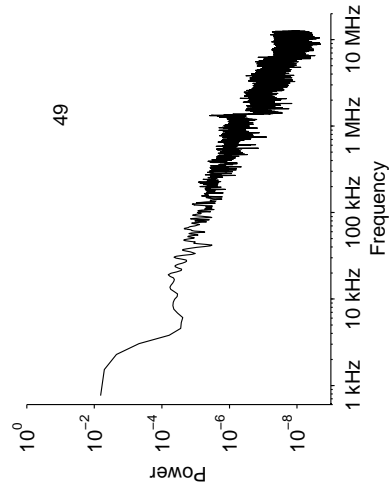
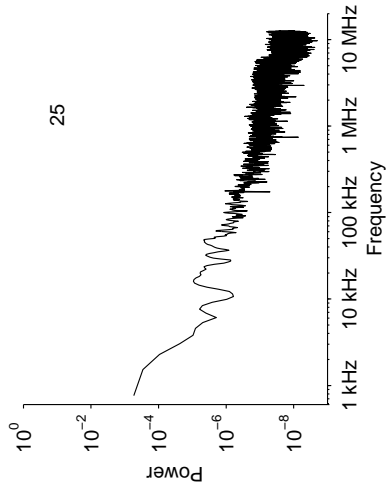
## 3.6 The Origin of Voltage Hash

### 3.6.1 Model of Random Superposition of Events

Because the voltage hash, as we have presented it in the preceding sections, is an essentially random process, modeling based on deterministic mathematics is inappropriate. Instead, in this section we will offer an explanation for what is occurring during voltage hash based upon a random superposition of events that are likely to occur in a current-starved MPDT that is susceptible to anode spotting.

Anode spots differ from the better-understood cathode spots in that they are not the sole conductors of current to the anode, whereas large arc currents from a cold cathode are usually collected solely in a number of spots [41]. Current to the anode may also be diffusely collected. In this sense, the definition of an anode spot is a local region on the anode surface of higher current density (higher conductivity) than the surrounding, diffuse regions.

Because an anode can only diffusely collect an amount of current up to the electron saturation current, any further current driven through the anode will either be conducted by spots, or will appear as a voltage rise across the anode sheath. The



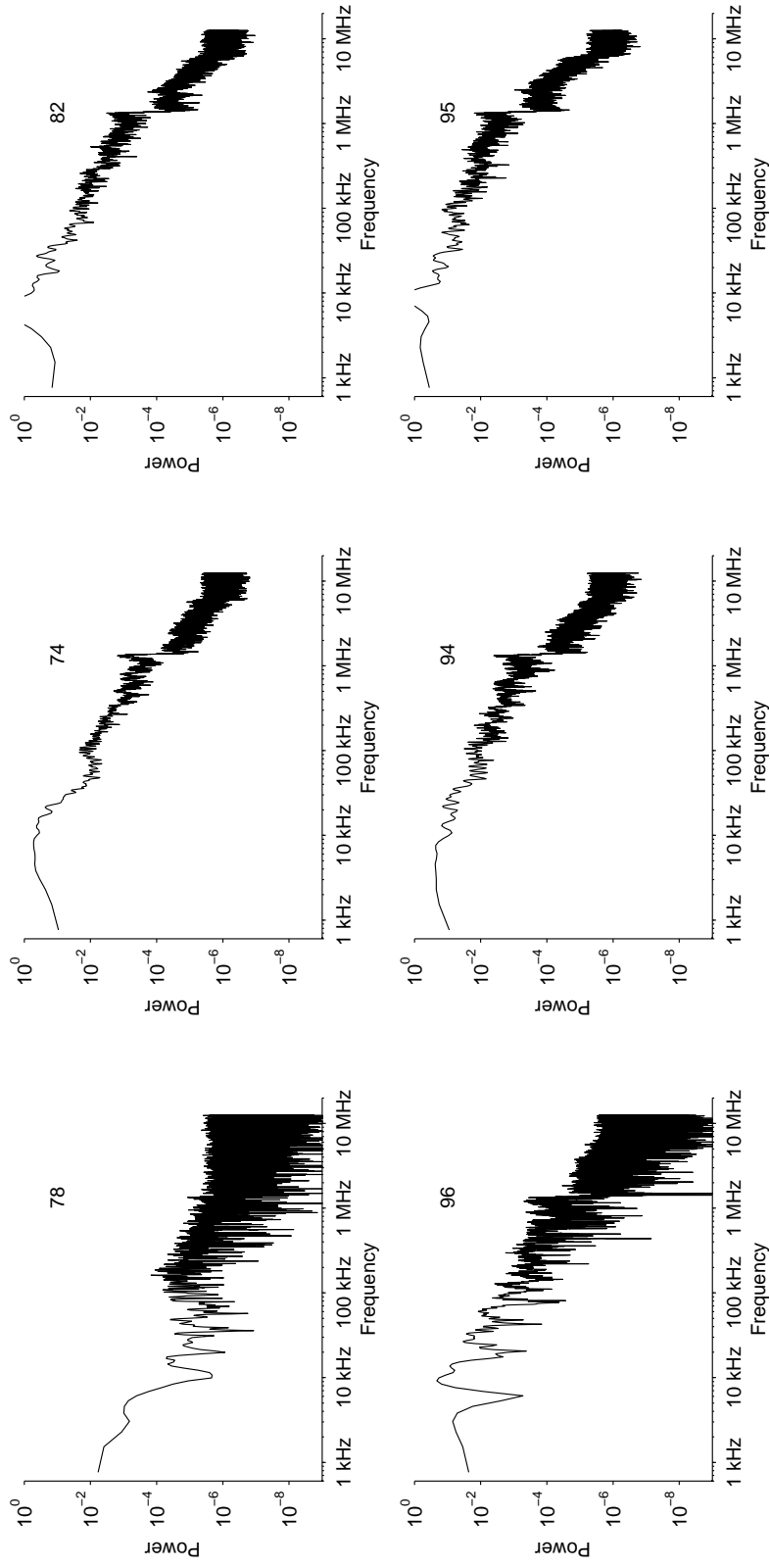


Figure 3.6: The power spectra of voltage signals for lead (left), copper (middle), and graphite (right) anodes at the values of  $J^2/m$  indicated.

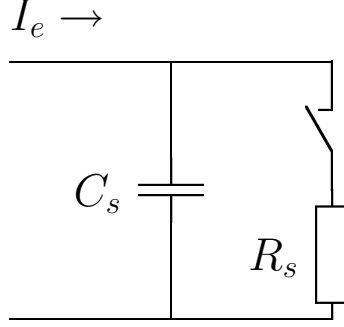


Figure 3.7: Parallel  $RC$  model of anode sheath and single spot.

sheath/spot interaction can be thought of as the parallel combination of the sheath capacitance and the spot resistance. Figure 3.7 shows this parallel combination and a switch whose opening and closing represent the extinction and ignition of a spot, respectively. The indicated current  $I_e$  is the difference between the electron saturation current of the MPDT anode/plasma combination (diffuse current collection) and the current being driven through the thruster by the PFN ( $I_e = I_{PFN} - I_{sat}$ ).

If the power supply is sufficiently inductive (stiff)—as in our experiment—then  $I_e$  is unaffected by the change in voltage across this combination as the capacitor charges and discharges. The voltage across the capacitor when the switch is opened, therefore, rises linearly with time and is

$$V_c = \frac{I_e}{C_s} t. \quad (3.1)$$

When the switch closes, the voltage across the combination falls as the capacitor discharges through the resistor, according to

$$V = V_c e^{-t/R_s C_s}. \quad (3.2)$$

The ratio of the rise and fall times of the voltage is  $V_c/R_s I_e$ . Experimental measures of  $I_e$  are difficult to obtain, but since we do not, in general, observe voltage rise rates of greater than  $100 \text{ V}/\mu \text{ s}$ , and the value of the sheath capacitance is on the

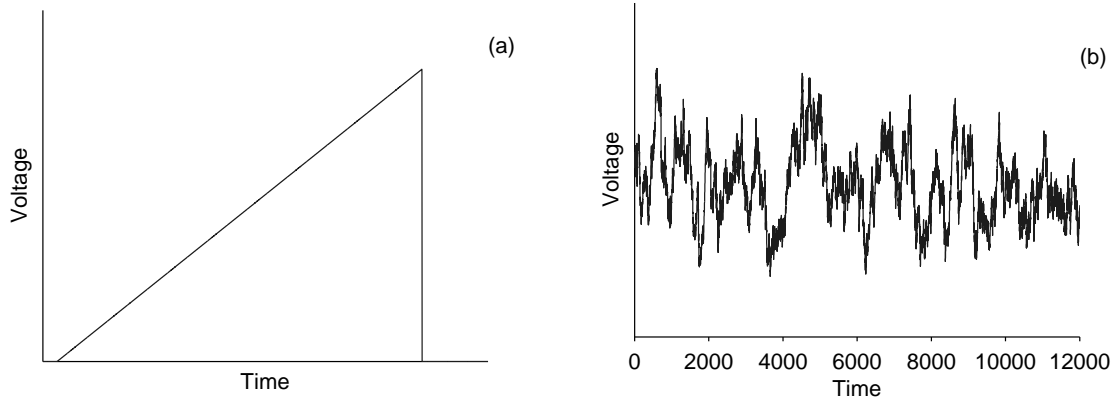


Figure 3.8: The voltage change caused by (a) a single starvation/spotting event; (b) random superposition of many such events.

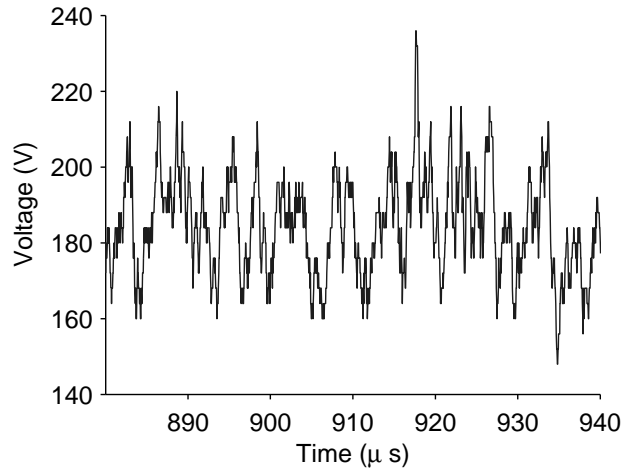


Figure 3.9: Experimental realization of voltage hash, for comparison with the simulated signal in Fig. 3.8(b).  $J^2/\dot{m} = 72 \text{ kA}^2\text{-s/g}$ .

order of 100 nF [42],  $I_e$  is likely no larger than  $\sim 10 - 100 \text{ A}$ . Since the resistance of the thruster plasma as a whole is on the order of 10 mΩ, and  $R_s$  should be smaller than this value, we expect that in a typical spotting cycle the rise time will be longer than the fall time. Experimentally, as well, we observe voltage fall times to be much shorter than the rise times, when we are able to distinguish individual rises and falls.

A single spotting event will therefore look something like the ramp in Fig. 3.8(a), where the specific values of time and voltage are dependent upon the parameters and the fall time here is shown much smaller than the rise time.

If we take this process to be indicative of what occurs across the anode sheath in the MPDT, then a full picture will include many anode spots (and the number may change with time), each having their own resistance  $R_s$ , but all sharing the same sheath capacitance  $C_s$ . The voltage that we measure across  $C_s$  will therefore be the superposition of the activity of all the spots—or, in the parlance of our model, the superposition of many switching events.

The picture we propose is consistent with our experiment under the following conditions:

- *The current carried by each spot is sheath-limited in its steady-state.* This ensures that when a spot extinguishes, the current it had carried goes to charging the sheath capacitance, rather than being redistributed to other spots. Were this not the case, we would expect no more than one high-conductivity spot to form, inconsistent with our observations.
- *The spotting events are uncorrelated.* The randomness seen in our experiments shows no deterministic correlation. It is not immediately apparent, in a physical context, in what way distant spots would communicate strongly with one another—so we expect this assumption to be reasonable.

If we now take a random superposition of many events such as that in Fig. 3.8(a) the signal that we generate appears as that in Fig. 3.8(b). This particular instance is a segment of a signal generated by 4096 events randomly distributed into a time span of 16384 (in which the units are arbitrary). The rise times were randomly distributed between 2 and 512, and the amplitudes chosen randomly on the interval  $[0,1]$ . The vertical axis remains unlabeled as the amplitude of the signal can be arbitrarily scaled with the maximum event amplitude chosen. As a comparison, a segment of a real voltage trace exhibiting hash, for  $J^2/\dot{m} = 72 \text{ kA}^2\text{-s/g}$ , is shown in Fig. 3.9.

The generated signal in Fig. 3.8(b) is an accurate reproduction of the voltage

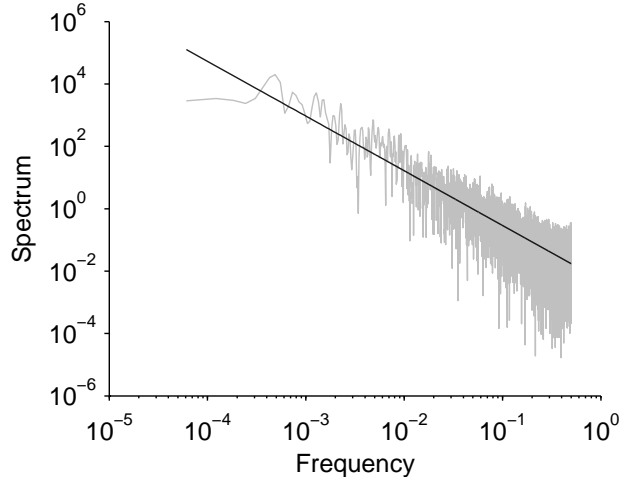


Figure 3.10: The power spectrum of the signal in Fig. 3.8(b).

hash. This signal is, like the voltage hash, a random walk, generated by the random superposition of deterministic functions. The power spectrum of this signal is shown in Fig. 3.10. The superimposed fit line on this graph corresponds to the function  $1/f^{1.75}$ : the power spectrum of the generated noise has a power-law drop whose exponent is, like those of the experimental voltage hash, between 1 and 2. It is clear why: by randomly superimposing many linear rises in this way, we have created a signal whose slope between any two points is a random variable. As we discussed in Sec. 3.5, this gives rise to a Brownian motion such as the one we have just calculated.

The statistics of our generated signal depend upon the average occurrence rate  $n$  of the events, and upon the rise time  $\tau$  of the events. The mean and standard deviation, as we have already pointed out, can be arbitrarily scaled according to the characteristic amplitude of the events; the skewness and kurtosis of the signals, on the other hand, show a tendency toward zero as the product  $n\tau$  rises—that is, the signal becomes more Gaussian as the events increasingly overlap. These trends are shown in Fig. 3.11. The range spanned by these statistics cover the entire range of statistics calculated for the experimental voltage hash in this chapter.



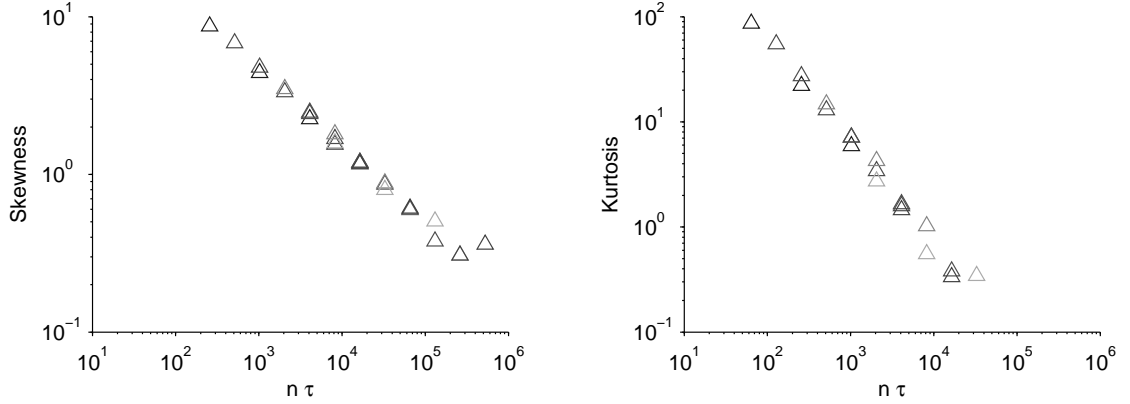


Figure 3.11: Skewness (left) and kurtosis (right) of generated signals with various  $n\tau$  values.

### 3.6.2 Discussion

We can use our understanding of this simple model to gain some physical insight from the experimental hash statistics. Both the skewness and kurtosis of the experimentally measured hash of Fig. 3.5 evolve with  $J^2/\dot{m}$ , both reaching a peak at the same  $J^2/\dot{m}$  value. We can picture the evolution of the statistics from Gaussian, to a distribution with significant skewness and kurtosis, then back toward a Gaussian, as a movement first to the left, then back to the right, along the curves of Fig. 3.11. This indicates that the product  $n\tau$  first decreases as  $J^2/\dot{m}$  increases, and then reverses. Physically, we may understand this in the following way. The occurrence frequency  $n$  is related to the average number of spots that are carrying current during a thruster firing: it is the ignition, and extinction, of each of these spots that creates a single event.  $\tau$  is representative of the current carried by a spot: the higher the current, the greater the slope of the voltage rise when the spot extinguishes, and the shorter the rise time if the voltage is not to increase to arbitrarily large values. Our data suggest that at first  $\tau$  falls faster with current than  $n$  rises, so that  $n\tau$  falls, and the hash statistics become significantly different than Gaussian. At sufficiently high current, however, increasing  $n$  catches up with the falling  $\tau$ , so that  $n\tau$  falls again and the statistics return toward Gaussian.

The implication of this for our understanding of anode spotting and voltage hash can be stated simply. In order to carry increasing thruster current in the anode-starved onset condition, anode spots must either carry more current each or a greater number of anode spots must form. Our evidence suggests that in the intermediate  $J^2/\dot{m}$  range, the current carried (or spot size) first grows in response to increasing thruster current; past a particular  $J^2/\dot{m}$  ( $\sim 110 \text{ kA}^2\text{-s/g}$ , in our data), the number of spots then increases.

This interpretation of Fig. 3.5, in which we associate the return of the statistics toward Gaussian with an increasing number of anode spots, implies that an effective mechanism for anode spot creation becomes dominant above  $J^2/\dot{m} \sim 110 \text{ kA}^2\text{-s/g}$ . Because this  $J^2/\dot{m}$  value is independent of the anode material, we expect that this mechanism is an instability in the plasma that drives the constriction of diffuse current into high-current, high-conductivity channels. A phenomenon similar to the anode spots that we have observed here, and in the references, is current filamentation, which is observed in coaxial plasma accelerators such as the plasma focus [43, 44]. The current filaments observed in the plasma focus exhibit some of the properties that we have inferred about anode spots, such as a limit on the filament current [44]. A number of mechanisms, such as thermal instabilities and ion-acoustic instabilities, can give rise to filamentation in plasmas [45, 46]. The drivers of these instabilities are present in the near-anode MPDT plasma as  $J^2/\dot{m}$  rises. With rising  $J^2/\dot{m}$ , the electron drift velocity and the specific power input to the plasma increase, and one of these instabilities may be excited. If the exciting of a thermal or drift instability causes the current to filament, the number of unsteady anode spots will increase. Should a detailed study of the relevant threshold parameters for these instabilities—which is beyond the scope of this work—uncover one such threshold that is equivalent to  $J^2/\dot{m} \sim 110 \text{ kA}^2\text{-s/g}$  in the FSBT, this will support our hypothesis that the mechanism behind the increasing number of anode spots after this  $J^2/\dot{m}$  value is

current filamentation.

### 3.7 A Further Word on Filamentation in the MPDT

In the last section, we did not suggest the presence of filamentation in the MPDT plasma without some prior observational evidence. We first encountered the possibility of current filamentation in high-speed photographs of the MPDT anode plasma taken at conditions above  $(J^2/\dot{m})^*$ . As an example, a sequence of several photographs with exposure time of  $11\ \mu\text{s}$  are shown in Fig. 3.12. The box over the MPDT illustration shows the portion of the thruster photographed. Bright sections of each photograph in the grid below the illustration are luminous plasma regions. The core of the MPDT plasma is just visible at the bottom of each photograph, and in each (save the last), several luminous channels—which we will refer to as filaments—exist between the core MPDT plasma and the anode face. The last photograph captures several quiescent microseconds, and is representative also of the appearance of the thruster operating at conditions below  $(J^2/\dot{m})^*$ , when filaments never appear. Since the filaments in the photographs do not appear as streaks, it is clear that they do not move over the anode surface during the exposure time of the photographs. (As we will see in Chapter 4, streaked melting on the anode surface indicates that anode attachments do move, if their lifetime is long enough. What we see here is that the movement is not an essential characteristic of all filaments.)

Multiple filaments appear in each photograph, and we assume that more must form on the anode in those regions not covered by the photographs. We also expect, based on observation of anode damage patterns (more on this in Chapter 4) that many more filaments may form on the anode inner lip, where we cannot observe them. Still others may not be sufficiently bright for us to observe. We therefore expect that, at any one time, there are multiple filaments acting on the anode, and that their lifetimes

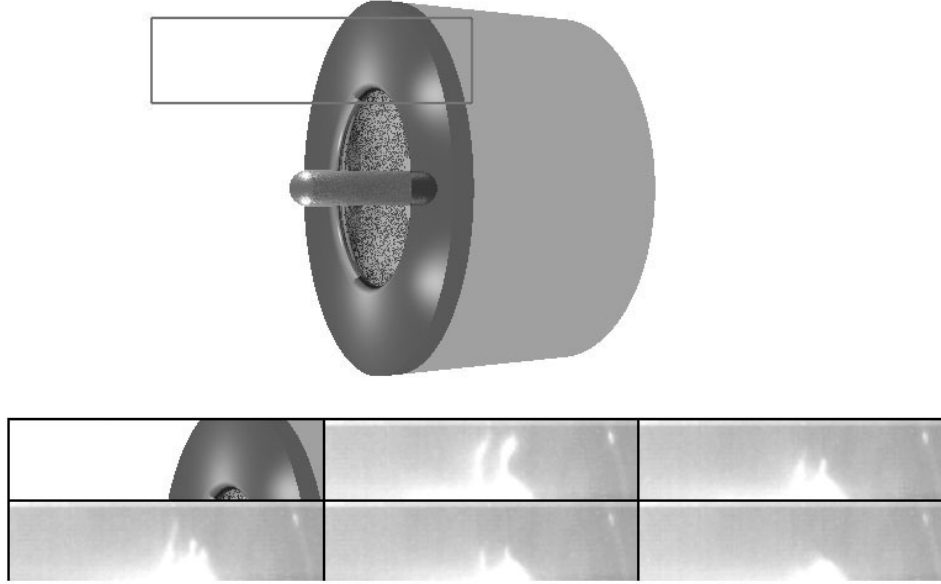


Figure 3.12: Several sequential frames ( $11\ \mu\text{s}$  exposure) of a high-speed video showing current filaments at the anode.

are something shorter than the exposure time of the photographs ( $11\ \mu\text{s}$ ). These observations are consistent with the assumptions that went into the random event model of the voltage hash presented earlier in this chapter, and with our interpretation of the voltage hash as a phenomenon influenced by current filamentation.

### 3.8 Summary of Results

In this chapter we have provided the a detailed examination of the onset voltage hash generated in an MPDT, and in doing so have been able to draw a number of conclusions about the process that generates the hash. The most important of our conclusions are:

- *The voltage hash is a random process.* No non-statistical description of the hash, whether transient or periodic, is appropriate. The characteristic frequencies discussed in the literature are either a misinterpretation of the fluctuations, or are caused by a source of corruption such as the power supply.

- *Anode material is not of primary importance to the hash properties.* The evolution of the hash statistics with  $J^2/\dot{m}$  takes place without a significant dependence on the anode material. The statistics show in particular a reversal from the trend away from Gaussian statistics to a trend back toward Gaussian at the same value of  $J^2/\dot{m} \sim 110 \text{ kA}^2\text{-s/g}$ , irrespective of the anode material.
- *A increased production of anode spots occurs above  $J^2/\dot{m} \sim 110 \text{ kA}^2\text{-s/g}$ .* By comparing our data with our hash model, we conclude that with rising  $J^2/\dot{m}$ , current is first carried to the anode by increasing the current carried by each spot; but at  $J^2/\dot{m} \sim 110 \text{ kA}^2\text{-s/g}$ , the number of spots then begins to increase. We have suggested that the excitation of a filamentation instability is responsible for this increase in the number of active anode spots, and we have presented photographic evidence of the existence of current filaments in the MPDT.

We have reached each of these conclusions by consideration of the statistics of the random voltage signals. We see that the voltage hash, which at first look appears to be simply noise, contains a good deal of information pertaining to the process that created it. We have described a model to show how anode spots may give rise to onset voltage hash, and have shown that the behavior of the hash statistics is consistent with this picture. While we have found that changes in anode material do not alter the hash statistics, we will see in the chapters that follow that the anode damage is very dependent upon the anode material used, and that the *stationarity* of the statistics, as we have already mentioned, is affected by the evaporation of anode material.

# Chapter 4

## Patterns of Anode Damage

### 4.1 Introduction

In Chapter 1, we made the case that a better understanding of the two main phenomena that are associated with operation above  $(J^2/\dot{m})^*$ —voltage hash and anode damage—is necessary before a creative way to overcome the onset problem can be devised. In Chapter 3, we gained a better understanding of the voltage hash, observing that it is a random fluctuation without any particular characteristic time scale, and without dependence upon what material the anode was made of. In this chapter, we seek to accomplish the same goal with respect to the anode damage. We start with a short review of the previous literature regarding anode damage, and then proceed to describe our experiments, the observations of anode damage that they enable us to make, and the insights we may draw from them.

### 4.2 Background

Little systematic investigation of anode damage exists in the MPDT literature. It is common to encounter descriptions of onset that refer generically to “ablation” or “erosion” of various thruster components, including the electrodes [7, 9, 30]. Some

references are more specific, saying that the electrodes melt [47]. Still others will identify the anode as the primary component to suffer damage [10, 48]. In all these studies, however, the manner in which the anode is damaged is not specified beyond these generic descriptors.

Those authors who have written more descriptive accounts of the damage suffered at the anode refer to anode spots [10, 19, 48]. Even these accounts, however, leave unspecified what these spots are. The most descriptive work is that of Diamant [14], in which photographic evidence of spots is provided. In Diamant’s work, the appearance of spot damage on the FSBT anode was not consistent among the varied conditions of the experiments. For example, in the case of a polished aluminum anode, the “spots” were macroscopic radial streaks across the anode lip—discolored but not obviously melted—whose severity grew worse as the current increased; for a polished copper anode, the spots were darkened circular features, small enough to require microscopic magnification. In the case of roughened anodes, the aluminum spots were macroscopic darkened areas that were frequently melted, and more so with increasing current; copper spots were macroscopic darkened areas without obvious melting. The state of knowledge of anode damage, therefore, consists of this ill-defined concept of the anode spot, whose properties are far from uniform across experimental conditions. It is our purpose in the remainder of this chapter to present more systematic observations of the anode damage.

### **4.3 The Effect of Contamination and Boundaries**

To present reliable results regarding patterns of anode damage, we must understand what these patterns depend upon. In the results of Diamant [14], a roughened anode experienced damage considerably different than a smooth anode. Also, in previous photographic studies [13], a significant amount of arc activity along the outer

boundary of the anode, where the conductor is insulated from the arc, is typically ignored. Our own experience, and that of researchers observing anode phenomena in other arcs [49, 50] suggests that the presence of contaminants anywhere on the anode can change the pattern of damage experienced. Based on these observations, we carried out a succession of experiments to ascertain to what extent boundaries and contamination significantly altered patterns of damage on the anode. In the following section, we will demonstrate that arc damage preferentially appears along anode-insulator interfaces, particularly when the insulator is easily evaporated by the arc.

#### **4.3.1 Anode Damage Attractors**

For this test, we intentionally contaminated a polished copper anode in eight sections (a–h), each in a different way, as shown in Fig. 4.1. The anode is contaminated in such a way as to provide ample boundary between the contamination and the anode metal. The anode is contaminated as follows, with respect to the figure:

- (a) Kapton (high-voltage insulator)
- (b) Copper oxide (water damage)
- (c) Clean (control)
- (d) Epoxy polymer
- (e) Silicon oil
- (f) Air-set cement
- (g) Clean (control)
- (h) Graphite powder



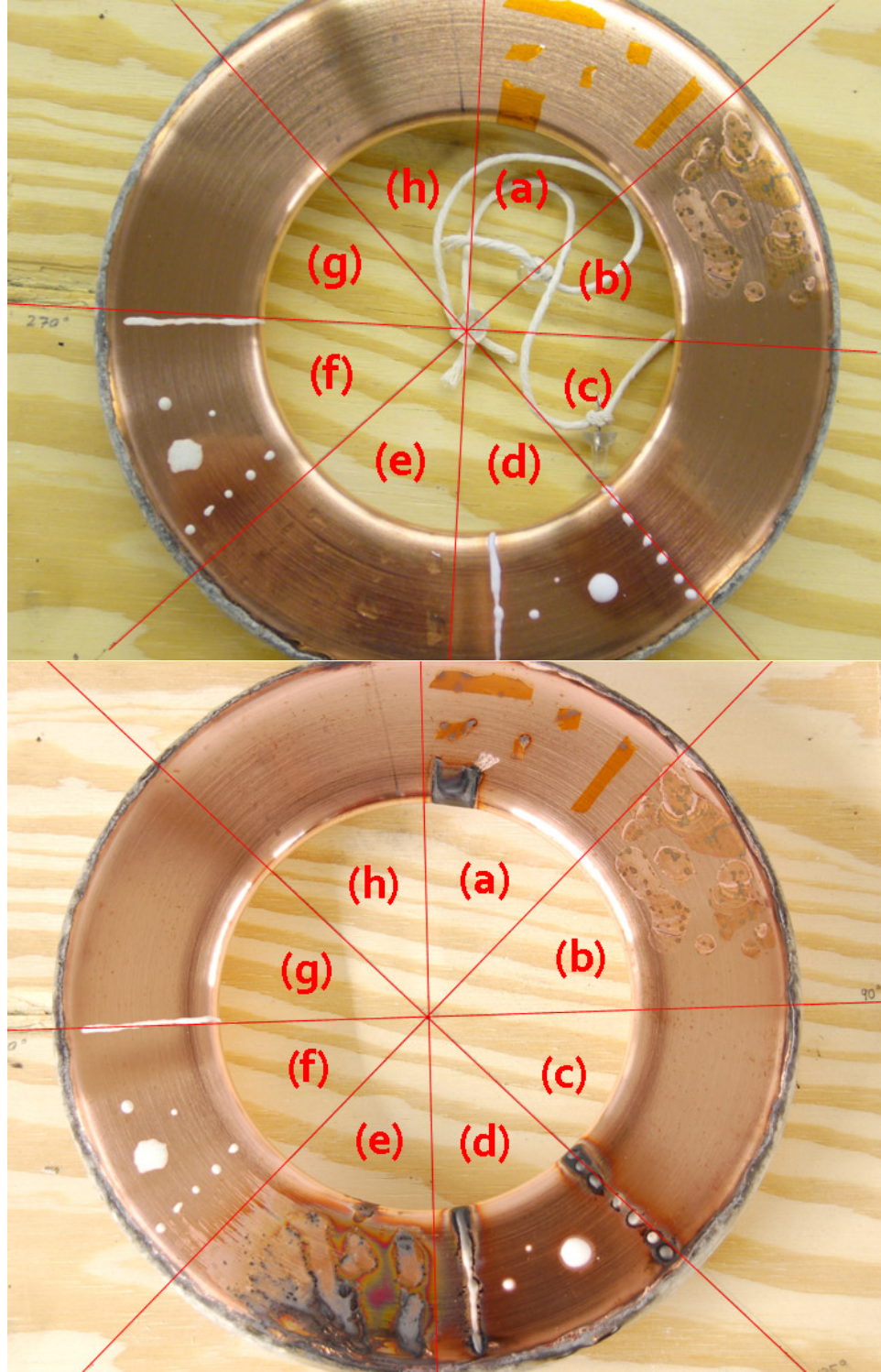


Figure 4.1: A deliberately-contaminated copper anode before (top) and after (bottom) 10 firings above onset ( $J^2/\dot{m} = 120 \text{ kA}^2\text{-s/g}$ ). Contamination is (a) Kapton; (b) Water damage; (c) Clean [control]; (d) Epoxy polymer; (e) Silicon oil; (f) Air-set cement; (g) Clean [control]; (h) Graphite powder.

It is apparent from the figure that certain forms of contamination attract more anode damage than others. Kapton, epoxy polymer, and silicon oil show a marked tendency to blacken around the boundaries and to initiate melting streaks, as is most clearly seen in section (a). Close inspection reveals that the blackened areas are populated with small spots of clean, melted metal. The three most effective contaminants have two characteristics in common, one of which is lacked by each of the other contaminants: each is non-conducting and easily evaporated under the action of the arc. (The air-set cement, for example, is non-conducting but, as a ceramic, has a high heat tolerance.)

Evidently, the current concentrates along the boundaries between insulator and anode, as electrons which would otherwise enter the anode through the area now covered by the insulator are diverted by an electric field to the nearest possible point of entry (see Fig. 4.2 for a diagram). The passage of electrons along the boundaries heats the insulator, which evaporates significantly if it is of a high vapor pressure. This evaporation raises the density, and so enhances the conductivity, of the near-anode plasma, further concentrating the current. The concentration in current is sufficient to melt the anode metal. By contrast, since a more refractory insulator does not evaporate easily, one mechanism for current concentration is lacking, and these insulators are less likely to attract damage to their boundaries.

Figure 4.3 shows an all-light, time-integrated photo of a single firing with this contaminated anode. The anode, when mounted on the thruster, is oriented with respect to the reader as in Fig. 4.1. The bright light surrounding the boundaries of the three most effective contaminants (regions (a), (d), and (e)), which indicates that the energy input is higher in those locations than elsewhere, matches identically the damaged appearance of the anode surface in Fig. 4.1; likewise, the darkness over other regions corresponds to the lack of damage in those same regions.

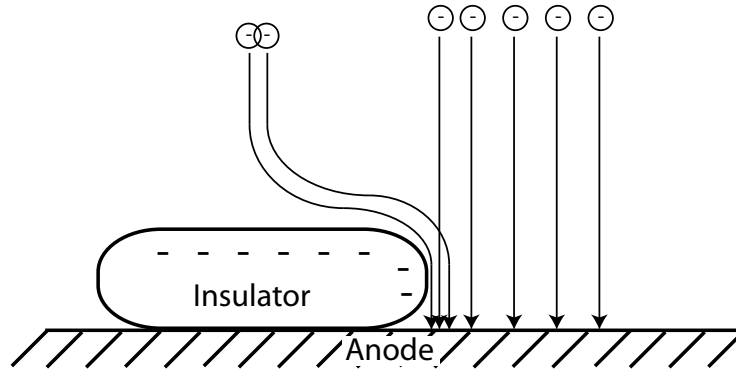


Figure 4.2: Sketch of the movement of electrons around an insulating boundary. The insulator surface is negatively charged, due to the electron flux to its surface; this negative charge alters the anode electric field, which turns the incoming electrons and moves them to the nearest point of entry. This concentration enhances the heat flux at the insulator boundary.



Figure 4.3: An all-light photograph of the integrated light output of the FSBT with the contaminated anode of Fig. 4.1.

One further comment should be made regarding the influence of boundaries on the anode damage. Referring again to Fig. 4.3, a bright ring of light surrounds the anode at the outer boundary. This boundary is unavoidable, for the arc must be contained to the inner and front anode surfaces if the current pattern is to provide thrust by  $\mathbf{j} \times \mathbf{B}$  forces. The current concentration, and corresponding anode damage, along this boundary cannot be eliminated by choice of the insulating material.

In the discussion of anode damage in the next few sections, we will not discriminate between damage along the outer boundary of the anode, and damage elsewhere, for two reasons: first, the form of the damage is different between the boundary and elsewhere only in predictable ways; and second, from a thruster lifetime point of view, anode erosion *anywhere* is a significant concern, and we are well advised to ignore none of it.

## 4.4 Anode Spot Damage

The last section demonstrates the importance of anode cleanliness to the study of damage. In this section, we will discuss the damage sustained by aluminum and copper anodes; we leave for the next section discussion of the special cases of lead and graphite. We polished the anodes in this study on a lathe with a succession of increasingly fine sandpapers, and finished the polishing with a 1  $\mu$  diamond suspension. (This last step is not essential; the nature of the damage is unchanged after the anode is polished beyond a roughness of a few  $\mu$ .) Oils and polishing residue were removed with acetone, and we handled the anode with gloves to ensure that the surface remained free of oils after cleaning.

Anodes cleaned and handled in this way were installed on the thruster, and first further cleaned by a series of low-current (8 kA) firings. (The shape of the voltage trace evolves over the course of the firings, settling down to a constant value after

about 20 shots. The anode is not damaged, nor indeed visibly altered in any way, by any number of these low-current shots.) We then subjected the anode to a single firing at some current above  $(J^2/\dot{m})^*$ ; we saved the voltage trace, and recorded the damage the anode endured due to this firing. In Figs. 4.4 and 4.5, we provide two example voltage traces, and photographs of the damage to an aluminum anode for two firings, one at  $J^2/\dot{m} = 60 \text{ kA}^2\text{-s/g}$ , and the other at  $J^2/\dot{m} = 85 \text{ kA}^2\text{-s/g}$ . The size and severity of the damage will be our main point of interest.

#### 4.4.1 Anode Damage Severity

The severity of the anode damage is a subjective measure. We might, for example, classify areas of the anode that have been slightly discolored, very discolored, and melted as areas with increasingly severe damage. Greater number and density of damaged areas also give the impression of greater severity.

It is clear that, of the two examples shown, the damage sustained by the anode at higher  $J^2/\dot{m}$  is more severe. At  $J^2/\dot{m} = 60 \text{ kA}^2\text{-s/g}$ , the damage is mainly discoloration of varying degrees, two small melted streaks, and a few collections of small melted points. By contrast, at  $J^2/\dot{m} = 85 \text{ kA}^2\text{-s/g}$ , melting is more extensive, deeper than in the previous case, and the abundance of damage of all kinds is larger than at lower  $J^2/\dot{m}$ .

Damage to the anode occurs in isolated points and in streaks. Either may be melted or merely discolored. The distinction between discoloration and melting is a distinction between whether or not the energy input to the anode at the damage point is sufficient to raise the temperature beyond melting. The distinction between isolated points and streaks may be either a distinction between a long and short spot lifetime (whether there is time for  $\mathbf{j} \times \mathbf{B}$  forces to push the spot along the anode surface) or between a small and large spot (large spots may naturally form in non-circular patterns).

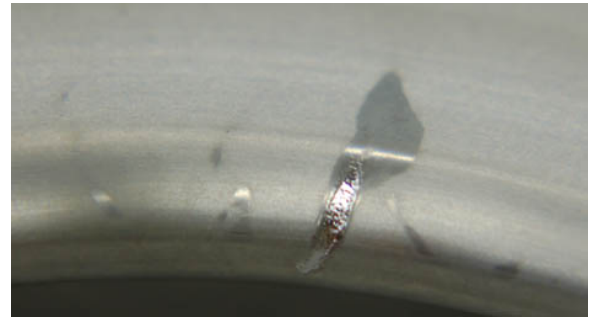
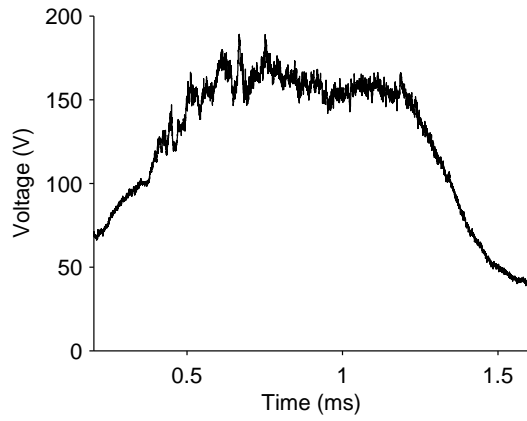


Figure 4.4: The voltage trace for a single firing at  $J^2/\dot{m} = 60 \text{ kA}^2\text{-s/g}$ , and photographs of the resulting damage to a polished anode. Damage extends from the lip to the outer face, in both a gross melting form and shiny streaks. Darkened and melted points also appear on both the lip and the outer boundary.



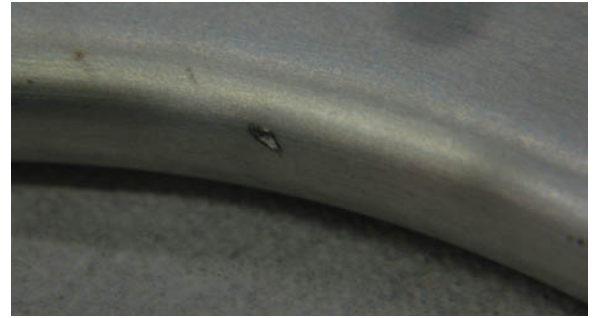
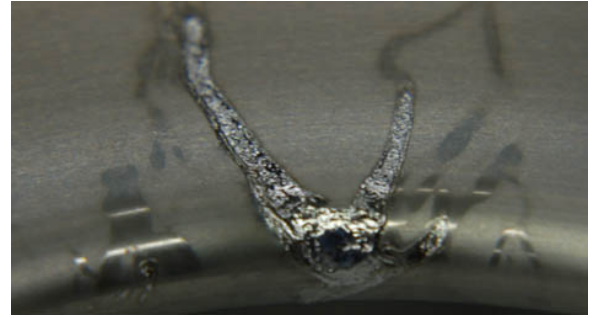
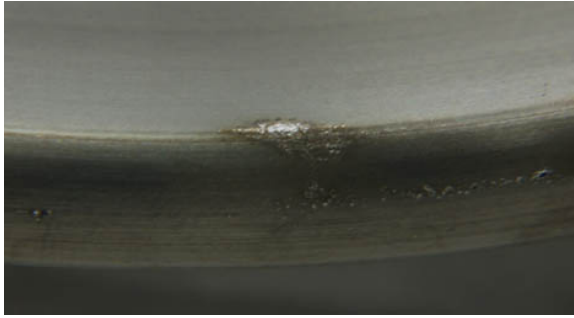
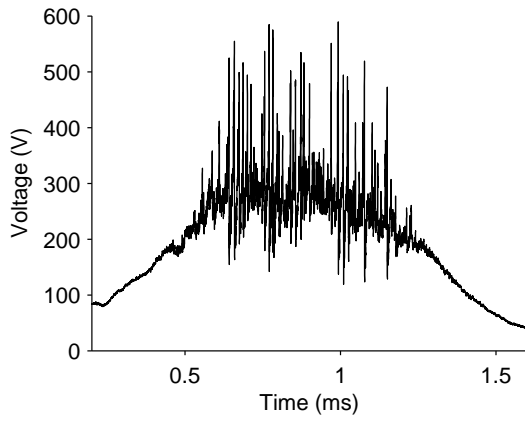


Figure 4.5: The voltage trace for a single firing at  $J^2/\dot{m} = 85 \text{ kA}^2\text{-s/g}$ , and photographs of the resulting damage to a polished anode. Damage occurs both on the lip and outer face, in patches of gross melting, shiny streaks, and darkened and melted points.

While it is clear that the severity of the damage at higher  $J^2/\dot{m}$  is greater, the character of the damage is otherwise similar between the two cases—isolated points and streaks, both discolored and melted, appear in both cases. This is the case even though the voltage hash between the two shots differ appreciably in their character, particularly in their amplitudes. That is, *the damage character is not a current-dependent quality*.

The “anode spots” that constitute the damage to the anode surface in the MPDT are not of uniform character, and appear in the distribution that they do without any intervention by the operator. Next, we make a quantitative observation of the damage pattern.

## 4.5 Distribution of Anode Mark Sizes

Though the damage that appears on the several anode materials we have used is of the same quality—spots and streaks, melting and discoloration—aluminum is the best material on which to make careful observations of the damage. (Graphite and lead, as we will see, are poor materials on which to make observations, for two very different reasons). It is clear from the figures in Sec. 4.4.1 that the damage appears in a variety of sizes on the anode surface. To measure the distribution of damage point sizes, we used the aluminum anode discussed in Sec. 4.4.1, and surveyed the damage under optical magnification. We define the size of a mark to be the diameter for roughly circular marks, or the long dimension for oblong marks. After cataloging the damage points by size, these are placed in bins according to the sizes of the points, one bin per order of magnitude. The result is the four-point histogram shown in Fig. 4.6.

Within the range of sizes catalogued, there is no characteristic damage size. Instead, there is a distribution of sizes following the power law  $1/d$ , where  $d$  is the



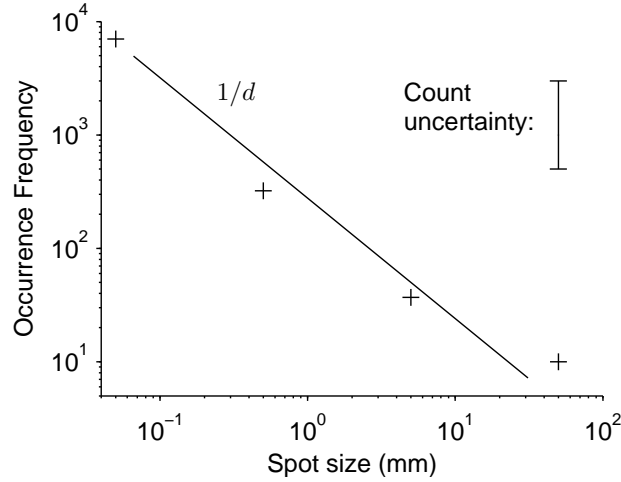


Figure 4.6: The distribution of mark characteristic sizes on a damaged aluminum anode.

spot size. The line  $1/d$  is plotted along with the data points in Fig. 4.6.

The range of spot sizes examined is limited on the large end by the largest mark size observed, which is likely related to the length of the current pulse. The limit on the low end is due to the difficulty in positively identifying damage left behind by the arc: at sizes smaller than those in the figure, marks left behind by the polishing process and, more significantly, those caused by oxidation and corrosion of the surface can appear very similar to arc damage. Investigation to smaller sizes requires a higher degree of anode surface polish than was possible in these experiments, on an anode made of a suitable metal (one that is non-corrosive in air and has appropriate thermal properties).

The slope of the points in Fig. 4.6 is artificially low, because large marks inevitably obliterate small marks. For this reason, the count in the range 1–10 mm is lower than it would be had not some of those marks been obliterated by those in the 10–100 mm range; the count is, for the same reason, too low in the 0.1–1 mm range, and so forth. While the distribution therefore has a slope close to  $-1$  on the logarithmic scale shown in the figure, it is likely that the distribution of mark sizes goes like  $1/d^\delta$ , where  $\delta \geq 1$ .

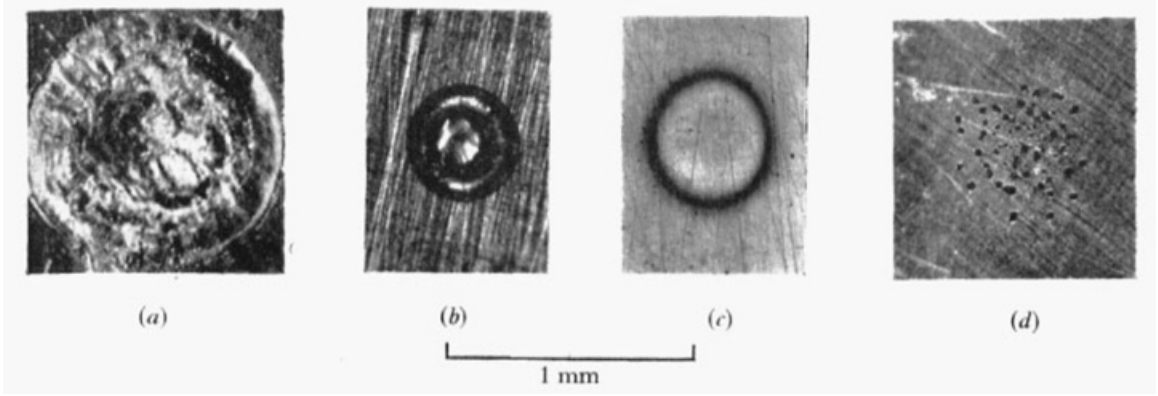


Figure 4.7: After Somerville [49]. Typical anode marks. (a) Tin anode, arc duration  $1200\ \mu\text{s}$ , arc current 34 amp. (b) Aluminium,  $200\ \mu\text{s}$ , 50 amp. (c) Copper,  $200\ \mu\text{s}$ , 50 amp. (d) Tin,  $1\ \mu\text{s}$ , 100 amp.

## 4.6 Time Evolution of Anode Damage

### 4.6.1 Background

While we cannot make any time-resolved observations of the formation and dynamics of anode spots in the MPDT, we would like to make a few inferences about the possible behavior of the spot during its lifetime to round out our knowledge of anode damage. In this section, we will compare the MPDT anode damage to that of a series of experiments in the literature whose observations of damage bear an interesting resemblance to our own.

The literature to which we refer describes work done at the University of New England, Australia, by Somerville et. al. [49,50]. These authors noted that the anode marks left behind on anodes of various metals, due to arcs of varying duration, had structures similar to one another, and that could be explained by considering the arc to be a rapidly expanding cylindrical channel of current [51].

Figure 4.7 is taken from photographs of the Somerville experiments, showing the anode marks left behind by transient arcs of the intensity and duration listed in the caption. The differences between the marks, caused by the differing anode materials and arc energies (i.e., current and duration), are clear: those marks on tin

and aluminum, both metals with relatively low melting points, are circles of metal that had melted under the action of the arc. The mark on copper, under conditions otherwise identical to those for the shown aluminum anode mark, is not melted, but rather is a discolored ring. Finally, the mark left behind on a tin anode for a very short duration arc ( $\sim 1 \mu\text{s}$ ) also does not appear melted, but rather is a circularly-distributed collection of points.

The appearance of these anode marks sheds light on the pattern of current conduction within the arc channel during its short lifetime. The marks left behind after the  $1 \mu\text{s}$  arc on tin (d) have clearly been obscured by melting after the  $1200 \mu\text{s}$  duration of the arc which left behind the melted crater in (a). The origin of the multiple marks on the anode in (d) is made clear by photographs of the arc during the discharge. Figure 4.8 shows two photographs of an arc on a tin anode, one for a  $5 \mu\text{s}$  discharge (left), and the other for a  $40 \mu\text{s}$  discharge (right) at 50 and 80 A, respectively. In the short-duration arc, the anode attachment clearly occurs in multiple points clustered together in an area of roughly 0.5 mm diameter, while in the longer-duration arc, the conduction occurs through both a central channel and a surrounding ring.

The time evolution of these arcs has been explored by these same authors using a palladium anode [52]. They used identical polished palladium anodes to pass 36 A arcs of varying duration, from 2 to  $50 \mu\text{s}$ . In this way, they observed the mark left behind on the anode as a function of time during the arc. Figure 4.9 is a reproduction of their findings. For a short duration arc, the current clearly passes through a number of small points clustered together; as the duration of the arc increases, the marks indicate that the current increasingly passes through the points on the outer periphery, eventually (by about  $8 \mu\text{s}$  in this figure) passing through a ring on the outer boundary, as the photographs in Fig. 4.8 attests. For longer duration arcs, the mark melts inward, eventually obliterating the original small-scale structure present

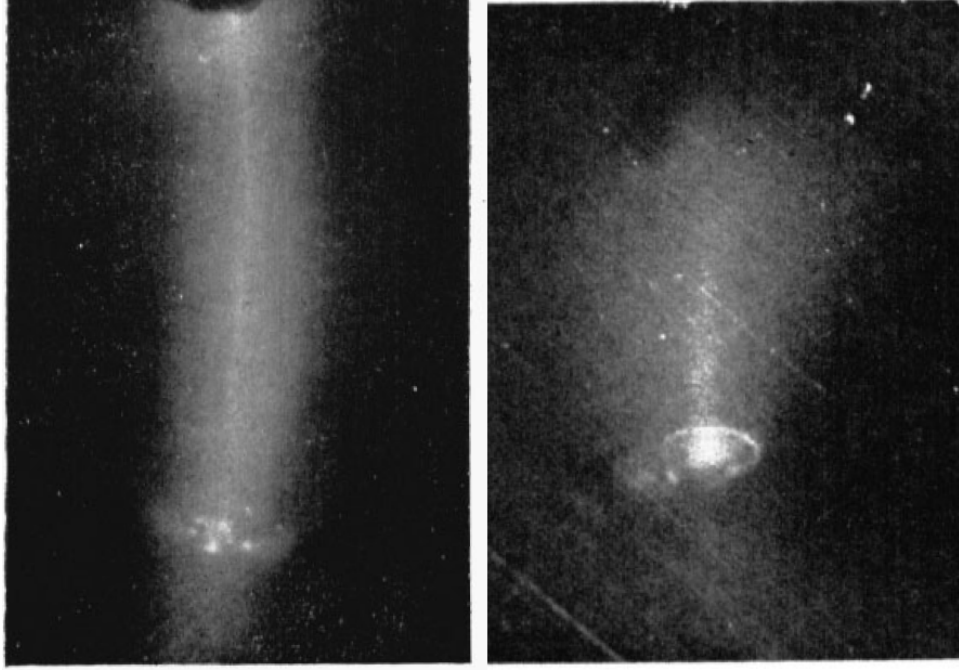


Figure 4.8: After Somerville et. al. [49] Photographs of fast arcs on a tin anode (anode at bottom of picture). (Left) 50 A arc of 5  $\mu$ s duration. (Right) 80 A arc of 40  $\mu$ s duration [50]. The diameter of the luminous area on the anode is in each case 0.5 mm.

in that mark.

The question remains why the marks should be circular, and especially why in the early stages the current should be conducted in a ring on the anode. Somerville and Williams [51] answered these questions by considering the dynamics of the current channel to be equivalent to those of an expanding cylindrical shock front. They follow the model of Drabkhina [53]—or, equivalently, of Lin [54], whose results were the same as those of Drabkhina—who derived the radial expansion velocity and density profile of a cylindrical shock wave produced by a fast release of energy along a line, in analogy to G. I. Taylor’s [55] seminal work on spherical shock waves. In this case, the arc initiation provides the energy release, which may have some profile in time, and the radius of the expanding shock channel is given by

$$R(t) = \left( \frac{\alpha}{\rho_o} \right)^{1/4} \left[ \int_0^t \sqrt{E(t)} dt \right]^{1/2}, \quad (4.1)$$

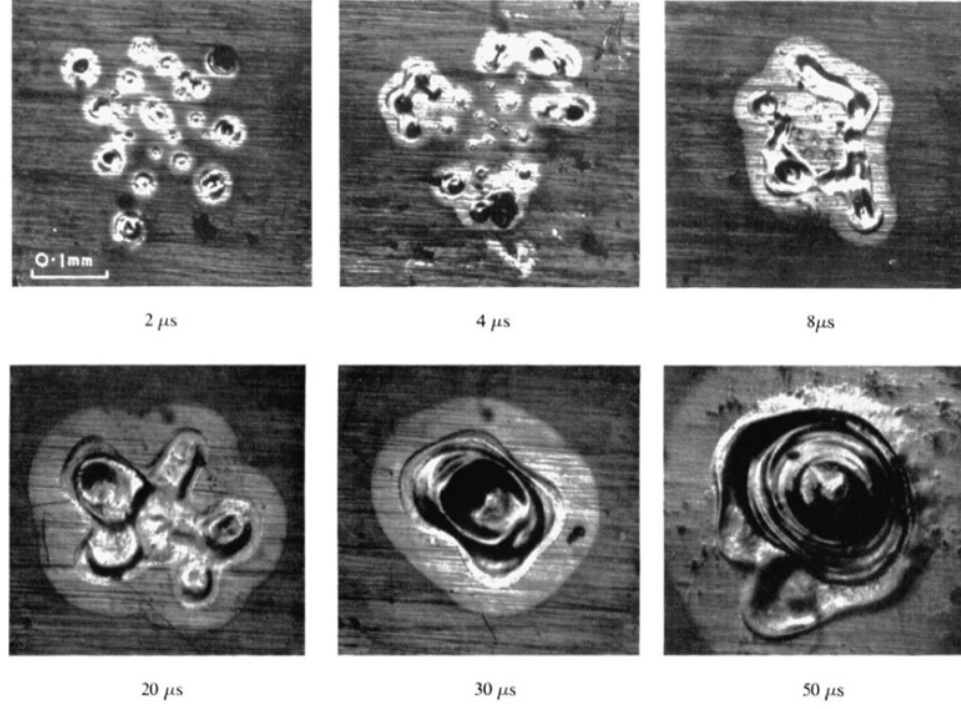


Figure 4.9: After Somerville and Grainger [52]. Marks left behind by a 36 A arc on a palladium anode for arcs of increasing duration, as noted.

where the factor in front of the integral is a constant depending on the density and species of the medium, and  $E(t)$  is the energy per unit length released along the line. A schematic of the expansion process is shown in Fig. 4.10, along with the calculated normalized density profile within the expanding channel from Drabkhina's original paper.

Somerville and Williams found that the current-carrying channel of their arc followed the calculated shock front position for about 0.2  $\mu$ s, after which they found that the front detaches from and expands more quickly than the channel. However, during the expansion phase, the density in the core of the channel is exceedingly low, while that at the periphery is much larger than the ambient: that is, the plasma conductivity at the outer edge of the channel is much greater than in the core, and it is through this ring at the outer edge that the current flows. The origin of the channels as shocks expanding from a central axis explains their cylindrical nature;

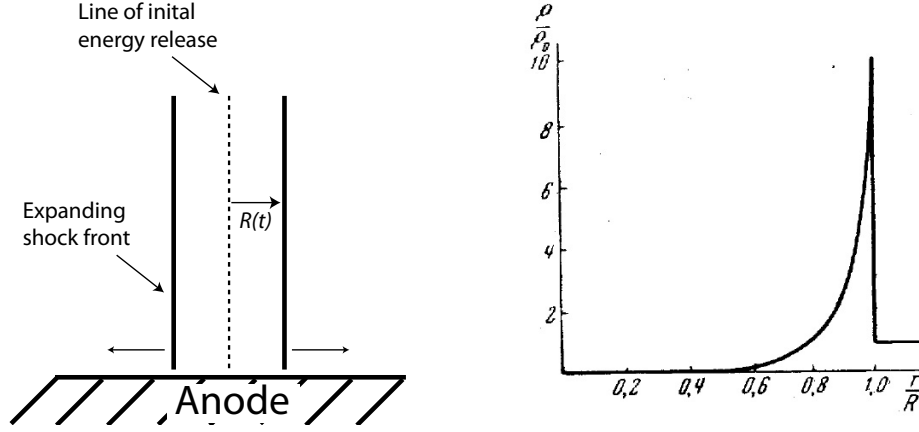


Figure 4.10: (Left) Illustration of the expanding cylindrical channel. (Right) The density profile within the expanding cylindrical channel, after Drabkhina [53].

the density profile as a result of the shock explains the ring conduction pattern.

#### 4.6.2 Spot Evolution on the MPDT Anode

While the experimental conditions between the study of Somerville et. al. are different from those in the FSBT, the differences are not so great as to make the Somerville conclusions of no use to us. The Somerville experiments were conducted in air, at pressures between 200 Torr and atmosphere, with arcs struck at currents on the order of 100 A and voltages of a few kV. The FSBT is run with argon at a pressure of  $\sim 1$  mTorr, at a current of tens of kA, and at voltages of a few hundred V. Nevertheless, we will see in this section that the FSBT anode damage strikingly resembles that of the Somerville experiments. This may be attributed to the unimportance of the differences between experimental conditions: the anode damage depends upon the power input to the anode metal, which is governed by the energy in the arc—not the specific values of current and voltage. The difference in medium species is also largely immaterial, since the anode power input is accomplished almost exclusively by electrons.

Because the Somerville group could control the arc time and energy, they could systematically study the formation of the anode damage as a function of these

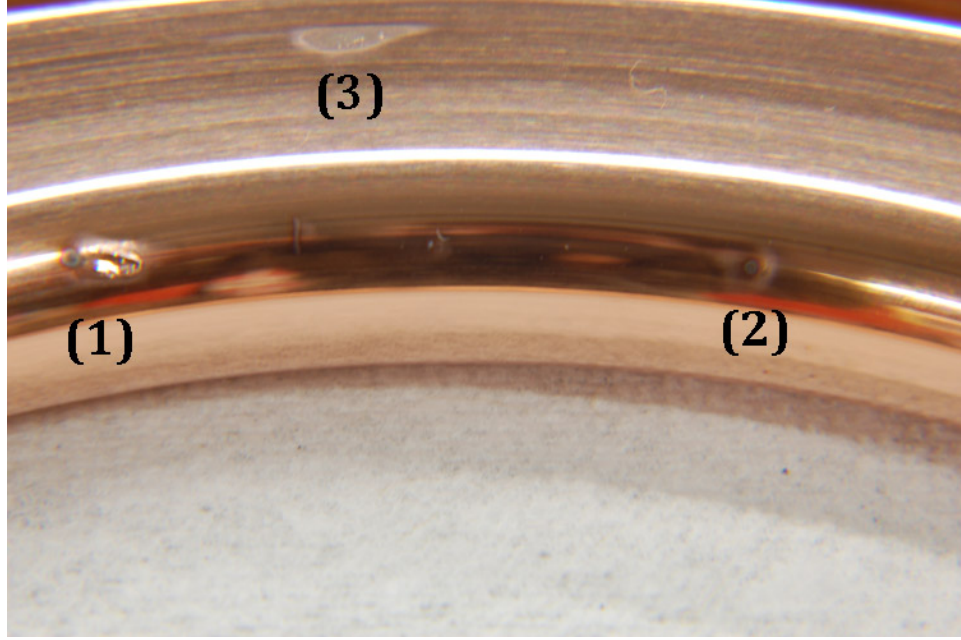


Figure 4.11: Anode spot damage on the lip of a copper anode.

parameters. Experiments in the MPDT do not share this luxury: anode spots form spontaneously on the anode surface, with a random energy and duration that the operator cannot control. Even for currents at which anode spotting is extensive, the FSBT discharge remains mostly symmetric (Fig. 4.3 is an example), rather than collapsing entirely into one channel between the two electrodes; this makes it impossible to know what fraction of the discharge current passes into the anode in a diffuse manner, and what fraction passes through the spots.

We will therefore, in this section, use our knowledge of the fortuitous similarity between the Somerville anode damage and our own to infer the behavior of anode spots in the FSBT. We use as an example a copper anode (copper, with its higher melting point and higher thermal conductivity than aluminum, less easily loses its markings to melting) which has endured a single firing at  $J^2/\dot{m} = 65 \text{ kA}^2\text{-s/g}$ . A sampling of the damage left behind appears in Figures 4.11 (a photograph of the anode lip) and 4.12 (several microscope images of anode marks in various degrees of formation).

The microscope images in Fig. 4.12 show several damage marks found on the anode surface. From top left to bottom right, these are a darkened circle of  $20\ \mu$  diameter; a dark circle surrounded by a darkened ring, total 0.5 mm diameter; a thick darkened ring containing a multiplicity of melted points, 1 mm total diameter; and an oblong melted ring, 2 mm short dimension. The first of the three is not visible to the naked eye; the next two appear like form (2) of Fig. 4.11 without magnification. The third, with its gross melting, appears to the naked eye like form (1) of Fig. 4.11. These damaged points, with the exception of the last, are circular. (The photographic equipment available for the microscope pictures had a limited depth of focus, leaving portions of some of the pictures blurred.)

Because spots form with a variety of energies and lifetimes in the FSBT, we can take the different damage marks just discussed to be indicative of anode spots that were extinguished at different times in their development, and in this way try to track the evolution of an anode spot. In essence, this creates an implied relative time index on the anode spots pictured in Fig. 4.12, made by comparison with the explicit time index in the Somerville experiments. The picture that emerges is as follows. The  $20\ \mu$  mark in Fig. 4.12 was created by a spot in its initial stages of formation, when the channel through which energy is deposited to the anode is small. As in the case of the marks of Somerville, a spot with a longer lifetime expands quickly, so that the current it carries soon leaves the central part of the channel, and begins to flow through the outer channel boundary. This leaves behind a “bulls-eye” mark, as in the second photograph in Fig. 4.12. After a rapid initial phase of expansion, the expansion slows and the current anchors in the ring-pattern conduction established earlier in its life; the energy input to the anode surface below the spot becomes larger, since the spot is expanding more slowly. The anode metal begins to melt as a result, leaving behind a mark as in the third photograph of Fig. 4.12. Finally, the longer the lifetime of the spot, the greater the melting, so that the ring in the fourth photograph



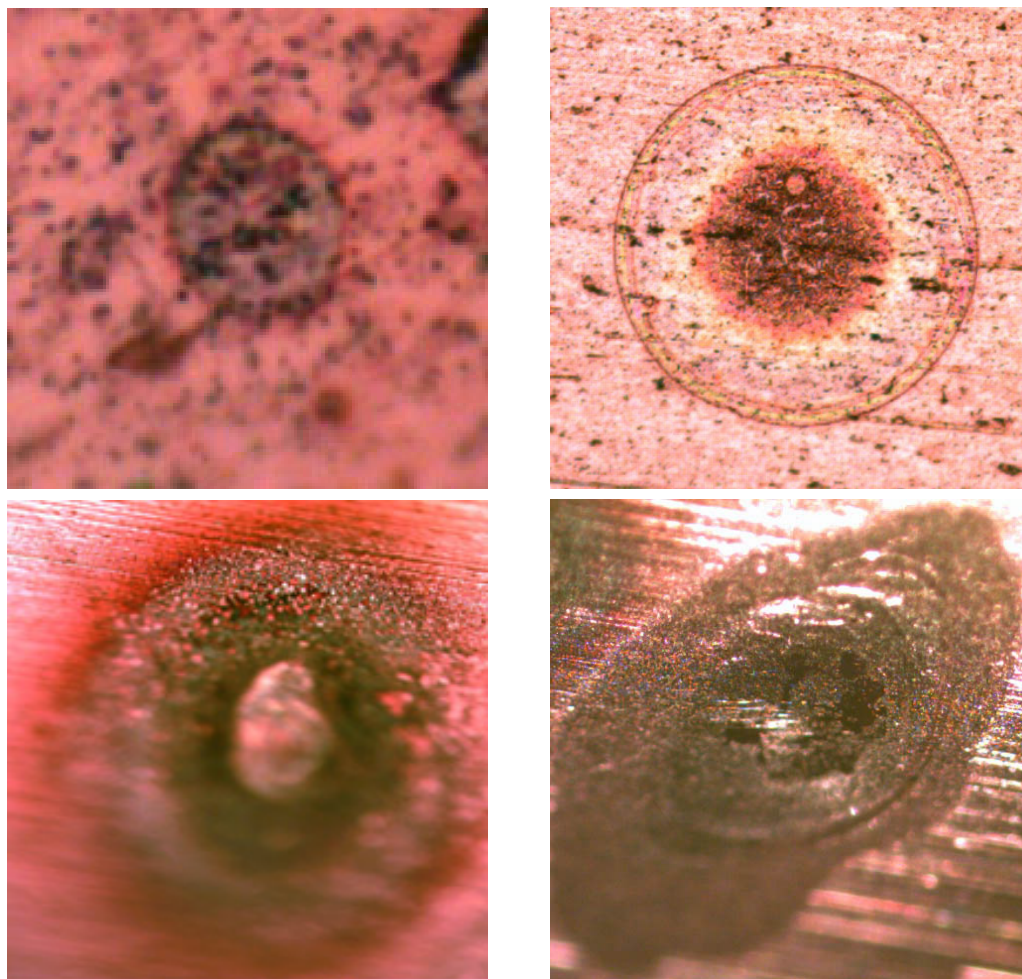


Figure 4.12: The progression of an MPDT anode spot. From top left to bottom right: a darkened circle of  $20\ \mu$  diameter; a dark circle surrounded by a darkened ring, total 0.5 mm diameter; a thick darkened ring containing a multiplicity of melted points, 1 mm total diameter; and an oblong melted ring, 2 mm short dimension.

of Fig. 4.12 has been completely melted. Even in this last photograph, however, the spot lifetime was not long enough for the metal to melt back into the center, which left the metal in the middle of the ring untouched. A longer-lived spot would leave behind a mark such as (1) of Fig. 4.11, in which the entirety of the region is melted, leaving behind no indication of the original ring structure.

In none of Somerville’s literature did the marks have an oblong shape such as seen in Figs. 4.11 and 4.12. The Somerville experiments, however, did not have a magnetic field imposed across the current channel. The FSBT, by contrast, has a self-induced magnetic field parallel to the anode surface; any current-carrying channel is subjected to the  $\mathbf{j} \times \mathbf{B}$  Lorentz body force, which will force the plasma in the radial direction along the anode surface. This force will tend to elongate the damage mark, which is seen in every picture of sufficiently-developed anode damage in this chapter.

In this account, the difference between marks (1) and (2) in Fig. 4.11 is the lifetimes of the spots that created them. The shallow, wide melting of mark (3) of Fig. 4.11 appears only along boundaries, in this case the inside boundary of the MPDT chamber. This appearance is a result of the constrained growth of a spot that forms right on a boundary: unable to grow symmetrically because of the quartz wall, it spreads out rapidly along the wall, and the mark it leaves is therefore more broad and shallow than it otherwise would be.

To summarize: an understanding of why we see anode damage of different forms is the end product of this comparison between MPDT spot damage and that seen in the Somerville experiments. The different damage forms—symmetric circular or oblong streak, melted or discolored—are marks left behind by anode spots of different lifetimes and total energies. This variety of lifetime and energy among the anode spots is also what gives rise to the distribution of anode mark sizes discussed in the last section.

## 4.7 Damage to Anodes of Extreme Materials

We now turn to the damage left behind on lead and graphite anodes, whose voltage hash properties we have already discussed. We have mentioned that copper sustains less severe damage than does aluminum, due to its greater thermal conductivity and higher melting temperature. Lead and graphite anodes illustrate this pattern in the extreme: lead displays significant damage even for the lowest  $J^2/\dot{m}$  values, while graphite displays no significant damage at even the highest  $J^2/\dot{m}$  values—both independent of the voltage hash behavior.

Table 4.1 lists together the relevant electrical and thermal properties of copper, aluminum, lead, and graphite. Among these four materials, the resistivity, density, specific heat and thermal conductivity all vary between one and three orders of magnitude. The ratio  $(\alpha/k)$  is an indicator of the extent to which the temperature of a material rises given a distribution of boundary heat fluxes and volumetric heat sources; the ratio of this quantity for two materials is the same as the ratio of the temperatures, when all lengths are normalized to the thermal diffusion distance  $\sqrt{\alpha t}$ . The  $(\alpha/k)$  row has been normalized to that of copper; aluminum, lead, and graphite all reach temperatures significantly larger than copper for an identical heat flux. At the same time, aluminum and lead have significantly smaller melting temperatures, and will melt at arc heat fluxes significantly smaller than will copper. On the other hand, graphite does not melt, but only sublimates.

As regards the interaction of the anode with the discharge, the most relevant measure of the difference between the materials is the erosion rate, measured as a function of temperature. The erosion rate into vacuum of any material is a function of the temperature, derivable from kinetic theory, and is given in SI units by

$$\Gamma = p_{sat} \sqrt{\frac{M}{2\pi kT}}, \quad (4.2)$$

Table 4.1: Summary of the properties of some anode materials.

Parameter	Copper	Aluminum	Lead	Graphite
$\rho$ [ $\mu\Omega \cdot \text{m}$ ]	.017	.027	0.21	14
$\rho$ [ $\text{kg}/\text{m}^3$ ]	8920	2700	11340	1938
$c_p$ [ $\text{J}/\text{kg}\cdot\text{K}$ ]	384	904	127	710
$k$ [ $\text{W}/\text{m}\cdot\text{K}$ ]	400	235	35	—
$\alpha$ [ $\text{mm}^2/\text{s}$ ]	117	96	24	—
$T_m$ [K]	1358	933	601	—
$\alpha/k$ [ $(\alpha/k)_{Cu}$ ]	1	1.4	2.4	2.5

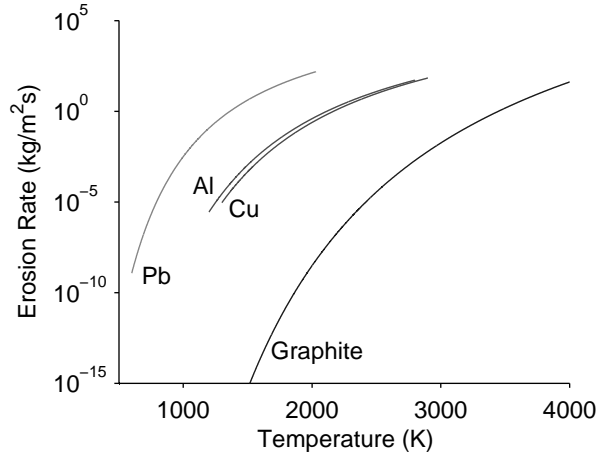


Figure 4.13: The erosion rate of four anode materials as a function of temperature.

where  $p_{sat}$  is the equilibrium vapor pressure. Empirical curves are available for  $p_{sat}$  for all of the above materials [23, 24]; using these (with the three metals in the liquid phase, and graphite solid), we calculate the erosion rate  $\Gamma$  for each as plotted in Fig. 4.13.

Because copper and aluminum have very similar erosion rates over the range of temperatures that the anode experiences in the FSBT, it is unsurprising that they exhibit similar damage characteristics and voltage hash. On the other hand, lead erodes significantly faster than either, at lower temperatures, and therefore provides a greater supply of material to the discharge. Graphite, by contrast, erodes orders of magnitude more slowly than the other materials for similar temperatures. Graphite

has the additional advantage that, because it does not melt, it avoids releasing molten macroscopic particles into the discharge, as the other materials do, making its comparative erosion rate smaller than even the calculation of Fig. 4.13 suggests. While the higher temperature of graphite (compared with that of copper) due to the same heat flux complicates the comparison between these two materials, the comparison between lead and graphite does not share this ambiguity, as they have a similar  $\alpha/k$  ratio.

Although graphite is significantly more resistive than any of the other materials, this does not pose a problem for either the arc voltage or the anode heat loads. Estimates indicate that, while the voltage drop across the anode and joule heating in the anode volume are larger than those in the copper anode by a factor of  $10^3$ , their values are still insignificant: less than 5 V are dropped across the graphite anode, and the temperature rise due to Joule heating by the highest-current pulse used in this study is below 1 K.

### 4.7.1 Damage to a Lead Anode

Experiments with the lead anode resulted in anode damage at all operating conditions, including at values of  $J^2/\dot{m}$  far below those at which damage begins to appear on copper or aluminum anodes. Figure 4.14 shows a time-integrated photograph of the first MPDT firing with the lead anode, and a photograph taken immediately afterward. Although  $J^2/\dot{m} = 12 \text{ kA}^2\text{-s/g}$  in this case, the anode suffered gross melting, as the photographs show.

The damage sustained by the lead anode, however, is not accompanied by voltage hash as we often observe in the case of aluminum or copper anodes. Figure 4.15 shows the voltage signal associated with the firing pictured in Fig. 4.14; it shows no appreciable hash. (The small fluctuations that are present are due to the desorption of gases from the new anode and the cathode, and disappear for more resilient anodes

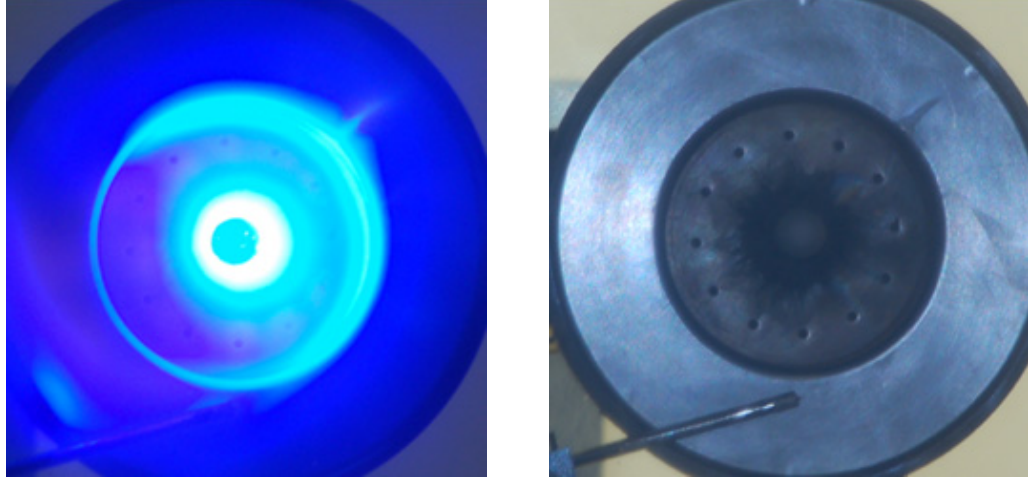


Figure 4.14: Lead anode during firing (left) and after (right) at  $J^2/\dot{m} = 12 \text{ kA}^2\text{-s/g}$ , well below onset.

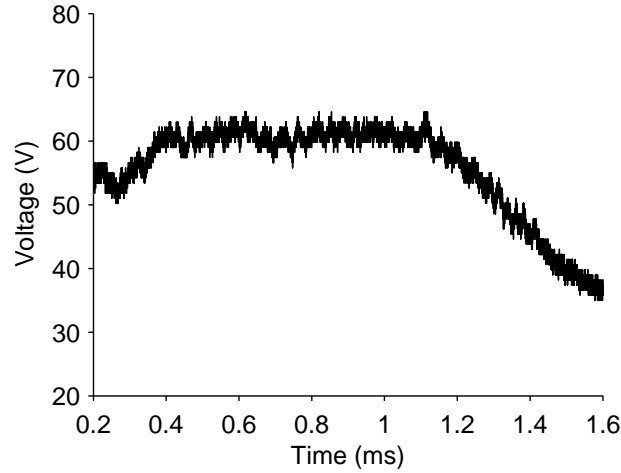


Figure 4.15: Voltage signal corresponding to the firing shown in Fig. 4.14.

after a number of low-current firings. Lead's susceptibility to damage, however, did not allow for low-current cleaning.)

This pattern is repeated for all operating conditions using the lead anode. Some measure of damage is sustained by the anode during every firing, regardless of its  $J^2/\dot{m}$  level; the hash exhibited in the voltage is more indicative of the  $J^2/\dot{m}$  level than it is of the visible anode damage, and its properties were discussed in Chapter 3.

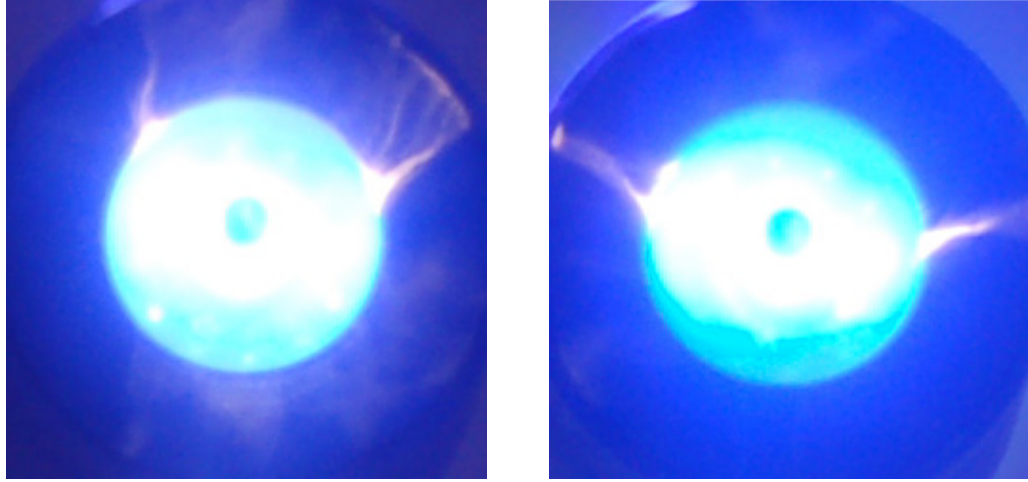


Figure 4.16: Graphite anode during two firings well above onset, with visible current contraction.

#### 4.7.2 Damage to a Graphite Anode

The graphite anode sustained negligible damage at all operating conditions, including at  $J^2/\dot{m}$  levels much larger than those used with anodes of any other material. Figure 4.16 shows two examples of the MPDT arc firing at high  $J^2/\dot{m}$  with a graphite anode. The current attachment at the anode is not diffuse, but “after” pictures similar to that given for lead in Fig. 4.14 are unrevealing. Instead, Fig. 4.17 shows a photograph of the graphite anode before and after over 150 shots at  $J^2/\dot{m}$  above onset with significant voltage hash. While discoloration is clearly present over the anode surface where the current has attached in spots, the surface shows no sign of significant damage the way lead, and to lesser extent aluminum and copper, do. Because photographs of the thruster firing reveal the presence of anode spots, and the voltage hash for graphite is similar to that of the other materials, we conclude that the significantly reduced damage on the graphite anode is the result primarily of the refractory nature of graphite, and not of alterations to onset phenomena.

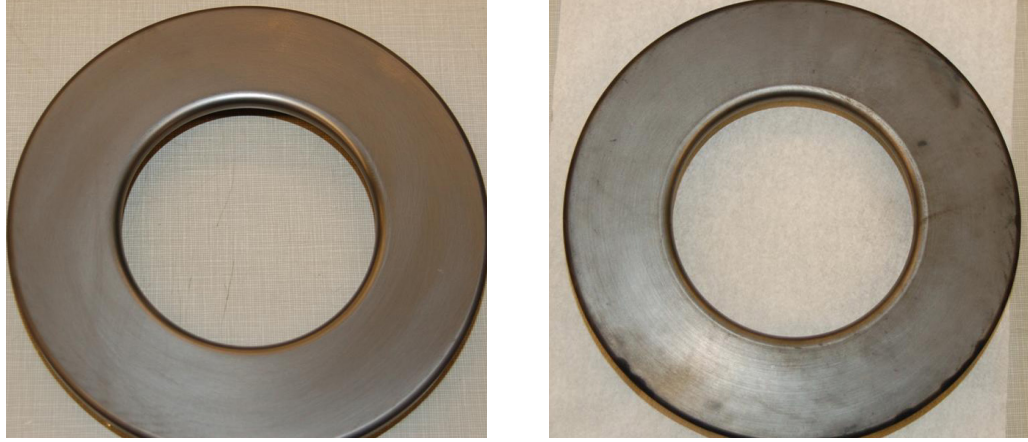


Figure 4.17: Graphite anode clean (left) and after over 150 firings at above-onset conditions (right).

## 4.8 Summary of Observations on Anode Damage

Our examination of the anode damage suffered by a MPDT has illuminated many important features of the damage character and has allowed us to make a number of inferences about the anode spots that cause the damage.

- *Anode damage concentrates in areas of high current density.* In the FSBT, these areas are the lip and the outer boundary, presuming that the anode is free of surface contamination.
- *For a given anode material, the character of the damage is the same across  $J^2/\dot{m}$  values, but the severity of the damage increases with  $J^2/\dot{m}$ .* The spot damage occurs in isolated points and streaks: this is not a  $J^2/\dot{m}$ -dependent phenomenon, but the severity with which it occurs is. This is true regardless of the amplitude and statistics of the voltage hash.
- *Spot damage sizes self-organize into a power-law distribution, such that the probability of spot damage of size  $d \sim 1/d^\delta$ , where  $\delta \geq 1$ .* This distribution of sizes is indicative of a distribution of spot lifetimes and energies during the arc. There is no characteristic spot size scale.



- *The severity of anode damage is more characteristic of the anode material than of  $J^2/\dot{m}$  level or voltage hash properties.* The most refractory materials are the least severely damaged.

The picture of anode spots that arises from these insights is the following. The current conduction to the anode, which at low  $J^2/\dot{m}$  is primarily diffuse, forms to some extent into spots at all  $J^2/\dot{m}$  levels. These spots carry little energy at low  $J^2/\dot{m}$ , so they have no effect on the anode, except when the anode material is sufficiently susceptible to damage, as lead is. As  $J^2/\dot{m}$  grows, the energy carried by anode spots grows, increasingly leaving behind damage on ever more refractory anodes. Thus aluminum sustains more severe damage than copper, which sustains more severe damage than graphite. These spots form in a stochastic manner, with no characteristic size, energy carried, or lifetime, but with a cascading distribution that makes damage marks of small size  $d$  more likely than those with larger size  $d$  according to the power-law  $1/d^\delta$ ,  $\delta \geq 1$ .

While on the surface our observation that damage severity is a function of anode thermal properties is trivial, it challenges the prevailing view of the function of anode spots. While the spots may release some anode material into the discharge, depending upon the anode's thermal properties, it seems that less refractory materials incur greater damage than is strictly necessary to satisfy spot current demands. Voltage hash and spotting occur in much the same fashion on anodes of widely different thermal properties, but the damage left behind on the various anodes is far from uniform. From this we see that the anode is primarily a passive player in the discharge, responding to the action of anode spots according to its thermal characteristics.

# Chapter 5

## The Relationship of Voltage Hash to Anode Erosion

### 5.1 Introduction

The evidence from Chapters 3 and 4 is that both the voltage hash and the anode damage are manifestations of random processes, with the result that, within our range of measurements, the voltage hash has no characteristic time scale and the spot damage has no characteristic size scale. Diamant [14] has suggested that the role of the anode spots is to provide additional particle density to solve the starvation crisis that occurs at high  $J^2/\dot{m}$ . Were this the case, it is reasonable to assume that the same degree of erosion would be apparent on anodes of all materials for similar operating conditions. Since, however, we have observed that the severity of the anode damage is related more to the anode material properties, and less to  $J^2/\dot{m}$  (and hence anode starvation), the more natural conclusion is that the anode spots act only with respect to the  $J^2/\dot{m}$  level, and the anode responds according to its thermal properties, releasing more or less mass according to its temperature-dependent erosion rate.

Our purpose in this work is to understand the phenomenology of onset. It is

interesting to note, therefore, that one of the fundamentals of onset—the approximate correspondence of voltage hash and anode damage, which has been noted many times in the literature—is a result of a fortuitous coincidence between the value of  $J^2/\dot{m}$  at which the voltage begins to show significant hash and the  $J^2/\dot{m}$  at which the anode damage begins to appear. We have shown that these two  $J^2/\dot{m}$  values need not be the same, as the contrast between graphite and lead anodes shows. Nevertheless, we have stated, in Chapter 3, that the nonstationarity of hash statistics is due to unsteady anode erosion, and now we wish to substantiate this claim.

With that in mind, the purpose of this chapter is to clarify the relationship between anode erosion and voltage hash in the case where the two do occur at similar  $J^2/\dot{m}$  values—specifically, for a copper anode. The question we wish to answer is, how does anode erosion influence the voltage hash?

As we pointed out in Chapter 1, erosion has been linked with hash in the literature from the earliest days of onset investigation. Erosion of the anode increases dramatically when the  $(J^2/\dot{m})^*$  is exceeded (where, as usual,  $(J^2/\dot{m})^*$  is defined by the voltage hash magnitude, and an anode of copper or steel, which display the fortuitous coincidence between hash and erosion, is used) [8, 13]. These observations are drawn from time-integrated spectral studies, which observe the light intensity at relevant wavelengths integrated over the length of a quasi-steady thruster pulse. We are not aware of any time-resolved spectral studies of this kind. The closest related study is that of Kuriki and Iida [11], whose luminosity measurements were not wavelength-resolved, and so offer no information about which species is responsible for the luminosity fluctuations observed.

Our results in this chapter provide observations of the time-dependent luminosity of both the argon propellant and the copper anode material in the thruster plume. The temporal relationship between these luminosity measurements and the voltage hash provide us the answer to the question posed above: how does anode erosion

influence the voltage hash?

## 5.2 Optical Diagnostics

The two diagnostics that we will use to answer the question posed above are time-resolved spectroscopy and high-speed video. We will discuss the results of these diagnostics, described in Chapter 2, in that order.

### 5.2.1 Time-resolved spectral measurements

The time-resolved spectral measurement of the thruster plume luminosity, which uses a spectrometer and photomultiplier as described in Chapter 2, provides us with a time trace of light output by either the argon propellant or the eroded copper anode vapor that can be compared to the simultaneously measured voltage trace. Examples of these measurements are shown in Figs. 5.1, 5.2, and 5.3 [56].

The spectroscopy setup used in this investigation was not calibrated to measure absolute spectral intensities of the line radiation emitted by the plume, because it is the relative change in the luminosity as a single firing progresses that is of interest to us. For this reason, in each of Figs. 5.1, 5.2, and 5.3, the luminosity traces have arbitrary units and have been scaled by an arbitrary factor to conveniently appear on the voltage axes. However, we can also draw information about the time-integrated evolution of the spectral intensities with current and mass flow rate by forcing the unknown calibration factors to cancel, in the following way.

The light collected by the PMT is proportional to the density of atoms making the emitting transition within the field of view; the proportionality constant is related to the solid angle taken up by the PMT photocathode, the quantum efficiency of the same, the PMT gain, and the Einstein coefficient of the transition. As all of these quantities are constant with current and mass flow rate, the *ratio* of the luminosity

of the argon and copper ion lines changes only with a change in the ratio of their densities. To see how this behavior plays out in the FSBT, we take the average of the copper and argon luminosity over the quasi-steady portion of a firing, and take the ratio of these time averages. We then plot this ratio, normalized to unity at the lowest current at which data was taken, against current in Fig. 5.4 for three values of mass flow rate. This plot gives an indication that, as a time-integrated quantity, the copper vapor in the plume takes on a growing presence with higher currents or lower mass flow rates. Such a result has been observed before [57], but without making reference to the time behavior of each species during the discharge, as we will now do.

The time behavior of the MPDT luminosity is dramatically different depending on which species is being observed, argon or copper. In summary, the copper luminosity shows a clear temporal relationship to the behavior of the voltage, while the argon luminosity shows either no such relationship, or a relationship opposite that shown by the copper.

Figure 5.1 shows traces of argon and copper luminosity, and voltage hash, for  $J^2/\dot{m} = 57 \text{ kA}^2\text{-s/g}$ . The argon luminosity rises in concert with the current (not shown), remains relatively steady over the course of the quasi-steady portion of the firing, and then falls again in concert with the current. It responds very little to changes in the voltage hash. By contrast, the copper trace responds to a decrease in voltage hash by a sudden increase in amplitude, indicating that at the end of a period of voltage hash, a quantity of copper vapor makes a sudden appearance in the spectrometer's field of view. (Of course, the causality in this sequence of events may just as well go the other way.)

A somewhat different behavior prevails at higher  $J^2/\dot{m}$ , such as in Fig. 5.2 where  $J^2/\dot{m} = 80 \text{ kA}^2\text{-s/g}$ . Here, the voltage alternates between bursts of high-amplitude hash and relatively quiet intervals between. Both the copper and argon

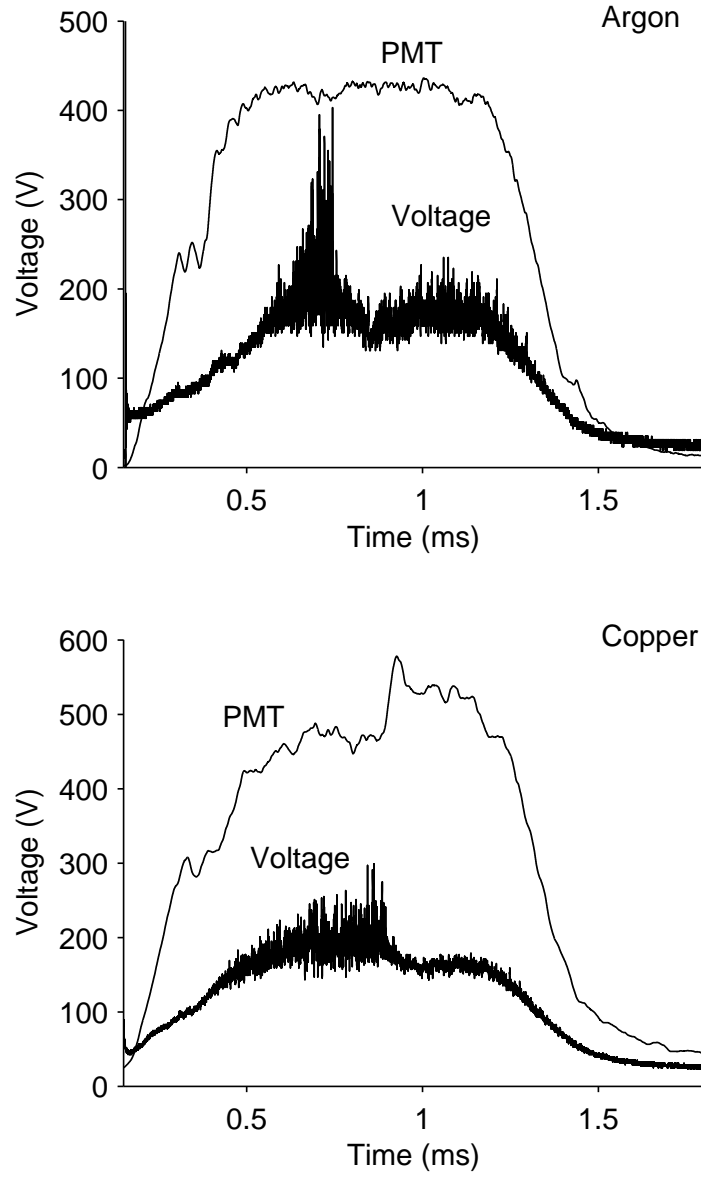


Figure 5.1: Examples of luminosity and voltage traces, for  $J^2/\dot{m} = 57 \text{ kA}^2\text{-s/g}$ . In each case, the luminosity trace has been scaled to fit the voltage axis. (Top) Argon luminosity and voltage traces. (Bottom) Copper luminosity and voltage traces.

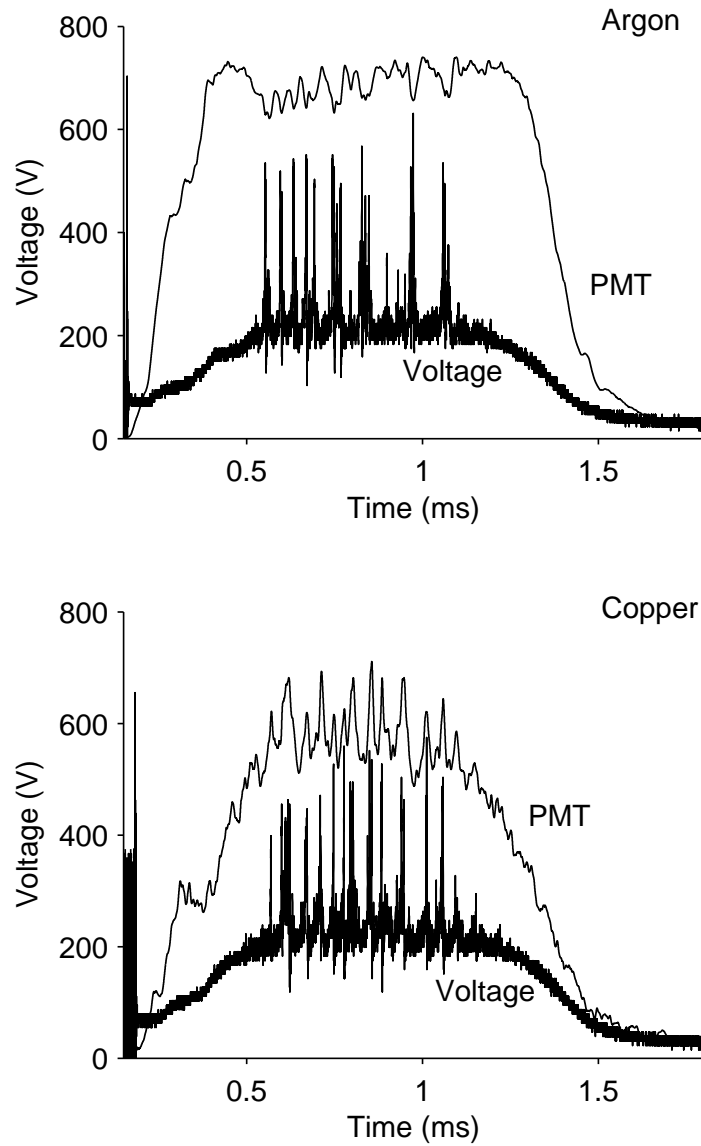


Figure 5.2: Examples of luminosity and voltage traces, for  $J^2/\dot{m} = 80 \text{ kA}^2\text{-s/g}$ . In each case, the luminosity trace has been scaled to fit the voltage axis. (Top) Argon luminosity and voltage traces. (Bottom) Copper luminosity and voltage traces.

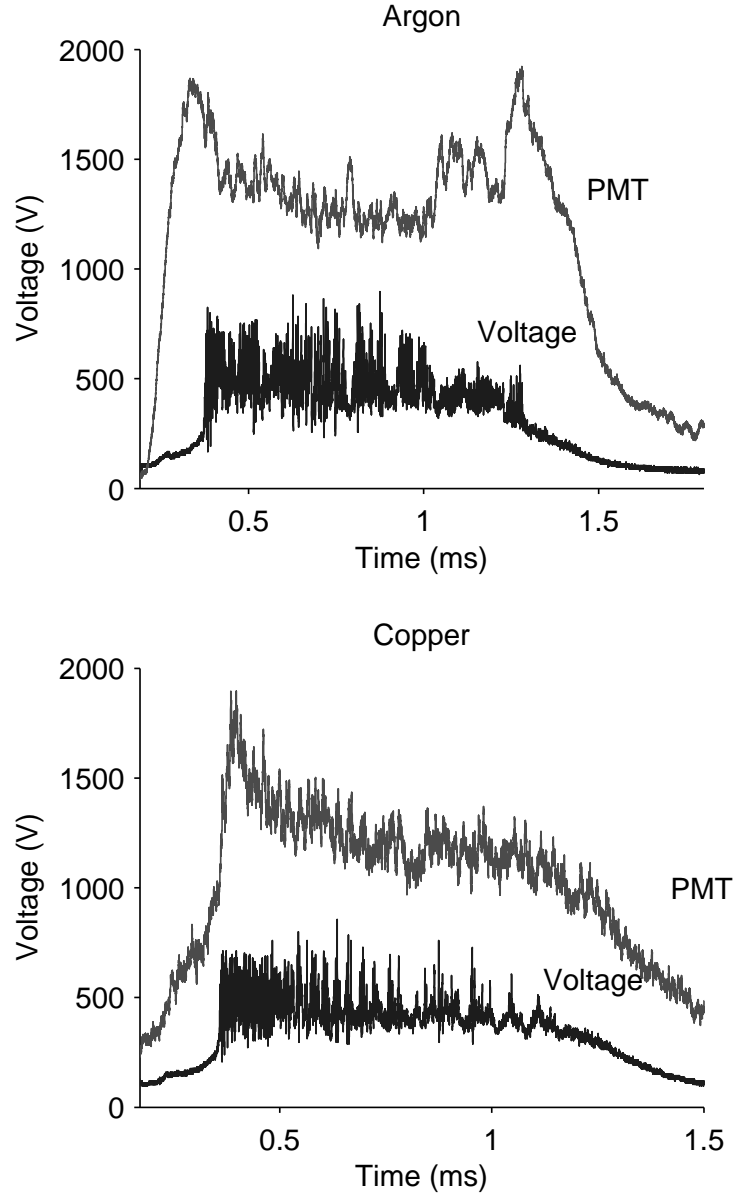


Figure 5.3: Examples of luminosity and voltage traces, for  $J^2/\dot{m} = 120 \text{ kA}^2\text{-s/g}$ . In each case, the luminosity trace has been scaled to fit the voltage axis. (Top) Argon luminosity and voltage traces. (Bottom) Copper luminosity and voltage traces.



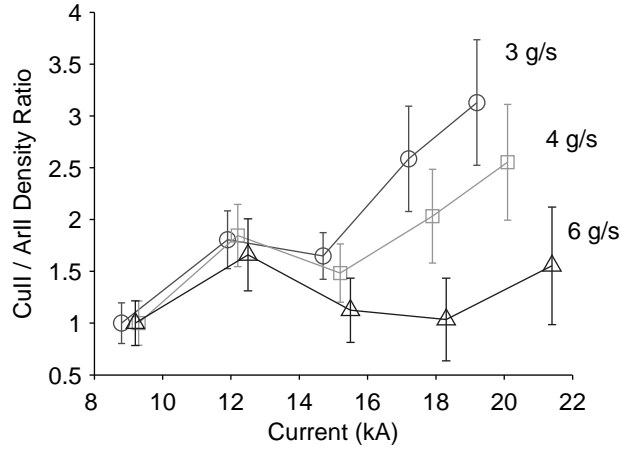


Figure 5.4: Normalized values of the copper/argon ion density ratios for three mass flow rates.

light output clearly vary with the hash bursts, but their variations are opposite one another: the argon intensity drops during a hash burst, and rises during the quiet periods; the copper intensity rises with the hash, and falls during the quiet times in between. The rising copper presence during hash has a clear interpretation: the process behind the hash leads to an increase in anode evaporation which is no longer effective when the hash ends. The fall in argon intensity during these same times may also be caused by the copper atoms, which are an energy sink to electrons as they are ionized, decreasing the electron temperature momentarily. Colder electrons allow the argon ion density to decrease by recombination.

The same trends are quite clear in Fig. 5.3, which shows the same traces for  $J^2/\dot{m} = 120 \text{ kA}^2\text{-s/g}$ . In this case, the high-amplitude hash completely dominates the voltage traces. As expected, the argon intensity decreases as the voltage hash begins, while the copper intensity makes a sudden increase.

## 5.2.2 High-Speed Video

The time-resolved spectroscopy using the photomultiplier arrangement of the last section provided excellent time resolution, but no spatial resolution. We can get

both using high-speed video, though state-of-the-art technology limits the possible time resolution to a fraction of that possible using a photomultiplier. We made our observations in this section with the high-speed video camera described in Chapter 2, operating at 50,000 frames per second—or  $20\ \mu\text{s}$  per frame—with the same exposure time. The image of the thruster on the CCD of the camera inhabits about 64 by 64 pixels, so that the spatial resolution is about  $9\ \text{mm}^2$  per pixel (each square pixel represents 3 mm each side).

The brightness of argon emission dominates the light output of the MPDT; all-light videos, therefore, do not provide any useful information about the behavior of anode erosion while the thruster operates above onset. An optical bandpass filter with a center wavelength at 630 nm and a bandwidth of 10 nm heavily attenuates the argon emission, while passing several lines emitted by CuII [28]. We used this filter at the input to the high-speed camera to observe the temporal evolution of the copper vapor. At our high frame rates, with filtering, the amount of light reaching the CCD is small. To more easily interpret the videos, we have inverted the frames, making light regions dark and vice versa; we have also enhanced the contrast, to make dimmer regions appear more bright. This makes it easier to identify areas with significant copper emission.

Videos at low values of  $J^2/\dot{m}$ , when little or no hash is present in the voltage trace, are uninteresting. In this section, we will discuss videos taken of the thruster at large values of  $J^2/\dot{m}$ .

A representative example of the video footage appears in Fig. 5.5. This shows, at top, a portion of a voltage trace for a thruster firing at  $J^2/\dot{m} = 60\ \text{kA}^2\text{-s/g}$ , labeled on the abscissa with numbers corresponding to the numbered frames of the high-speed video shown at the bottom of the figure. To orient the reader, we refer now to the frame labeled “1” in the figure. The dark ring surrounding a white circular area is a luminous ring surrounding the dark tip of the cathode; the area of dark pixels to the

left of this is a luminous area near the anode, which forms the right-hand boundary of this dark area.

The striking pattern revealed in this figure is clear: the emission of anode copper vapor in jets toward the cathode occurs during periods in which the voltage trace is relatively quiet, for example in frames 2–5. By contrast, when the voltage hash has a large magnitude, the presence of copper vapor is relatively muted—for example, in frames 6–7. In total, the periods of hash see relatively little vapor evolved from the anode, while the periods of quiet immediately following the hash see much emission of anode vapor. This corresponds exactly to the same observation using the photomultiplier, in Fig. 5.1.

As a side note, we should point out that the discharge does not collapse into a single column between cathode and anode during the quiescent periods, as a naive glance at the video frames might suggest. All-light videos and photographs of the discharge continue to reveal a symmetric discharge; it is the copper emission that provides the asymmetry in Fig. 5.5, and this emission is very dim in comparison to that of the entire discharge.

It is more difficult to make out distinct trends at higher  $J^2/\dot{m}$  values, corresponding to cases such as in Fig. 5.2. The fluctuations in the luminosity are visible in the video whose frames are shown in Fig. 5.6, though it is more difficult to make that out in the still frames. The copper light output is brighter when the voltage is high, and smaller when the voltage drops. The time resolution of the video frames is not, however, as good as in the case of Fig. 5.2, which, between the two, is the better indication of what is happening. The evidence from both these diagnostics indicates that at this  $J^2/\dot{m}$  level, erosion is not capable of suppressing the hash, either because it is too transitory, of insufficient magnitude given the higher  $J^2/\dot{m}$  level, or perhaps a combination of both.

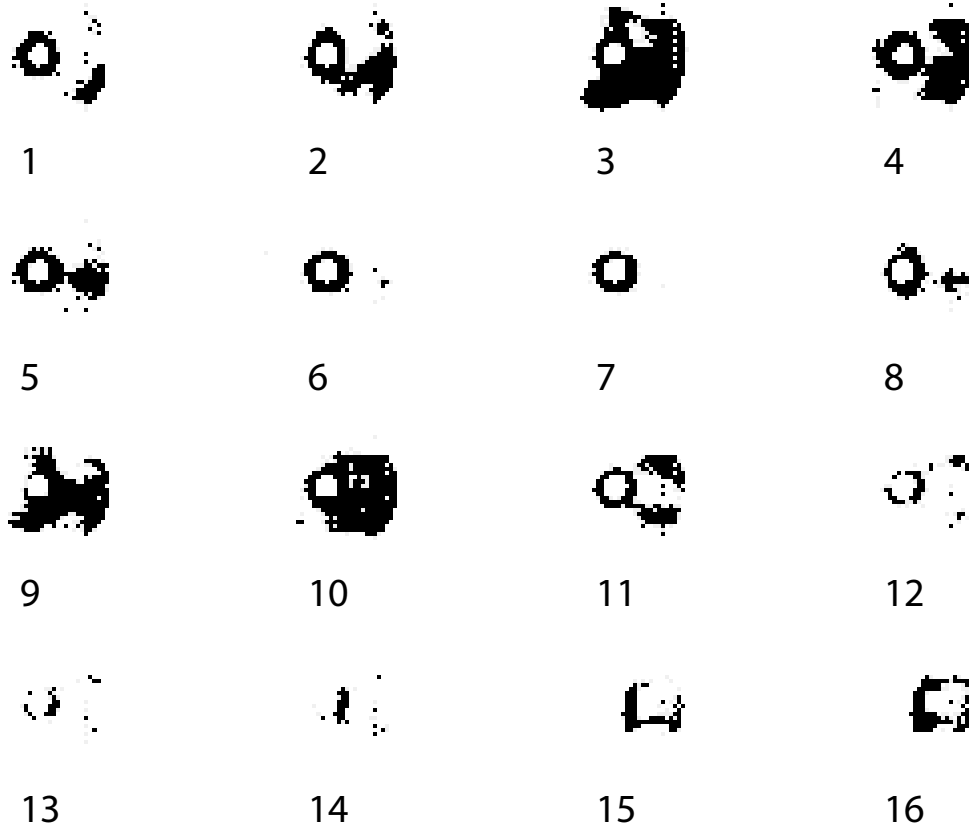
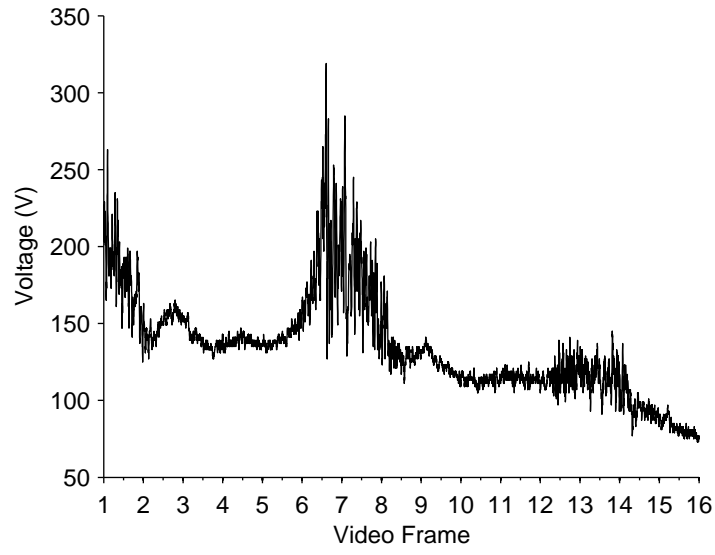


Figure 5.5: (Top) A portion of the FSBT voltage trace for a firing at  $J^2/\dot{m} = 60 \text{ kA}^2\text{-s/g}$ . (Bottom) Sixteen frames of a high-speed video of the thruster (see orienting details in the text), numbered according to where along the ordinate of the voltage trace the frame was taken.

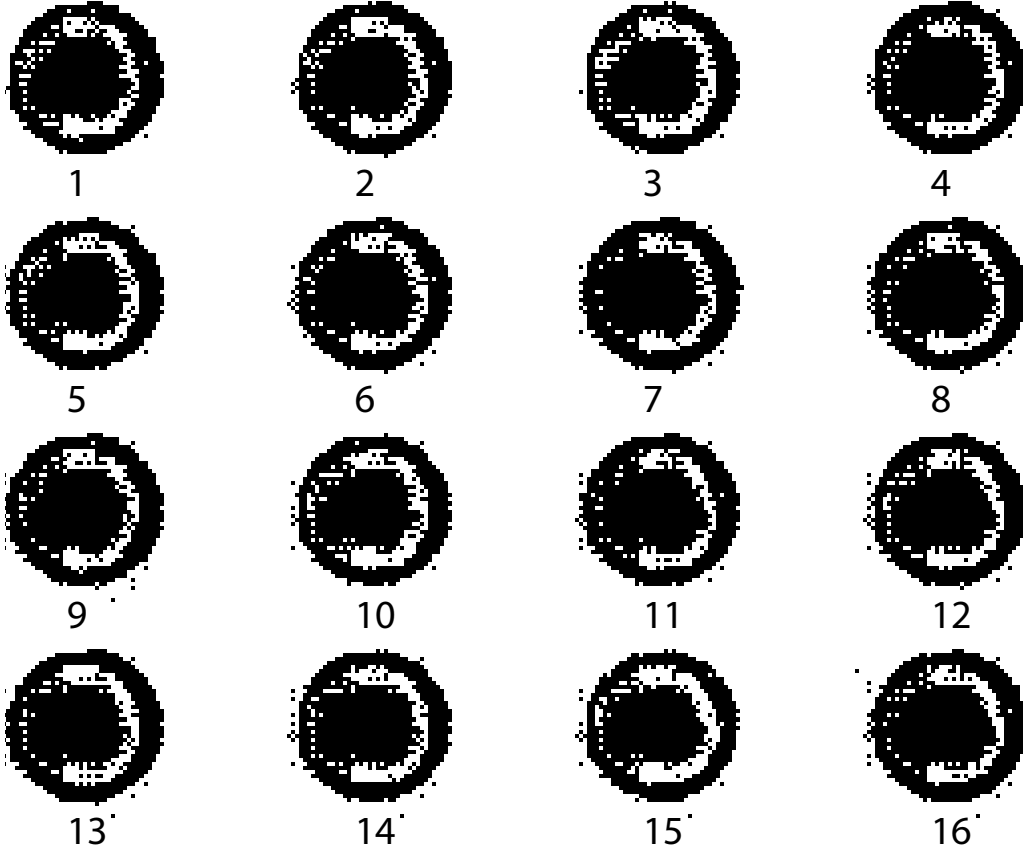
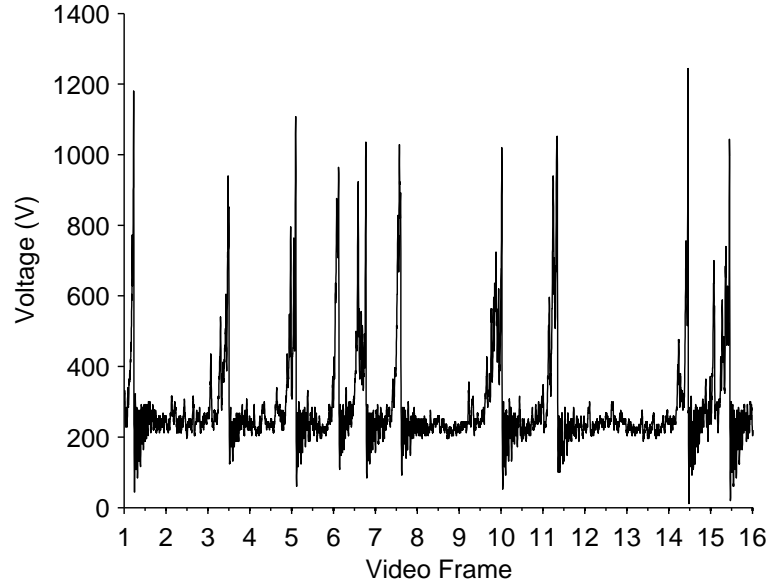


Figure 5.6: (Top) A portion of the FSBT voltage trace for a firing at  $J^2/\dot{m} = 80 \text{ kA}^2\text{-s/g}$ . (Bottom) Sixteen frames of a high-speed video of the thruster (see orienting details in the text), numbered according to where along the ordinate of the voltage trace the frame was taken.

### 5.3 Summary of Results

In this chapter we have reported a time-resolved investigation of the relationship between voltage hash and anode erosion. What we have observed agrees with previous time-integrated studies and sheds light on the influence of anode erosion on voltage hash properties. In summary, we have found the following.

- *Anode erosion accompanies voltage hash as  $J^2/\dot{m}$  increases, but greater anode erosion can suppress voltage hash.* Rudolph [8], among others, has observed this in a time-integrated sense, but we have shown it is true in a time-resolved sense as well. In the video of Fig. 5.5, we have the advantage of a single thruster firing with alternating periods of hash and quiescent voltage, and we observe that the voltage hash nearly disappears when copper vapor eroded from the anode bridges the gap between the anode and cathode.
- *The erosion process is an unsteady one.* Each of the diagnostics in this chapter shows the anode erosion starting and stopping throughout the discharge, with predictable consequences for the voltage hash. This, it is now clear, is the reason for the non-constant statistical properties of the hash we discussed in Chapter 3.
- *Voltage hash may be the driver of, or be driven by, the anode erosion.* We have seen both these behaviors in this chapter. Figure 5.1 shows the hash suppressed by the erosion, while Fig. 5.2 shows the erosion jumping in magnitude along with the hash. This suggests that the behavior of the hash is not governed strictly by the erosion, or vice versa.

The insights that we have just enumerated shed light on why the two onset suppression mechanisms discussed in Chapter 1 work to reduce the voltage hash, while anode erosion—which, like the other two, adds mass to the discharge—does not. The two examples given were relatively controlled mass release sources: in the case of

anode propellant feed, mass was provided to the discharge at a constant rate; in the “stinger” experiment, the location of the evaporated mass source, in the hot plasma near the cathode, could ensure a more or less uniform erosion rate. By contrast, the erosion of the anode is neither predictable nor controllable—and so neither is its ability to suppress voltage hash.

# Chapter 6

## Experiments with a Constrained-Attachment Anode

### 6.1 Introduction

In the previous chapters, we have made a number of observations concerning the nature of the noise present in post-onset MPDT operation, and of the damage patterns present on anodes that have experienced onset. The physical insight into the onset problem we have gathered in the process is now sufficient to allow us to postulate a mechanism for altering the properties of the voltage hash.

It is worthwhile, at this point, to briefly review several of the most salient results of the last three chapters. These are:

- *The voltage hash is a random fluctuation with no characteristic time scale (within the range of our measurements) and statistics related to the value of  $J^2/\dot{m}$  but not the anode material.* We infer from the evidence that the formation of enhanced-current channels—anode spots—is a process rooted primarily in the plasma, and that it is stochastic, self-organizing into a random sequence of events.



- *Damage sustained by the anode has no characteristic size (within our measurement range).* The implication is that there is no typical energy delivered by an anode spot to the surface. From this we also infer that there is no characteristic spot lifetime, which implies that anode spots are inherently unstable structures.
- *Anode spotting occurs to some extent at all  $J^2/\dot{m}$  levels.* A lead anode, whose material properties make it most susceptible to damage, shows spotting at all  $J^2/\dot{m}$  levels, though the severity increases with  $J^2/\dot{m}$ .

The picture that emerges from these insights is the following. The current conduction to the MPDT anode is, to some extent, spotty at all current levels, though it appears for the most part to be diffuse at the lowest  $J^2/\dot{m}$  levels. The energy carried by the spots grows with  $J^2/\dot{m}$ , becoming sufficient to cause visible damage on the anode at some value of  $J^2/\dot{m}$  that depends upon the material characteristics. As the current conduction becomes increasingly spotty, the activity of spots increasingly affects the thruster impedance, and the perturbation that the spots cause to the voltage grows. The unsteady nature of the spots causes their lifetimes, energies, and occurrence to be stochastic, giving rise to the observed distribution in damage mark size and randomness in the voltage hash.

We have found that the severity of the damage suffered by an anode can be significantly decoupled from the occurrence of voltage hash by the choice of a suitable anode material. Hence, the problem of anode damage can be approached as a materials problem. To address the problem of voltage hash requires that we change the nature of the anode attachment, forcing the rapid occurrence of spot formation, movement, and extinction to proceed in a controlled way.

Perhaps the most straightforward way of accomplishing this is to heed the old adage, “If you can’t beat ’em, join ’em.” The occurrence of anode spots is a self-activated phenomenon—that is, the MPDT operator has no direct control over it. Our insights into the process have not made clear a way to force the current conduction to

remain primarily diffuse over a large range of  $J^2/\dot{m}$ . Instead, we reason, it would also be effective to find a way to stabilize the current conduction into a steady collection of spots.

## 6.2 The Constrained-Attachment Anode

Referring back to Fig. 4.6, the range spanned by the anode damage—and therefore, the anode spot attachments—is from  $\sim .01$ –10 mm. We clearly can eliminate attachments greater than any size  $d$  if the anode does not have any areas exposed with characteristic dimension greater than  $d$ . Because the arc self-organizes its attachments into a distribution of sizes, we cannot guarantee that the arc will not continue to attach in spots smaller than  $d$ . Nevertheless, if small areas of characteristic dimension  $d$  are the only possible attachment sites for the arc, we may presume that the current attachment will be significantly different than in the case of a completely exposed anode, and that the voltage hash will be commensurately affected.

On this logic, we created a new Constrained-Attachment Anode (CAA) to force a steady spot conduction pattern at the anode. A new graphite anode—chosen because we have observed graphite to be the material least susceptible to damage—was plasma-spray coated with a 0.25 mm layer of aluminum oxide, one of the most refractory ceramic materials available for the plasma-spray process. An azimuthally-symmetric pattern of 320 holes, each 0.5 mm in diameter, was laser-drilled through the ceramic to expose the graphite surface. 240 of these holes are on the outer face of the anode, separated radially by 6.35 mm and azimuthally by 9 degrees. The remainder of the holes are on the inner face, with the same radial and azimuthal separation. A photograph of the anode is shown in the left panel of Fig. 6.1.

The goal of this experiment is to change the characteristics of the thruster voltage hash as compared to the normal case of an exposed anode. There are two,

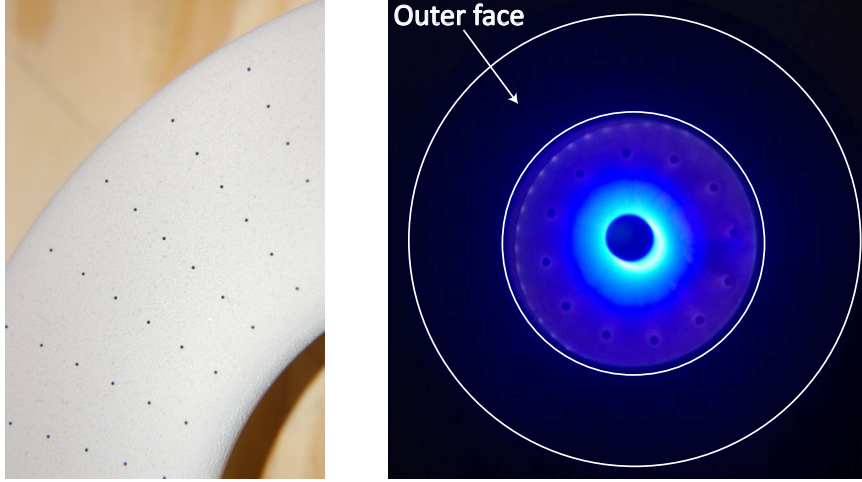


Figure 6.1: The alumina-covered graphite anode (left) with 0.5 mm holes exposing the conductive surface. A typical firing of the graphite CAA (right),  $J^2/\dot{m} = 97 \text{ kA}^2\text{-s/g}$ .

not necessarily separate, ways that a constrained-attachment anode can accomplish this. First, the spot attachment may be stabilized because the number of possible attachment configurations is restricted, whereas on an exposed anode the number of possible configurations is much larger. In this case, we may expect that the current densities of the anode spots will be much greater than those on an exposed anode, on which appreciable current also is collected in a diffuse manner. This greater spot current density will place greater thermal loads on the anode, and lead to greater erosion.

The second way that the CAA can stabilize the spot attachment is the reverse of the first. Because of the large thermal loads in the constrained spots, and the evaporation that follows, the near-anode discharge will be supplied with significant anode vapor—and this can be the cause of the spot stabilization. In what follows, we will explore the operation of the thruster with the CAA, and use the results to discuss the two possibilities, which is more strongly indicated, and how well we can distinguish between the two. Regardless of which of the above two mechanisms is more prevalent, however, we expect that anode erosion will be an important part of the thruster’s operation, and we should point out that without quantitative, comparative

erosion rate measurements—which we do not obtain in what follows—we cannot state unambiguously what the implications of our results are for the anode lifetime.

### 6.3 Operation and Voltage Behavior

The right panel of Fig. 6.1 shows a time-integrated photograph of a typical firing taken with the graphite CAA just described. Although there are many possible attachment locations on the outer face of the anode, the arc attachment stabilizes at the holes on the inner face, leaving the front (within the marked white boundaries in the photograph) dark. (Because the photograph in Fig. 6.1 is taken at a slightly oblique angle, the stable attachments on the inner left face are faintly visible.)

As anticipated, the mean voltage and the magnitude of the voltage hash for the CAA are significantly different than that of the exposed anode as a function of  $J^2/\dot{m}$ . Both are shown in Fig. 6.2, where for the exposed graphite anode the data points are reproduced from Chapter 3. The mean voltage is larger for the CAA at low  $J^2/\dot{m}$ , but increases linearly with a smaller slope than does the exposed anode, whose voltage quickly overtakes that of the CAA. The magnitude of the voltage hash, which rises quickly for the exposed anode starting between 80–100 kA<sup>2</sup>-s/g, does not do so for the CAA.

The results in Fig. 6.2 show that the thruster with the CAA operates at lower power, and with less noise, than its exposed-anode counterpart. The dramatic difference of the thruster behavior with these two anodes indicates a fundamental change in the thruster mode of operation. Because the difference between the two cases is the constrained anode attachment, the anode attachment must be the main influence on which mode is operative. We have stated before that it may be the constrained current attachment itself that is responsible for changing the thruster operation, it may be the resulting enhanced anode erosion that does so, or it may be

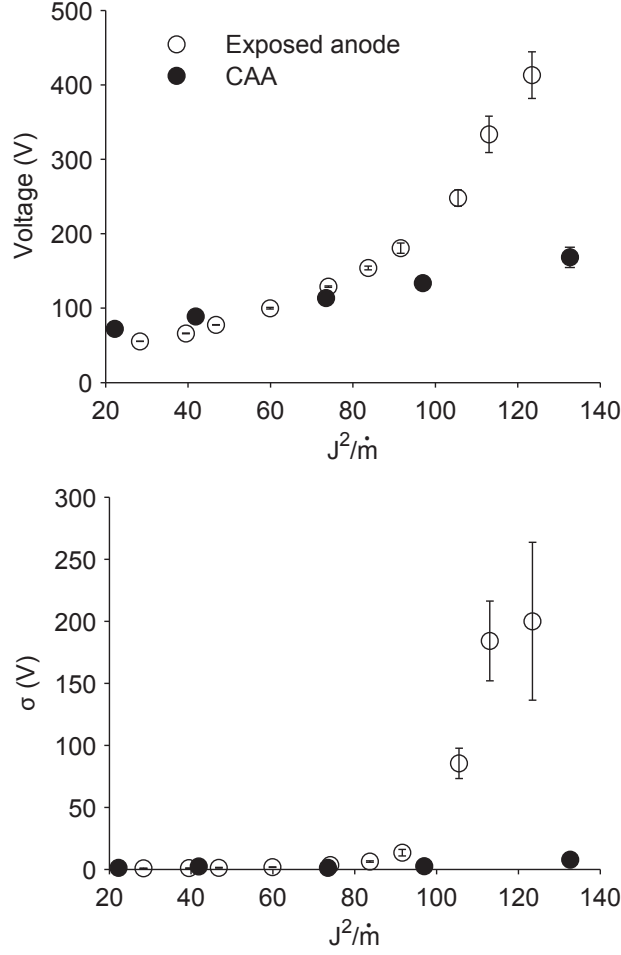


Figure 6.2: The mean value of thruster voltage and hash magnitude for both an exposed graphite anode and a graphite CAA.

a combination of both.

## 6.4 Erosion of the Constrained-Attachment Anode

We have succeeded, with the CAA, in significantly modifying the thruster voltage, and in particular, we have suppressed the voltage hash. However, because the important parameter governing voltage hash is  $J^2/\dot{m}$ , and the anode can be a source of  $\dot{m}$  as it erodes, we must gauge the significance of anode erosion to the operation of the CAA. To do this, we turn to the plume spectrum.

During operation of the FSBT with both the exposed graphite anode and

the graphite CAA, we obtained the time-integrated plume spectrum using an Ocean Optics fiber-coupled CCD spectrometer. Both the coupling fiber and the spectrometer have sufficiently wide optical bandwidth that the whole visible spectrum and the near infrared from 400–900 nm can be recorded. A large number of species are present in the thruster plume: argon (propellant), carbon (anode), tungsten (cathode), aluminum (ceramic covering, in the case of the CAA), silicon (quartz chamber insulator), boron and nitrogen (backplate), and oxygen (from a number of the preceding). Having accounted for all of these, however, in what follows we will see that the most conspicuously significant species is carbon.

Figure 6.3 shows the optical spectrum of the FSBT operating with an exposed graphite anode and the CAA, operating at  $J^2/\dot{m} \sim 125 \text{ kA}^2\text{-s/g}$  (at which condition the voltage hash magnitude is large for the exposed anode, and quite small for the CAA). Labeled in these two figures are spectral lines corresponding to argon and carbon. Argon emits light at a large number of wavelengths, many of them in the longer-wavelength end of the visible spectrum (hence the characteristic blue color of the discharge in the photographs). Of greatest note in these spectra are the two strong lines which lie at 658 nm and 723.7 nm in the CAA spectrum (marked with arrows in Fig. 6.3), which have no counterpart in the exposed anode spectrum. Neutral and singly ionized carbon are responsible for these lines. Nowhere in the CAA spectrum are there unambiguous aluminum lines, as we would expect if the aluminum oxide ceramic evaporates significantly.

We noted, in Chapter 4, that the graphite anode showed no significant damage at any  $J^2/\dot{m}$  level at which we operated it. The spectra just discussed show that carbon does not have a significant presence in the spectrum. In the case of the CAA, however, it is apparent from the spectrum that we have caused significant erosion by constraining the anode attachment.

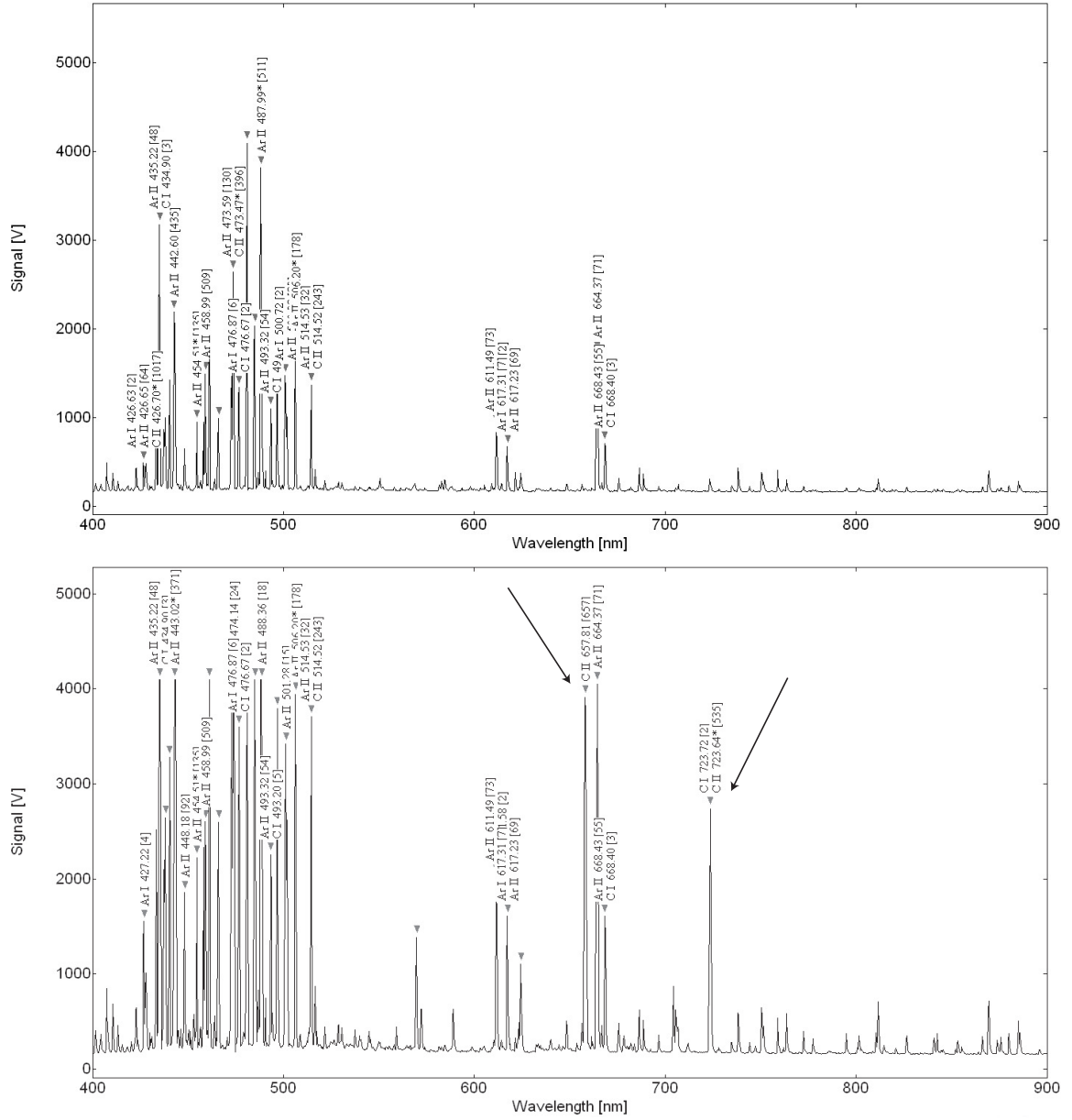


Figure 6.3: Optical spectra of the FSBT plume operating at  $J^2/m \sim 125 \text{ kA}^2\text{-s/g}$  with (top) an exposed graphite anode, and (bottom) a graphite CAA.

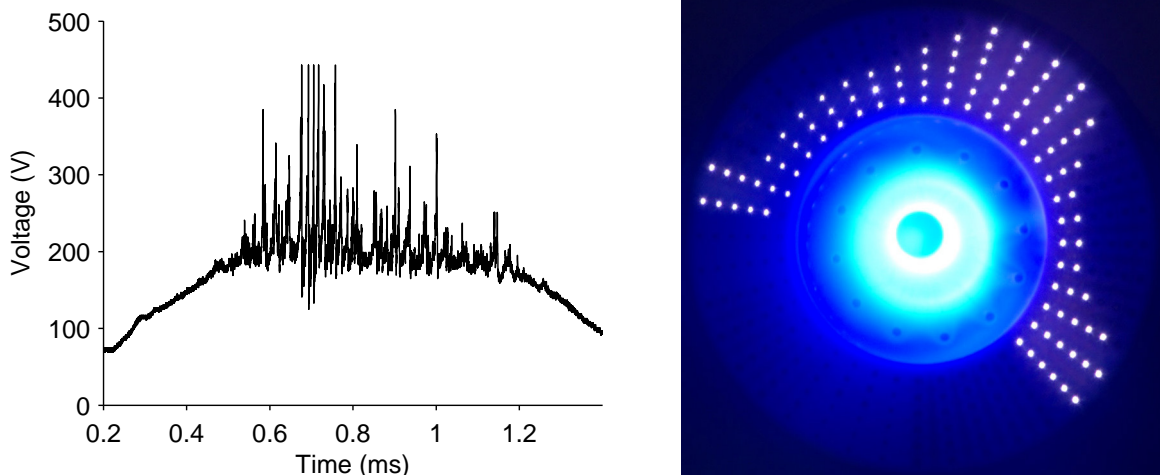


Figure 6.4: Voltage trace (left) and all-light photograph (right) of the FSBT with graphite CAA operating at  $J^2/\dot{m} \sim 130 \text{ kA}^2\text{-s/g}$  during a firing with voltage hash.

## 6.5 Voltage Hash with the Constrained-Attachment Anode

It happens, in a small percentage of firings at high  $J^2/\dot{m}$ , that the FSBT operating with the CAA will exhibit voltage hash. An example of such a voltage trace is shown in Fig. 6.4, along with an all-light photograph of the thruster for the same firing. The photograph is clearly different from that in Fig. 6.1, in which no attachment on the outer face of the CAA can be seen. It is always the case when using the CAA that there is attachment on the anode outer face when the voltage contains hash. The optical spectrum for this firing is shown in Fig. 6.5. The strong carbon spectral lines, so prevalent in the CAA case of Fig. 6.3, are absent in this spectrum.

That the voltage should ever exhibit hash implies that the CAA encourages, but does not mandate, that the anode attachment stabilize. When the attachment wanders, it moves from the inner attachment points to the outer face, where—a sampling of photographs suggests—it activates groups of attachment points on the outer face at random. When this is the case, the attachment is apparently not sufficiently stable to heat the anode and cause erosion of the same magnitude seen



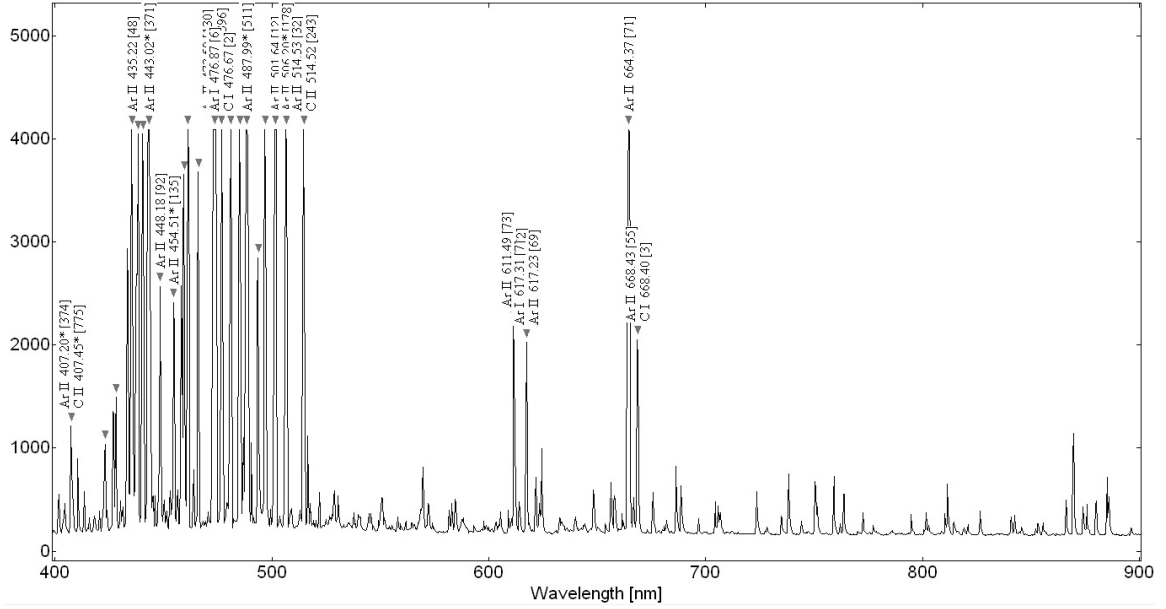


Figure 6.5: Optical spectra of the FSBT plume, for operation at  $J^2/\dot{m} \sim 130 \text{ kA}^2\text{-s/g}$  for the case shown in Fig. 6.4.

when it is stable.

## 6.6 Discussion

We have already seen, in Chapter 5, that when anode vapor is present in large enough amount to span the gap between the anode and cathode, the voltage hash is suppressed. The result that we have seen in the data presented in this chapter—that significant carbon presence in the plume coincides with noiseless voltage—is consistent with that observation. The difference is that, while the erosion observed in Chapter 5 was unsteady—and so, therefore, was the effect on the voltage hash—the effect we have seen using the constrained-attachment anode is steady. It is clear, therefore, that we have stabilized the anode erosion by constricting the current into small spots.

The differences in the voltage properties of the two anodes can be explained in terms of this anode erosion. The mean voltage of the CAA increases slowly with

$J^2/\dot{m}$ , in much the same way as it does for the exposed anode at low  $J^2/\dot{m}$  values. The voltage with the exposed anode, however, increases in slope as  $J^2/\dot{m}$  increases, a behavior that is understood in terms of propellant ionization [58]. That the voltage with the CAA does not do this implies that eroded anode material is sufficiently abundant to keep the effective  $J^2/\dot{m}$  at a low level throughout the range of the measured  $J^2/\dot{m}$ . In the same way, just as at low  $J^2/\dot{m}$  the exposed anode does not give rise to voltage hash, neither does the CAA at any tested value of  $J^2/\dot{m}$ . The presence of carbon emission in the spectrum of the CAA, but not that of the exposed anode, supports this view.

This tidy picture of the influence of eroded anode material still leaves open the question of which comes first: the stable current attachment that enables erosion, or the erosion that helps stabilize the attachment? Our best indication of the answer to this question comes from our observation that in a small percentage of firings, voltage hash can be present while carbon is not present in the spectrum. Whether voltage hash is present or not, the constriction of current into small spots will cause the heat loads on the graphite to be large; with large power input in both cases, the difference between the two is in how long the attachment at the spots exists. If the attachment is unstable, it will extinguish and move elsewhere before the graphite has reached surface temperatures large enough for significant erosion; if the attachment is stable, the graphite will become hot enough to erode significantly. While the entrainment of anode vapor will undoubtedly stabilize the anode attachment, it seems to be the case that for the erosion to begin in the first place requires some degree of initial stability.

An exposed anode, with an infinite number of attachment configurations, offers no such initial stability. The CAA, however, does provide this stability by forcing high-conductivity channels to form at isolated points in the near-anode plasma. As we have seen, the points the arc generally stabilizes upon are those on the internal anode face, closest to the cathode; geometry dictates that these points are the preferable

points for the initial breakdown, and the current conduction on them is apparently maintained thereafter.

We have also seen that firings involving unstable attachment generally have some attachment on the anode outer face as well. This suggests that, due to some perturbation, the initial breakdown may have occurred between the cathode and some outer points. Barnett [30] has shown that current attaching to the outer anode face is unsteady at high  $J^2/\dot{m}$ ; it may be that the CAA is not effective at combating this unsteadiness, which leads to voltage hash and the lack of significant graphite erosion during these firings. These observations do not fully clarify the chicken-or-egg dilemma of whether stabilized attachment leads to erosion, or erosion leads to stabilized attachment; but they suggest that, at least at the beginning of a firing, the arc stabilizes first.

## 6.7 Summary and Insights

The constrained-attachment anode that we have used in this chapter forced current conduction to the anode to occur in small (0.5 mm diameter) areas distributed over the anode surface, and discouraged the easy movement of those attachments once formed. The differences that we have observed between operation with this CAA and with a normal exposed anode have reinforced two lessons that we have learned over the course of our study of onset.

- *Stable current attachment on the anode is necessary for a quiet thruster voltage.*

In Chapter 3 we reproduced signals with the statistical properties of voltage hash with a model whose first assumption was that the current attachment on the anode was unsteady. Using the CAA, we have steadied the attachment—and by doing so we have settled the thruster voltage.

- *Energy input to anode surface areas—and not the mechanism behind voltage*

*fluctuations—is primarily responsible for anode erosion.* Just as, in Chapter 4, we saw that voltage hash and anode erosion are largely decoupled processes, here we have seen that the erosion is greater when the attachment is stable than in those cases in which it is not. It is the larger energy input to stable attachment points that leads to the greater erosion, whereas the unstable attachment that leads to voltage hash reduces the energy input to, and concomitant erosion at, any particular attachment point.

Because voltage hash can be suppressed by stabilizing the anode attachment, and anode erosion can be suppressed by either reducing the energy input to the attachments or raising the temperature tolerance of the anode material, future work attempting to resolve the onset problem should focus on these two challenges. We suspect that an MPDT that can incorporate solutions to both will experience far less of the detrimental effects associated with onset.

# Chapter 7

## Conclusion

### 7.1 A Broad Overview

It was our intention in this dissertation to understand the origin of the onset phenomenon in the MPDT, as a step in the long-term development of ways to mitigate its negative consequences. Reviewing the literature, we saw that all previous knowledge concerning raising the value of  $(J^2/\dot{m})^*$  can be in some way reduced to enhancing the plasma density, and thus the plasma’s current-carrying capability, near the anode. Barring further optimization of the thruster geometry, any additional suppression of onset phenomena have involved adding mass to the discharge—and so involve no more fundamental insight than the identification of  $(J^2/\dot{m})^*$  as a scaling parameter, which has long been known.

Our approach has been to first gain some insight into the origin of the onset phenomena—voltage hash and anode damage—and from this deduce the likely physical mechanisms responsible. In doing so we have carried out a detailed investigation of the voltage hash, a detailed investigation of the damage left behind on the anode, and a time-resolved investigation of the relationship between the two. In broad overview, our results are consistent with the suggestion that current conduction to the anode

becomes starved at a value of  $J^2/\dot{m}$  at which the random thermal flux of electrons to the anode is insufficient to carry the entire current imposed on the thruster. As this happens, the amount of current carried through spots, which are regions of enhanced conductivity, increases; when the power deposited in the anode by these spots becomes sufficiently large, the anode material begins to show signs of damage. Anode vapor is then released into the thruster plume in an amount dependent upon the power input to the anode spot. To this extent, the findings in this work are consistent with those of the most recent work on the subject [14].

## 7.2 Summary of Findings

### 7.2.1 Voltage Hash

We have shown that the voltage hash is an essentially random fluctuation, without a characteristic time scale within our measurement range but instead a distribution of the signal power that goes with frequency like  $1/f^\beta$ , with  $1 \leq \beta \leq 2$ . This randomness leads to a different interpretation of voltage hash than would a strong characteristic time scale: instead of seeing the hash as arising from the repetition of a particular deterministic process, we see that it is instead the result of a stochastic process without a characteristic scale that can be used to help identify it. Instead, we have examined the statistics of the voltage hash, and have seen that there is a distinct behavior with rising  $J^2/\dot{m}$ : the statistics first trend away from Gaussian, and then at  $J^2/\dot{m} \sim 110 \text{ kA}^2\text{-s/g}$  begin the trend back toward Gaussian. This process proceeds in the same way for copper, graphite, and lead anodes, which possess a wide range of thermal properties—implying that the driver behind voltage hash is largely independent of the anode.

We have developed a model of the likely voltage signature caused by an anode spot. By taking the random superposition of a number of these events, we

have generated voltage hash with statistics matching the empirical hash, including the degree of non-normality and the  $1/f^\beta$  fall in the power spectrum. Then, by comparison of the two, we conclude that as  $J^2/\dot{m}$  rises toward 110 kA<sup>2</sup>-s/g, the amount of current conducted through individual spots increases, leading to larger, faster voltage events for each spot, and hence a greater deviation from Gaussian statistics. After about 110 kA<sup>2</sup>-s/g, however, the return of the statistics toward Gaussian implies that a greater number of anode spots appears to conduct current to the anode.

We have suggested that above  $J^2/\dot{m} \sim 110$  kA<sup>2</sup>-s/g, the current to the anode begins to fragment into filaments, leading to the greater number of anode spots. This suggestion was supported both by the possible existence of sufficient conditions for filamentation in the MPDT plasma, and by the harder evidence of photographic confirmation that filamentary structures do exist in the MPDT and have properties consistent with our interpretation of the voltage hash data.

### 7.2.2 Anode Damage

We have observed that the anode damage in the MPDT concentrates in isolated areas. We have observed no characteristic size for these areas—indeed, the dimensions  $d$  of the damage span several orders of magnitude, from the smallest observable to on the order of the anode size (roughly  $10^{-1}$ – $10^2$  mm). The distribution of the sizes  $\sim d^{-\delta}$ , where  $\delta \geq 1$ . From this we deduce that the anode spots, which are responsible for this thermal damage, nucleate at microscopic sizes and grow, with a power-law probability of extinguishing at any size  $d$  before growing to larger size. We have also presented a picture of the growth process through a comparison to experiments in the literature.

Perhaps most importantly, we have found that while the severity of the anode damage increases with  $J^2/\dot{m}$ , it is more sensitive to the thermal properties of the anode material itself—graphite, a refractory, was the least-damaged anode material

used in this work. While this may appear to be a trivial observation, it changes the prevailing view of the *raison d'être* of the anode spots. Clearly the spots release anode material into the discharge—but in different amounts depending on the thermal properties, not in an amount which is strictly sufficient to solve the starvation crisis, as suggested by Diamant’s previous work [14]. From this we see that the anode is primarily a passive player in the discharge, responding to the action of anode spots according to its thermal characteristics.

### 7.2.3 Relationship Between Voltage Hash and Anode Damage

We have learned that anode erosion accompanies voltage hash, or that it suppresses it, depending upon the extent of the erosion. This has been inferred before from time-integrated diagnostics, but we have shown that it holds true on a time-resolved basis as well: anode material is released into the discharge concurrent with periods of voltage hash; but if sufficient material is released, the voltage hash may be suppressed entirely. The definition of “sufficient” appears, from the evidence in our high-speed videos, to be enough material that a bridge is formed from the anode to the cathode—essentially providing a short circuit between the two. Based on our knowledge of the anode starvation process, however, it is most likely that though the anode vapor bridge does reach to the cathode, such extent is not strictly necessary to suppress the hash: if the vapor is sufficient to bridge the low-plasma-density region adjacent to the anode, that may be what is required for the suppression. The unsteadiness of the erosion is the main driver of the time-varying hash statistics.

### 7.2.4 Use of the Constrained-Attachment Anode

We have reasoned that, since the voltage hash is a random process that arises from the random formation of current attachments in anode spots, we can stabilize the thruster voltage by stabilizing the anode attachment. Our constrained-attachment



anode forced the current to attach in small areas symmetrically spaced over the anode surface, and thereby restricted the possible attachment locations and sizes. By restricting the degree of randomness possible in the attachment, we have dramatically increased the likelihood that the attachment will be stable, and the voltage along with it. While we have not succeeded in both eliminating voltage hash and anode erosion simultaneously, we have shown that we may, with proper anode materials or preparation, eliminate one or the other. Our observations have also not ruled out the possibility that, with the appropriate ingenuity, both may be eliminated simultaneously.

## 7.3 Insight into Onset Phenomena

The findings of this work, when taken together, shed light on a number of questions that have surrounded the onset problem for many years. We have asked detailed questions about the nature of the voltage hash, but we may go further than answering only our own questions. For example:

- *We have shown experimentally, as past theoretical work has suggested, that the anode starvation and plasma instability theories of onset are not mutually exclusive.* In Chapter 1 and Appendix D, we describe the debate between anode starvation and plasma instability theories of onset. We explained how past literature showed them to be equally good at predicting  $(J^2/\dot{m})^*$ . While Diamant [19] has provided convincing evidence that anode starvation occurs in the FSBT, our observation that anode spotting is independent of the anode material argues that it is a primarily plasma phenomenon—and it requires an instability of some sort, as we discussed in Chapter 3, to form anode spots from an initially diffuse discharge.
- *We have updated the prevailing view on the role of anode spots.* Diamant [14]

described anode spots as arising from local overheating of the anode, and surmised that the amount of material released by spotting was enough to sufficiently solve the starvation crisis. We have shown that in fact the anode damage is more dependent upon the anode material properties than on  $J^2/\dot{m}$  (which is the driver of starvation).

- *We have shown that anode erosion and voltage hash are largely decoupled phenomena.*

It has long been the presumption that voltage hash and significant anode erosion accompany one another, beginning at  $(J^2/\dot{m})^*$ . We have demonstrated that the two do not go hand in hand, but are driven by separate drivers— $J^2/\dot{m}$  for voltage hash, thermal properties for anode erosion—which happen to take effect at similar operating conditions for many anode materials used in past studies.

## 7.4 Open Questions

A number of questions still remain at the end of this investigation, some of which arose as a result of our observations. Primarily, our approach has been empirical and phenomenological, which leaves open at least one important theoretical avenue which, if pursued, could yield better fundamental insight into the phenomena we have described. In the same way, carrying our experiments further than we have for this dissertation will further our understanding of the technical usefulness of our findings.

Perhaps most importantly, we have, like others before us, invoked an anode spot model to describe both the voltage hash and anode damage without being specific about why the anode conduction should be spotty in the first place. We have not identified the plasmadynamic drivers behind the contraction of current into a spot, or those behind the extinction of a spot once it forms. A stability analysis in at least two dimensions will be required to show the development of an area of enhanced current density out of a homogeneous background—and perhaps the solution to that problem

will shed light on the origin of the randomness of the formation process. Likewise, a stability analysis of the current channel of a spot already formed should reveal why a spot extinguishes, and may give insight into the reasons behind the power-law distribution of anode spot damage sizes. The contribution of this dissertation to the theoretical modeling of anode spotting phenomena is to point out that the filamentation instability, which is documented in other devices, is very likely a driver of anode spotting at high  $J^2/\dot{m}$ —and that the theoretical treatment just prescribed would find a fruitful starting point with an investigation of filamentation. The modification of the theory already developed elsewhere, for application to the MPDT plasma, would show whether this mechanism, so fundamentally important in similar systems like the plasma focus, plays a part in onset. We expect, based on the experimental evidence provided in this work, that such a theoretical analysis will answer this query in the affirmative.

In the area of thruster design, we have shown that use of the constrained-attachment anode can be a voltage stabilizing mechanism, though the stable voltage in that case was accompanied by significant erosion. In our discussions, we suggested that an MPDT that could both stabilize the attachment and reduce anode heat loads would see a decline in detrimental onset phenomena. Doing both has at times been attempted with the application of a magnetic field [59], but applied fields come with increases in system complexity. The full theoretical treatment of current constriction and filamentation that we have recommended may suggest damping mechanisms that serve to keep the anode current conduction mostly diffuse and overcome the anode starvation problem, which would serve both to make the attachment more steady and reduce anode heat fluxes. Barring that, the identification and use of a more refractory material than our graphite—for example, a pyrolytic graphite—may allow the stabilization of the attachment in a number of spots, as on our CAA, without significant accompanying erosion. In any case, such an empirical solution should

include measurements of the performance characteristics (thrust and efficiency) of the modified MPDT. In theory, the  $J^2$  dependence of the thrust and the  $I_{sp}$  is not influenced by the anode conduction geometry; but the difference in the voltage characteristics between an exposed anode and a CAA suggests that the performance of the thruster using the two anodes may be different. Only performance data using the CAA, or any other onset suppression scheme, would provide information one way or the other.

The former suggestion, of modeling the anode spot formation and extinction, would amount to a satisfactory theoretical description of the onset phenomena. Successful results of the latter suggestion, enhancement of the CAA technique or development of an equivalent onset suppression scheme, coupled with performance measurements, would represent a leap forward in our ability to control the behavior of the MPDT at high  $J^2/\dot{m}$ . This dissertation has aimed to provide a bridge between the unclear implications of the work in the literature and the clarity that would come with the successful conclusion of either of these tasks.

# Appendix A

## Voltage Hash Influence on MPDT Current

### A.1 The MPDT Current

In discussions of onset, we generally refer to the thruster current as being some value and compare it to the critical onset current. In order to make such statements, we must have an unambiguous definition of the thruster current. This makes it worthwhile to ask how the large-magnitude voltage hash affects the thruster current, and whether that effect is small enough to ignore. In this appendix, we will answer that question in the affirmative.

#### A.1.1 Expectation

We may get a feel for how the MPDT voltage hash during onset will affect the current through the thruster by looking at the current driven in the power-supply cabling by the  $V(t)$  in the model of Sec. 2.2.2. The Laplace space representation of the current,

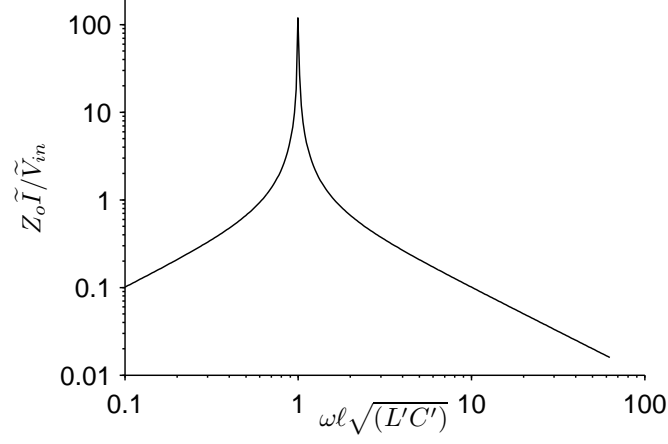


Figure A.1: The frequency-dependent current response of the power supply cabling to  $V(t)$ . The resonance at  $|\kappa| = |i\omega\ell\sqrt{L'C'}| = 1$  corresponds to the fundamental resonance in the voltage transfer function shown in Fig. 2.7.

in terms of the nondimensional frequency  $\kappa$ , is

$$\frac{Z_o \tilde{I}}{\tilde{V}_{in}} = \frac{\kappa}{\kappa^2 + 1}. \quad (\text{A.1})$$

$Z_o = \sqrt{L'/C'}$  is the characteristic impedance of the cabling. Equation (A.1) relates the current driven through the cabling due to  $V(t)$  to the magnitude of  $V(t)$  as a function of frequency. A plot of this function is shown in Fig. A.1, which manifests a sharp resonance around the resonant frequency  $\omega = 1/\ell\sqrt{L'C'}$  of the cabling. This resonance indicates that the cabling presents a much lower impedance to current flow at this frequency than at others, so that currents at the resonant frequency will be dominant in the signal.

Since  $Z_o$  of our cabling is  $50 \, \Omega$ , a  $1 \, \text{V}$  signal applied by  $V(t)$  at the resonance (which for the FSBT is  $1.3 \, \text{MHz}$ ) will produce a  $\sim 2.4 \, \text{A}$  current. The voltage hash, as shown in Fig. 2.7, can reach magnitudes as high as  $500 \, \text{V}$ , but with power concentrated in frequency bands far off the resonance, which is  $1.3 \, \text{MHz}$  in our setup. For example, a  $500 \, \text{V}$  signal at  $500 \, \text{kHz}$  would affect the current through the thruster by  $\sim 5 \, \text{A}$ , an amount too small to be noticed. At  $1.3 \, \text{MHz}$ , the current effect would be

on the order of 1 kA, but the magnitude of this frequency component in  $V(t)$  is much smaller than that of the frequency range below 1.3 MHz. This leads us to expect that the current measurement will show relatively low-amplitude (as compared with the mean) oscillation about the mean at 1.3 MHz, and very little variation at other frequencies of interest.

### A.1.2 Current Measurement

The FSBT current was measured in two places to test this assertion: at the output of the PFN, using a Pearson 301X current transformer, and at the base of the thruster cathode, using a Rogowski coil constructed specifically for this purpose, as described in this section.

The current diagnostic we chose to incorporate *a posteriori* into the FSBT setup was a Rogowski coil, because this could be made smaller than a ferrite-core transformer, and is not prone to core saturation at the high currents being measured. Recently [60–62], a method of mass-producing identical Rogowski coils of varying sizes and sensitivities has been developed based on printed circuit boards (PCBs). In these designs, the coil is produced by connecting printed traces on alternating sides of a silicon board with vias, or plated through-holes. This produces a coil with a rectangular poloidal cross-section, and because the manufacture is based on an automated process, many identical coils can be cheaply produced. This also makes it easy to control the coil’s inductance and interturn capacitance, which together work to determine the bandwidth and sensitivity of the ideal measurement. Coil-only bandwidths of 10 MHz or more [62] and very small response to external currents [60] have been reported.

The peculiarity involved in designing a Rogowski coil appropriate for the FSBT is the small mutual inductance,  $M$ , required by the electronics and the constrained geometry. As the design of the coil itself is a topic that has received substantial

Table A.1: Values of the Rogowski coil equivalent circuit parameters

Parameter	Value
$L_c$	48.5 nH
$C_c$	2.66 pF
$R_c$	0.475 $\Omega$
$M$	1.35 nH
$L_\ell$	2.16 $\mu$ H
$C_\ell$	360 pF

coverage elsewhere [60, 62], we will not again describe that aspect of the system. We will instead focus on the unique peculiarities encountered when using a coil of small inductance at a location distant from the recording electronics.

The Rogowski coil is terminated in recording electronics through 12 feet of twisted-shielded pair cabling. Because we are, in this setup, only interested in signal frequencies below a few MHz, the 12 feet of cabling is far shorter than the wavelengths of interest. The cabling can therefore be treated as a lumped inductance and capacitance (with resistance negligible compared with the termination). In this case, the Rogowski coil system equivalent circuit is shown in Fig. A.2, with the cabling elements shown as  $L_\ell$  and  $C_\ell$ . The Rogowski coil itself is shown as a lumped  $R_c$ ,  $L_c$ , and  $C_c$ , and the applied voltage source is proportional to the derivative of the current enclosed by the coil:

$$V(t) = M \frac{dI}{dt}(t). \quad (\text{A.2})$$

The coil parameters are determined by the specified coil geometry, and for our coil—shown photographed in Fig. A.4—can be calculated in the ideal case [63] as shown in Table A.1. In practice, only small ( $< 1\%$ ) deviations from these values may be expected thanks to strict circuit board printing tolerances.

The small values of  $L_c$  and  $C_c$  are a consequence of meeting the design criteria of the first paragraph. The value  $M = 1.35$  nH means that the typical current rise of our PFN pulse,  $\sim 10^8$  A/s, will produce a 100 mV output across the Rogowski coil,



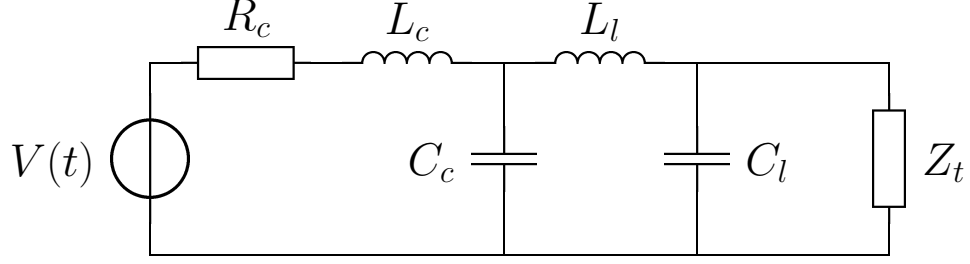


Figure A.2: The Rogowski coil system equivalent circuit.  $V(t)$  is the Rogowski output voltage,  $R_c, L_c, C_c$  the coil parameters, and  $L_\ell, C_\ell$  the cabling parameters, all given in Table A.1.  $Z_t$  is the impedance terminating the cabling.

and any large, faster transients are unlikely to produce more than 2 V output, which marks the linear range of the signal conditioning electronics.

The values of  $L_\ell$  and  $C_\ell$  given in Table A.1 are calculated for the specific values of the cabling used in our setup: 12 ft of Belden 9452 twisted shielded pair, with published values of inductance and capacitance per foot of  $0.18 \mu\text{H}$  and  $30 \text{ pF}$ , respectively. An important point to notice is that  $L_c \ll L_\ell$  and  $C_c \ll C_\ell$ , and will be for any practical length of cable. We immediately conclude that the cabling will have a dominant effect on the dynamical response of the system, a conclusion that is borne out in an analysis of the transfer function.

The transfer function of this system is

$$\frac{\tilde{V}_{Z_t}}{\tilde{V}(t)} = Z_t \left\{ Z_t C_c C_\ell L_c L_\ell s^4 + C_c L_\ell (L_c + Z_t C_\ell R_c) s^3 + [Z_t (C_c L_c + C_\ell (L_c + L_\ell)) + C_c L_\ell R_c] s^2 + [L_c + L_\ell + Z_t R_c (C_c + C_\ell)] s + (R_c + Z_t) \right\}^{-1}. \quad (\text{A.3})$$

Equation (A.3) contains two important insights, which are evident in the curves of Fig. A.3. The first we have already stated: the electrical properties of the cabling connecting the Rogowski coil to the termination have a significant effect on the frequency response, the result of  $L_c \ll L_\ell$  and  $C_c \ll C_\ell$ . Curves (a) and (b) show the frequency response of the coil system without and with inclusion of the cabling

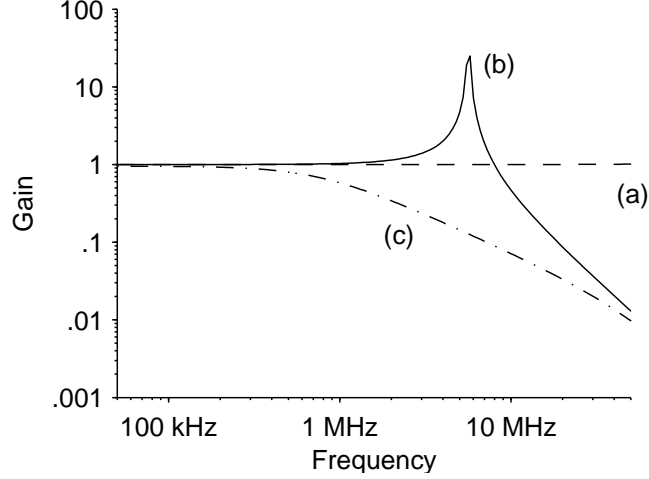


Figure A.3: The calculated frequency response of the PCB Rogowski coil (a) alone, terminated into 56 k $\Omega$ ; (b) with 12 ft of twisted shielded pair cabling terminated into 56 k $\Omega$ ; and (c) like (b), but terminated into 10  $\Omega$ .

parameters: it is apparent that cabling lowers the bandwidth of the measurement. The cabling should therefore be made as short as possible, to lower  $L_\ell$  and  $C_\ell$ . In our experiment, 12 ft is the minimum length necessary to move the signal out of the vacuum tank to the digitizing electronics, which could not be moved inside.

The second insight involves the termination impedance  $Z_t$ . Without the effect of the cabling, the value of  $Z_t$  does not matter until the frequency of the signal becomes very large, when the combination of  $L_c$  and  $Z_t$  forms a low-pass filter that effectively integrates the signal. With the much larger value of  $L_\ell$ , however, the pole of the low-pass filter formed by  $L_\ell$  and  $Z_t$  sits at a much lower frequency and may attenuate frequencies of interest. In response to this, the signal of the coil should, in general, be terminated into a high impedance. (The relevant comparison is between  $Z_t$  and  $\sqrt{L_\ell/C_\ell}$ .) Curve (c) in Fig. A.3 shows the response of our system with  $Z_t = 10 \Omega$ ; in contrast, curves (a) and (b) are calculated with  $Z_t = 56.2 \text{ k}\Omega$ .

We installed the Rogowski coil into the FSBT assembly at the axial location labeled “Coax” in Fig. 2.1. Because in this location the Rogowski coil is surrounded by an assembly floating at cathode potential, the coil is insulated by a G10 housing,

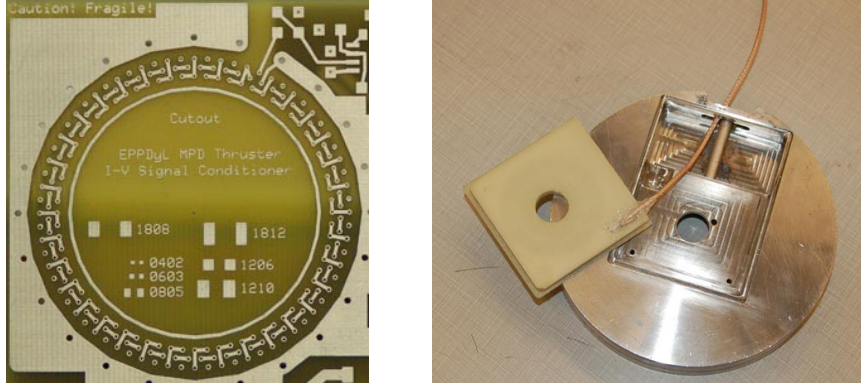


Figure A.4: (left) A picture of the printed Rogowski coil. Visible are the top traces (L-shaped) and the return lead through the center of the coil. (right) The enclosed coil at its installation location: the cathode is inserted through the hole in the G10, which aligns with the hole in the steel backpiece.

whose dielectric strength is sufficient to hold off several thousand volts and whose hardness is sufficient to withstand the pressure required to ensure the cathode makes good electrical contact with the rest of the thruster. The housing is sealed with a silicon RTV. The coil assembly is shown in Fig. A.4.

The proximity of the coil to the arc allows the coil and its cabling to pick up a significant amount of electrical noise. We have found it insufficient merely to fit the Rogowski coil with an electrostatic shield surrounding the windings at ground potential—such a configuration, in which one end of the coil is grounded to the shield, and the other is brought out on the center conductor of a coaxial cable, allows the signal to be corrupted by a significant amount of common-mode noise. Instead, as already pointed out, we use twisted shielded pair, with the shield grounded at one end of the line and connected to the Rogowski coil shield at the other, to bring the coil signal to the recording electronics differentially. The signals on the twisted pair are then subtracted by an active balanced/unbalanced signal converter [64], whose 20 MHz bandwidth is sufficient to pass all frequencies of interest. This balanced signal transmission greatly attenuates common-mode signals, as any noise picked up at the coil or along the cabling is transmitted equally along both conductors and is

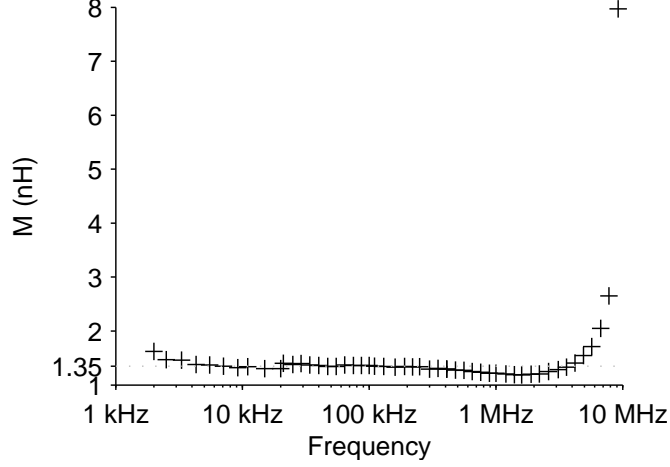


Figure A.5: The measured Rogowski coil mutual inductance over the range of frequencies encountered in the FSBT. Uncertainties in the measurement are represented by the vertical size of the data markers.

therefore subtracted out of the final signal.

Because of the effect of the cabling on the Rogowski coil output, we calibrate the coil only after it is installed into the FSBT. A sinusoidal current with a known amplitude  $I$  and frequency  $\omega$  produces a measured output  $V_{out}$  from the coil; using the Fourier transform of Eq. (A.2),  $M = V_{out}/\omega I$ . Any amplitude  $I$  can be used for the calibration, because the Rogowski coil produces a linear response; however, because  $M$  is small, the coil output approaches the measurement resolution of standard oscilloscopes for small  $I$  and  $\omega$ , using available RF power amplifiers. Figure A.5 shows the in-situ calibration performed on our setup. Approaching several MHz, the curve begins to rise as the resonance described in the last section is approached; in the low kHz, the value of  $M$  begins to rise as well, but due only to difficulty in measuring the low signal output at such low frequencies. Ignoring such low frequencies, and frequencies approaching resonance (which are above our frequency range of interest), the mean value of the calculated mutual inductance is  $M = (1.32 \pm .05)$  nH, in favorable comparison with the calculated value  $M = 1.35$  nH from Table A.1.

To simplify the setup, we digitize the output of the Rogowski coil and numerically

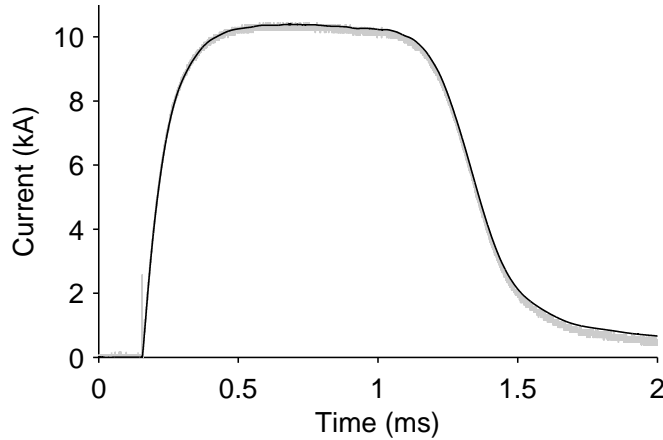


Figure A.6: A comparison of the Rogowski coil output (black trace) and that of a commercial current transformer (gray trace) for a 10 kA test pulse.

integrate *a posteriori*. Figure A.6 shows a comparison between the current as measured by our Rogowski coil and that of the Pearson transformer. The favorable agreement provides assurance that the coil behaves as anticipated.

The Rogowski coil was used to check the effect of the cabling resonance on the thruster current. Figure A.7 shows the voltage and current across and through the FSBT during a firing above onset. The voltage trace is a random signal as discussed in Chapter 3. On the other hand, the dominant frequency in the current trace is 1.3 MHz, reflecting the much lower line impedance presented to this frequency compared with all others. During even the most pronounced of the voltage hash, the current variation is only hundreds of Amperes, small compared to the mean current ( $\sim 19$  kA). We conclude that though the effect of the power supply line is manifest in the current trace, it is not of a sufficient magnitude to cause concern in the interpretation of onset phenomena.

The current values reported in this dissertation represent the mean value of the flat top of the quasisteady current pulse, without reference to the small effect of the cabling.

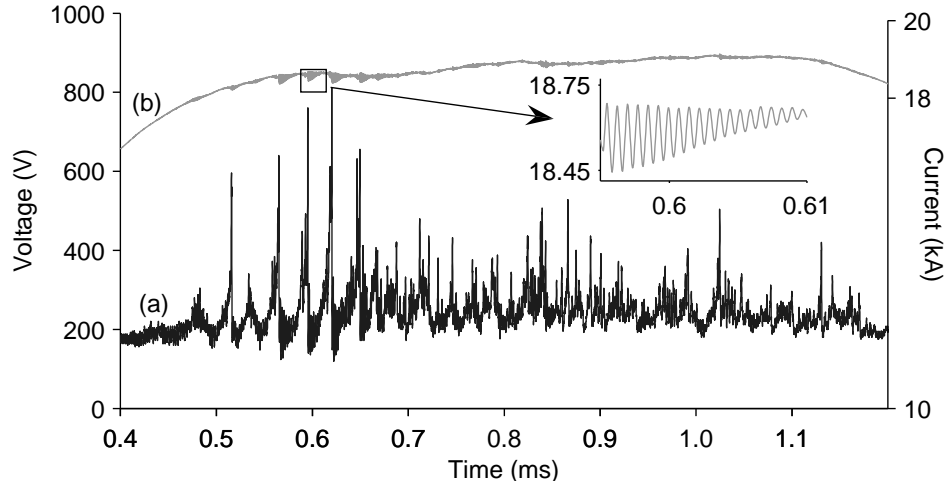


Figure A.7: The voltage (a) and current (b) across and through the FSBT during a firing above onset ( $J^2/\dot{m} = 80 \text{ kA}^2\text{-s/g}$ ). The jumps in the thruster voltage set off current oscillations with an amplitude of hundreds of Amperes and a frequency of 1.3 MHz, but the forms of the voltage transients themselves are not reproduced in the current trace (inset).

# Appendix B

## Cathode Tip Current Measurements

The pinching component of the Lorentz force is usually invoked to explain the cause of anode starvation in the MPDT. We suspect, therefore, that the voltage hash should only begin when the pinch is sufficiently developed, and we wish to verify this. In this section, we describe an experiment to measure the temporal variation of the current blowing downstream of the cathode tip; we will show that the appearance of voltage hash is correlated in time with the appearance of a significant axial current extending downstream of the cathode tip, an indication of a well-developed plasma pinch.

That a fraction of the thruster current extends downstream of the cathode tip in this MPDT during the quasi-steady portion of the thruster firing has long been established [8,9,30]; the fraction of the current blowing out of the thruster increases as  $J^2/\dot{m}$  increases. The axial component of the current flow interacts with the azimuthal magnetic field to produce the Lorentz pumping force density, which pushes plasma away from the anode, toward the thruster centerline. What previous studies do not show, however, is the time evolution of the axial current—in particular, how long it takes to establish a significant axial current, and how, if at all, this influences the

voltage.

To answer this question, we use the Rogowski coil described in the next section to measure the axial current attaching near the tip of the cathode. The 45 mm diameter coil was positioned at the downstream tip of the cathode, coaxial with the thruster axis of symmetry.

## B.1 Rogowski Coil

It was illuminating to measure the amount of current attaching near the tip of the cathode. The electrons that carry this current swing downstream of the cathode tip, and then back up to attach near the outer edge of the anode, as shown by the current patterns measured by previous researchers [8, 9, 30]. These measurements also show that the amount of current that attaches near the cathode tip is a good indicator of the extent to which the overall thruster current has been turned downstream by large electron Hall parameters in the thruster plasma. To measure this current, a Rogowski coil was fashioned after the work of Wright [65]. (For more information on the theory, design, and calibration of Rogowski coils, see Appendix A.) The coil of #32 magnet wire was wound around #22 PVC-insulated wire; a uniform coil spacing was maintained by first wrapping the wire around a #2 machine screw, and then transferring the coil to the #22 wire. Heating the PVC insulation, then allowing it to cool, embedded the surrounding coil into the insulation to keep the coil from slipping and deforming. The #22 wire was attached to one end of the coil, and used as the return lead through the center of the coil. The signal was brought out of the vacuum chamber on twisted/shielded pair, which was then terminated in an active balanced/unbalanced converter to eliminate common-mode noise picked up by the close proximity of the coil to the discharge. The entire coil was inserted into a glass tube bent into a circle 45 mm in diameter to maintain the shape of the coil and



insulate it from the discharge.

The coil was then positioned coaxially with the cathode, at the axial location of the cathode tip, so that it measured only the axial current that attached near the cathode tip. The recorded signal was integrated digitally in post-processing.

## B.2 Typical Results

Examples of the current measured by the Rogowski coil are shown in Fig. B.1, along with the current and voltage traces for the same firing. The most obvious feature of these figures is the delay between the initiation of the thruster current, and a significant rise in the current attaching to the cathode tip, enclosed by the Rogowski coil. This delay, present at all thruster currents, indicates that several hundred  $\mu\text{s}$  are required for the emission processes of the cathode, and the pinching contraction of the plasma, to establish a steady axial current. High-speed video of cathode spot formation and movement during firing corroborates the finding that the same delay exists between switching the thruster current and the establishment of steady cathode emission.

At low values of  $J^2/\dot{m}$ , the delay between the thruster current initiation and the axial current establishment is irrelevant to the shape of the voltage: the voltage remains a steady value even as the current distribution changes. On the other hand, at high values of  $J^2/\dot{m}$ , at which voltage hash is present, the evolution of the voltage closely matches the evolution of the axial current. Unlike in the low  $J^2/\dot{m}$  case, the voltage does not immediately assume its quasi-steady value, but rises from its breakdown minimum over the course of several hundred  $\mu\text{s}$ . The rise occurs concurrently with the the rise of the cathode tip current, and the voltage hash does not begin until the tip current has risen to near its final value.

The conclusions drawn from these observations are consistent with the hypothesis

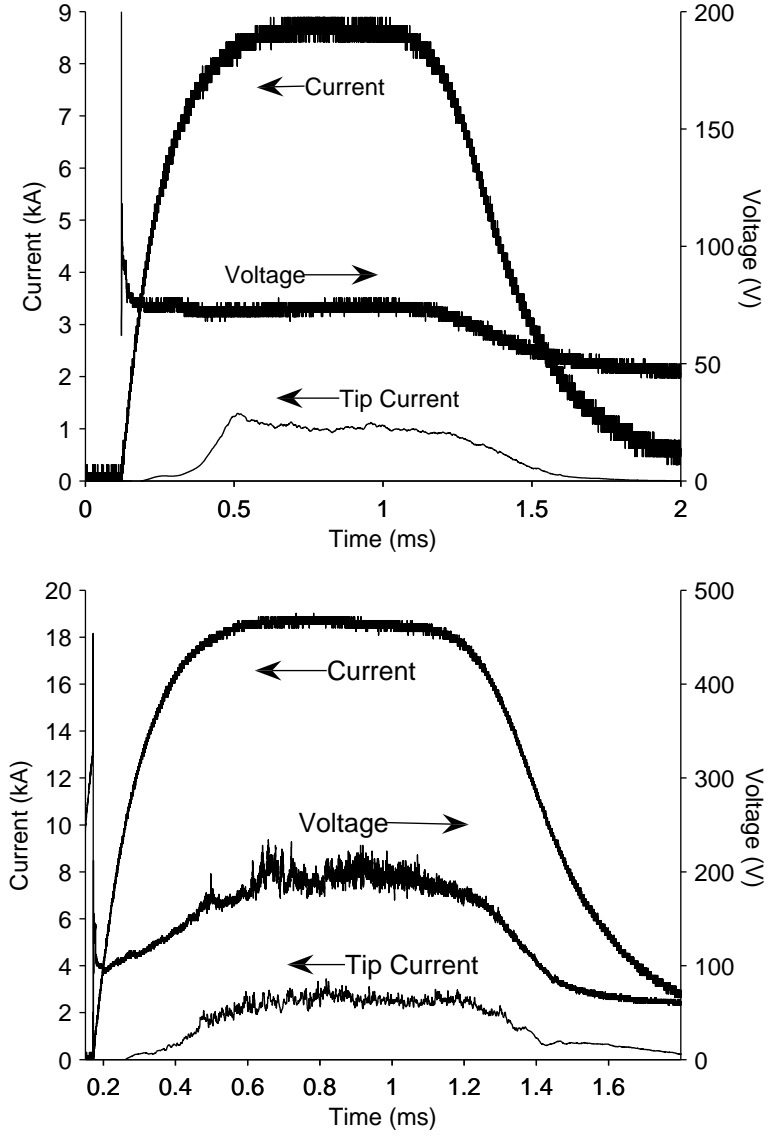


Figure B.1: The thruster total current, terminal voltage, and axial current from the cathode tip measured by a Rogowski coil, at two values of  $J^2/\dot{m}$ : (top)  $14 \text{ kA}^2\text{-s/g}$ , and (bottom)  $75 \text{ kA}^2\text{-s/g}$ .

that voltage hash is a result of anode starvation. The presence of larger axial currents at high  $J^2/\dot{m}$  creates a large Lorentz pumping force that forces plasma radially inward, away from the anode. The delay time in establishing an axial current indicates there is a similar delay in establishing the resulting pumping force. If voltage hash is a result of the low near-anode plasma density that this causes, then the beginning of voltage hash should be similarly delayed until the axial current is established. The observations in this section do in fact show this delay.

It was not possible to collect information on the time evolution of the axial current at even higher values of  $J^2/\dot{m}$ ; at these currents, the discharge becomes exceedingly noisy, overwhelming the otherwise excellent common-mode noise rejection built into the Rogowski coil circuitry. We cannot, therefore, directly comment on the behavior of the cathode tip current when the voltage hash becomes very large.

## Appendix C

# Relationship Between Plasma Density Fluctuations and Voltage Hash

In his study of near-anode plasma density, Diamant [14] observed that the time-resolved density showed spikes rising from the baseline density as  $J^2/\dot{m}$  rose above onset, and attributed this behavior to anode spots. In our own random model of anode spots, in Chapter 3, we have assumed that when a spot ignites, it does so quickly, so that the voltage falls rapidly. Diamant's observation is consistent with our assumption of anode spot behavior if the rapid energy input to the anode from a spot causes a burst of anode material to evolve from the anode. Because Diamant did not compare the time-resolved density measurements with the time-resolved voltage hash, it has been unclear whether this was the case. In this appendix, we present measurements of the plasma density that show that the evolution of anode material does coincide with the rapid drop of the voltage during hash, providing further evidence that the anode spot model that we have used is consistent with our knowledge of onset physics.

## C.1 Langmuir Probe Apparatus

We measured the plasma density using a double Langmuir probe made of two 0.13 mm diameter tungsten wires encased in glass and ceramic to shield all but the exposed probe tip, which was 1 mm long, from the discharge. The wires were crimped to the two leads of a twisted/shielded pair cable, which were connected to an Agilent E3640 DC power supply. The bias between probe wires was kept constant at 40 V, which is sufficient to drive the probe into the ion saturation region of the probe characteristic. We measured the current through the probe wires using a Tektronix CT-2 current transformer, which has a flat frequency response from 10 kHz to 200 MHz. The measurements therefore represent the fluctuations in the plasma density, and not the quasi-steady plasma density, information about which is available in the work of Diamant et. al. [14, 19] The signal from the current probe was reduced to the measurement of ion density by the standard formula for ion saturation current density,

$$i_+ \approx en_i \sqrt{\frac{kT_e}{M_i}}, \quad (\text{C.1})$$

where  $i_+$  is the ion saturation current density,  $n_i$  the ion density,  $T_e$  the electron temperature, and  $M_i$  the ion mass. The conditions for which this formula is appropriate were met in this experiment.

We took all the density fluctuation measurements discussed in this paper at one location,  $\sim 10$  mm downstream of the copper anode, and  $\sim 7$  mm radially outward from the anode inner radius ( $r_a$  in Fig. 2.1).

## C.2 Simultaneous Density Fluctuation and Voltage Hash Observations

The ion density, like the voltage hash, is a random fluctuation. Except for a single range of  $J^2/\dot{m}$  values, the density fluctuation shows no temporal correlation or definite relationship to the voltage fluctuation. The range of  $J^2/\dot{m}$  values for which it does is the range over which the statistics of the voltage hash are strongly non-Gaussian.

In this range, the ion density shows a time variation that is clearly correlated to the behavior of the thruster voltage. This can be seen in Fig. C.1, from which it is apparent that spikes in plasma density occur, generally, concurrently with bursts of voltage hash. In the expanded view, we see that spikes in the plasma density occur after a quick fall in the voltage. The density spikes, with remarkable consistency, occur between  $0.5 \mu\text{s}$  and  $1.5 \mu\text{s}$  after the beginning of the corresponding voltage drop.

That the density fluctuation is a series of spikes indicates that the plasma density at the probe location is executing a series of sharp rises and slightly more gradual falls. This sort of shape in the density transient is what might be expected from the quick release of vapor into the plasma—i.e., the rapid formation of an anode spot. Evaporated anode vapor will expand out from its point of origin; when it reaches the probe location, the probe will register a fast rise in density, which will decay quickly as the vapor from the quick release at the spot passes by. Based on the location of the probe, and the delay between the beginning of the voltage drop and the rise of the corresponding density spike—a delay on the order of  $1 \mu\text{s}$ —the released vapor should have a velocity on the order of  $10^4 \text{ m/s}$ . This is much faster than the thermal velocity of copper atoms at the copper melting temperature (about  $400 \text{ m/s}$ ), but on the same order as the plume flow velocity at these conditions. This may indicate that ionized anode vapor, which is subject to the Lorentz  $\mathbf{j} \times \mathbf{B}$  body

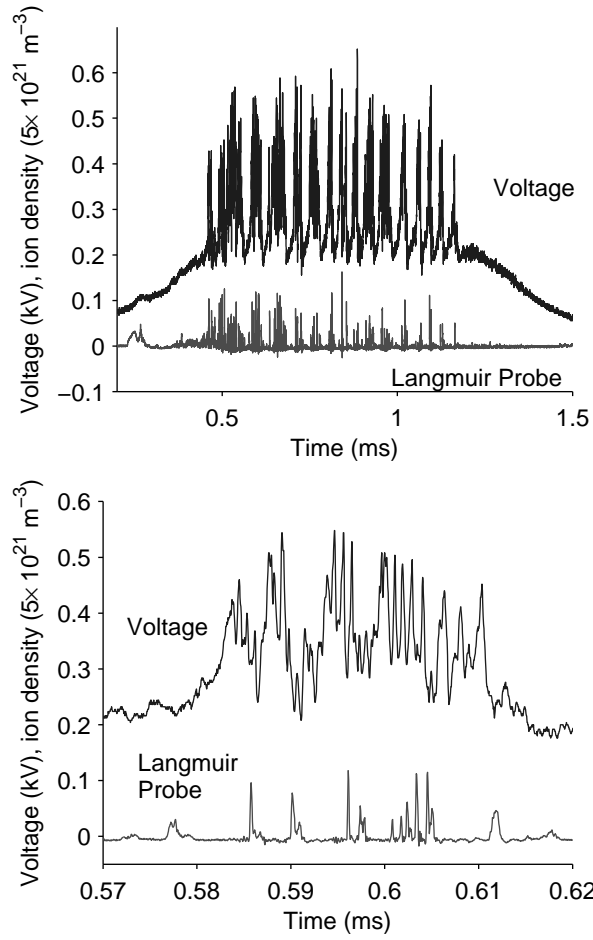


Figure C.1: An example voltage and Langmuir probe trace, for  $J^2/\dot{m} = 100 \text{ kA}^2\text{-g/s}$ . (Top) The whole duration of a quasi-steady pulse, showing the appearance of density spikes contemporary with the voltage jumps. (Bottom) A  $50 \mu\text{s}$  section of the same trace, showing the density spikes at many, but not all, of the voltage jump locations.

force (where  $\mathbf{j}$  is the current density and  $\mathbf{B}$  is the magnetic field), is quickly accelerated to the plume velocity. That roughly half of the voltage drops are followed by a density spike—measured at a single location with the Langmuir probe—indicates that spots may be formed at multiple locations on the anode during a single drop. Otherwise, since we expect only to see density spikes when a spot forms near the probe location—and since the anode is large with respect to the probe size—we should see a voltage spike followed by a density spike much less often.

It is easy to see, following this reasoning, why we do not see clear temporal correlations at  $J^2/\dot{m}$  values lower and higher than those which we have just discussed. Because at these  $J^2/\dot{m}$  the voltage events overlap significantly—hence the nearly-Gaussian statistics—any anode material released by the formation of a spot will join that released by many other spots that occur at nearly the same time. The density signal is therefore the superposition of the signals generated by a series of randomly-spaced events—and is itself a random signal.



# Appendix D

## Further Literature Review of Onset Phenomena

In Chapter 1, we summarized the key findings regarding the  $J^2/\dot{m}$  dependence of the onset phenomenon, the behavior of the thruster voltage and erosion at large  $J^2/\dot{m}$ , and the theories that have been developed to explain these observations. In this chapter we expound on the specific studies whose findings we condensed into the points in Chapter 1. Rather than proceed chronologically, we will break up the review into three parts corresponding to the summary in Chapter 1: dependence of  $(J^2/\dot{m})^*$  on thruster design; voltage noise and component erosion; and theoretical work predicting  $(J^2/\dot{m})^*$ .

### D.1 Thruster design impact on $(J^2/\dot{m})^*$

Boyle et. al. [9] are the first to give the name “onset” to this phenomenon. They showed the geometric dependence of  $(J^2/\dot{m})^*$  to be more complicated than a simple dependence on  $r_a/r_c$ , as Malliaris had tabulated; they found the critical parameter to be raised when the radial location of propellant injection in the backplate was moved outward toward the anode, and when the cathode was lengthened. (These

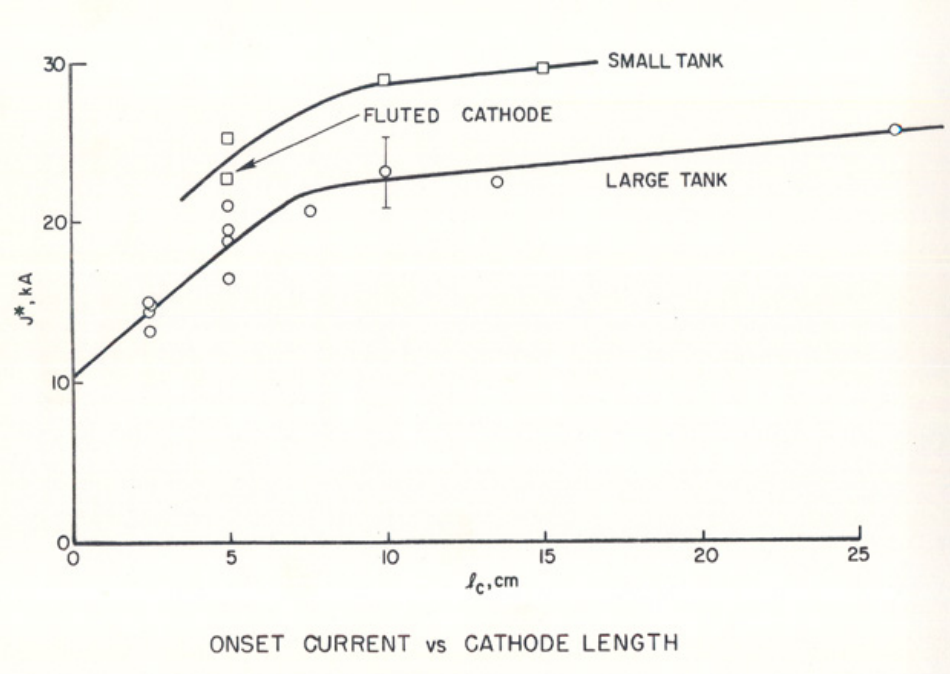


Figure D.1: Asymptote of  $J^*$  with increasing cathode length (after [8]).

authors in fact argued that it was the increased cathode surface area that was the important feature of lengthening the cathode; it was left to Rudolph [8] to show that this was not the case, but that the length itself of the cathode was important. Rudolph demonstrated that a limiting value of the critical parameter is asymptotically reached as the cathode is lengthened beyond the exit of the thruster (see Fig. D.1.) It was Villani [66] who showed that the longer cathodes promoted a more radial current pattern in the discharge volume, which would serve to decrease the radial pumping force and so delay anode starvation. Experiments by Andrenucci et. al. [67] show similar results.

Each of these findings supports the following points made in Chapter 1.

- *Increasing the particle density of the propellant increases  $(J^2/\dot{m})^*$ .* Propellants with lower atomic weights reach onset at higher  $J^2/\dot{m}$ , because for the same  $\dot{m}$  the particle density is greater. The dependence of  $(J^2/\dot{m})^*$  on the propellant is strictly  $\sim M^{-1/2}$ . [7].

- *Thruster geometry alterations that increase the particle density at large radii (near the anode) increase  $(J^2/\dot{m})^*$ .* These include, keeping all other parameters constant: lowering the radii ratio of anode to cathode  $r_a/r_c$  (smaller thruster volume increases particle density) [7]; lengthening the cathode (discouraging Lorentz body forces that move plasma away from the anode) [8]; and injecting propellant at a radius similar to the anode radius (forcing more propellant near the anode initially) [9].

## D.2 Thruster behavior beyond $(J^2/\dot{m})^*$

Vainberg et. al. [48], by taking direct probe measurements of the anode fall voltage over the full operating range of a lithium-fed steady-state MPDT, showed that the anode fall takes on small negative (electron-repelling) values at low-current operation, but rises quickly to large positive values at the same current at which the terminal voltage transitions from a weakly-rising function of current to a strongly-rising function of the same. They note also that oscillations are excited in both the probe and the terminal voltage at this current. The voltage-current characteristic and the anode fall rise at the critical current are shown in parts (a) and (e) of Fig. D.2, reproduced from [48]. Hugel, in a later paper, has also noted this occurrence [68]. The rising anode fall potential leads to greater power input to the anode, which in turn promotes anode damage.

Rudolph [20] has shown that the magnitude of the voltage noise (which he refers to as “hash”) rises as  $(J^2/\dot{m})^*$  is reached, and reaches a maximum at some current above onset; the magnitude of the voltage hash then decreases to a steady value for higher currents (behavior seen in Fig. 1.3). Spectroscopic studies by Ho [13] have shown that the major erosion products in an MPDT operating above onset come from erosion of the anode, and that this erosion becomes more pronounced

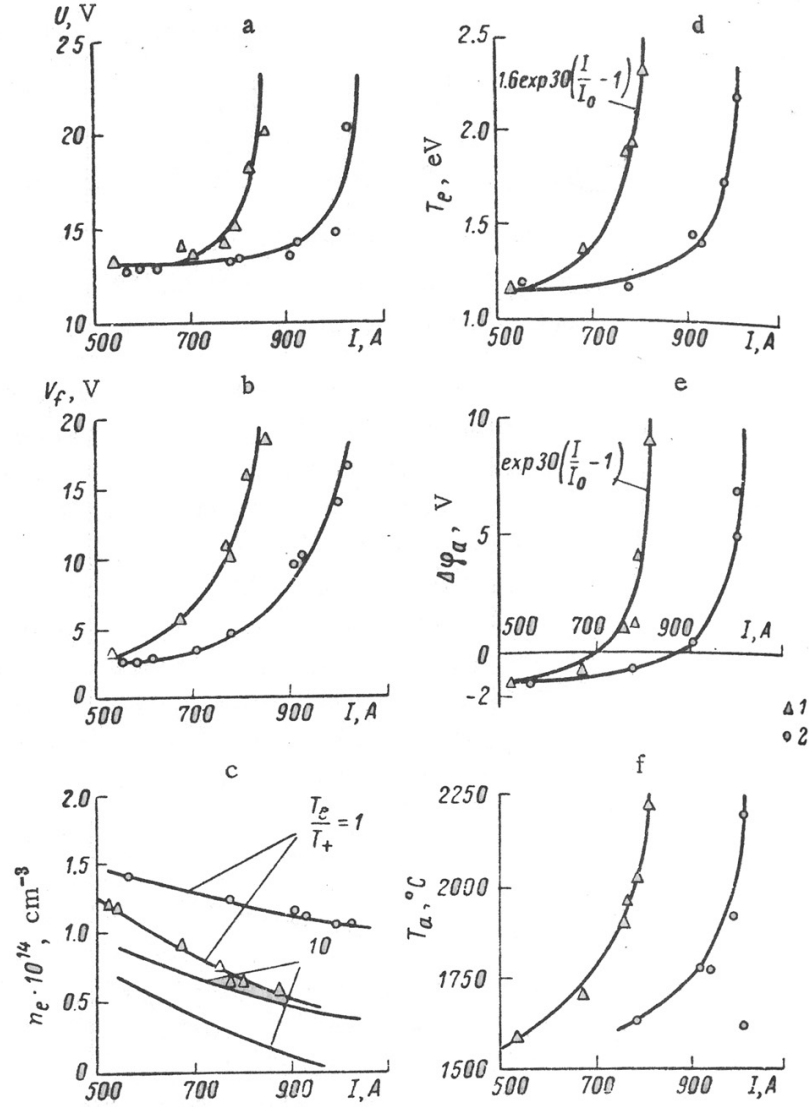


FIG. 3. Experimental results (averaged over the scatter in values). 1) The rate of expenditure of the working medium is  $\dot{m} = 0.006$ ; 2)  $0.010$  g/sec.

Figure D.2: Variation of measured near-anode parameters as the critical current is passed. (a) voltage-current characteristic; (b) floating potentials near the anode; (c) near-anode plasma density; (d) electron temperature at same location; (e) anode fall potential; (f) anode temperature. After Vainberg et. al. [48].

as the current is increased. Though Rudolph observed the magnitude of the voltage hash to decrease above a certain current, Ho showed that the amount of anode erosion continued to rise as the current increased—indicating that the erosion of the anode is responsible for damping the phenomena that gave rise to the oscillations.

Kuriki and Iida [11] observed weak peaks in the power spectra of both the voltage hash fluctuations and fluctuations in the total luminosity of the thruster arc above onset. The frequencies present in the two signals, which are not equal to one another, rise with  $J^2/\dot{m}$  over the range 100–400 kHz. They observed different frequencies for hydrogen and argon propellant. These authors did not identify the sources of these peaks, nor did they comment on the shape of their spectra, which, aside from the weak peaks, falls off with frequency much as those in Chapter 3 of this dissertation do. This paper by Kuriki and Iida is notable as the first, and to our knowledge, the only other attempt to analyze the power spectrum of the hash aside from the work presented in this dissertation. Tilley et. al. [38] conclude that the work of Kuriki and Iida is “inconclusive”, and show that a number of instabilities may exist within the thruster. We have addressed, in Chapter 3, the possibility that these instabilities may manifest themselves in the thruster voltage; we have also, in Chapter 2, shown that the power circuit may introduce harmonic structure into the voltage hash power spectrum. Without specific details of Kuriki and Iida’s thruster power circuit, and without any published follow-up work, it is impossible to conclusively interpret their data in light of this dissertation’s findings.

Hügel [10, 69] found using high-speed photography that the arc attachment at the anode occurs in a diffuse manner below  $(J^2/\dot{m})^*$ , but bright spots appeared at the anode above the critical parameter. Anode material was melted where these spots had been present. The thruster voltage became noisy at the same operating parameter as that for which the spots appeared; furthermore, the voltage noise (which had an apparent dominant frequency component at 230 kHz) was accompanied by

coherent fluctuations in the voltage between the anode and a Langmuir probe placed close to the anode—indicating the near-anode region to be the source of the noisy voltage. While Hugel showed that, statistically, anode spots were more likely to form during periods when the voltage hash was peaking, he stopped short of showing a causality between the two.

Vainberg [48] noted the collapse of a diffuse arc attachment at the anode into attachment through anode spots as the critical parameter is reached, and associated this process with evaporation at the anode.

Based upon observations of the damaged anode of the FSBT, Diamant [14, 19] has shown that MPDTs are subject to the formation of anode spots when operating above onset. He demonstrates that the  $J^2/\dot{m}$  value at which spot marks appear on the anode is dependent on surface condition; sufficiently rough anodes transition to spot mode at lower currents than smoother anodes. He identifies the parameter that triggers the transition from diffuse anode current collection to spot mode as  $j/j_{th}$ , the ratio of the near-anode current density to the largest possible current density that can be provided by the thermal motion of electrons. For  $j/j_{th} < 1$ , the current collection at the anode is diffuse and no anode spots form; for ratios greater than one, anode spots form (on smooth anodes; on rough anodes, the transition to spot mode occurs at values of current nearly half as large as that for smooth anodes). Further increases in the thruster current bring the ratio below one again, as the anode evaporation caused by the spots leads to a resurgence in the near-anode plasma density.

In combination, the work of Hugel and Diamant in particular provides a clear picture of the triggers that cause onset phenomena. In few words, the anode enters saturation when the current is increased and the near anode density drops such that  $j/j_{th} > 1$ ; this triggers the formation of anode spots, which solve the saturation crisis by providing preferential current channels to the anode. In the process additional plasma density is generated via anode erosion. The dynamics of spot formation

and extinction give rise to fluctuations in the arc voltage and plume luminosity. To summarize the review of this section into the points made in Chapter 1:

- *With rising  $J^2/\dot{m}$ , voltage noise (hash) magnitude increases slowly at first, leaps to large values, then falls again.* [8] The characteristic frequency of the hash is frequently noted as hundreds of kHz [10–12].
- *With rising  $J^2/\dot{m}$ , the erosion of all thruster components increases, but the erosion of the anode rises dramatically with respect to the others.* The anode erosion rises steadily with increasing current, not displaying the rise-and-fall of the voltage hash. [13]
- *“Spots” appear on the anode above  $(J^2/\dot{m})^*$ , apparently conducting significant current and melting the anode at discrete sites.* Evidence for anode spots comes from both high-speed photography, which captures spots when they occur [10], and observations of the anode after firing, when the damage is visible [14].

This tidy picture is disrupted by the formation of anode spots below  $(J^2/\dot{m})^*$  on rough anodes [14]; but this can be explained by our observation, in Chapter 4, that spots form to some extent at all  $J^2/\dot{m}$  values, but visible evidence of the spots, on which Diamant based his interpretations, only appears when the anode is susceptible to damage, as for less refractory anodes. Rough anodes, with their whisker-like protrusions, are more likely to reach localized higher temperatures, and so are more likely to show evidence of spotting damage than smooth anodes.

### D.3 Theoretical Prediction of $(J^2/\dot{m})^*$

Attempts to explain the onset phenomena generally fall into two categories: anode (sheath) starvation, and plasma instability. These two are in fact not mutually

exclusive, as some authors would argue that anode starvation acts as a trigger for plasma instability.

The anode starvation thesis is as follows. The Lorentz force density, given in Eq. (1.3), has both an axial component and a radial component, as can be seen in Fig. (1.1). The radial force component pushes the propellant toward the thruster centerline, and away from the anode. This effect becomes more pronounced at higher currents, as the current density  $\mathbf{j}$  and the magnetic field  $\mathbf{B}$  both depend on the current. As the near-anode plasma density drops and the current rises, the anode enters sheath-limited current saturation (analogous to the saturation of a Langmuir probe at large positive potentials). In this view, the effects of onset—voltage hash and damage to the anode—represent the arc’s response to current saturation.

Anode starvation was not originally used within the framework of onset: Oberth and Jahn [70] invoked the idea to explain the growth of electric fields around the anode in the high-current MPDT arc. Hügel [10] used anode starvation to postulate that above onset the near-anode electric field grows to such a value that “flash-overs” occur between the anode and the core of the plasma that has been pinched toward the cathode. He suggests that the current pattern, affected by the formation of this “spot”, redistributes to temporarily solve the anode starvation; however, once the event is finished, the starvation returns and the spot must form again, in repetitive fashion.

This line of reasoning was followed in the former Soviet Union as well. Baksht et. al. [15] similarly argue that the MPDT anode enters starvation when the pinch effect causes the thermal electron current collected by the anode to drop below the thruster current. This leads to a reversal in the sign of the anode sheath (from negative, or electron repelling, to positive). The reversal of the sheath is the trigger for onset phenomena. Baksht derives an expression for the limiting parameter  $J^2/\dot{m}$ , and shows that it is constant for a constant propellant and thruster geometry, and its



dependence on the propellant species is as  $\sim M^{-1/2}$ —each dependence the same as that observed experimentally by Malliaris et. al. [7]. With a similar logic, Korsun [71] argues that the pinched MPDT plasma is contained within a column whose boundary contracts with increasing current; when the column boundary no longer contacts the anode, no further current can flow and the limit is reached. However, Korsun’s derived value for the limiting  $J^2/\dot{m}$  is dependent upon the propellant mass as  $\sim M^{-3/4}$ ; and while conceptually, one might expect that as the plasma column pulls away from the anode, an electron-attracting anode sheath would develop, Korsun’s model does not address this. Nevertheless, numerical simulations by Sankaran [72] show that the concept of a moving plasma column boundary is a useful simplification of the pinching phenomenon, if not a fully satisfactory explanation for the onset phenomenon.

The arguments that onset phenomena are the result of plasma instabilities rely on identifying conditions favorable to the development of certain instabilities or observing that the frequency spectrum of the observed voltage hash is similar to that of certain known instabilities. Shubin [17] argues that low densities and high electric field near the anode cause an increase in the relative drift velocity of electrons with respect to ions, which may drive certain drift instabilities. He derives a criterion for the limiting  $J^2/\dot{m}$ , and shows it to be equal within a constant factor to that of Baksht [15]. (In the past, much has been made of this agreement, arguing that underlying understanding is lacking if two theoretical avenues lead to equivalent results [48]. It is not surprising, however, that the two produce a similar result: though Shubin wishes to invoke instabilities, his criterion for the stability of his model plasma is that the fluid plasma boundary should not have pulled away from the anode. In this sense, Shubin’s argument is not much different than that of Korsun or Baksht.) Kuriki and Iida [11] point out that frequencies similar to those observed in the voltage hash are present in certain ionization instabilities. Wagner et. al. [16, 73] show that macroscopic space-charge instabilities can exist in MPDTs, and

can be excited by large electron drift velocities and density gradients, which would appear in the MPDT at high  $J^2/\dot{m}$ . Bonomo et. al. [74], Zuin et. al. [29, 75, 76], and Paganucci et. al. [77] have observed a helical kink instability present in the applied-field MPDT using ultraviolet tomography, and found favorable comparison with the MHD instabilities normally found in screw pinches—in particular, they found that the Kruskal-Shafranov limit effectively divided their own stable and unstable operation. They suggest that this kink instability is the driver behind onset phenomena. However, the extension of their work to MPDTs with no applied field—such as our own—is not straightforward, as the Kruskal-Shafranov stability limit relies on the presence of an applied axial field. They suggest that symmetry breaking at high currents may create axial magnetic fields, and so create conditions in which the kink instability may exist; they have not, however, shown that this is the case, and it remains that their work is more applicable to applied-field than to self-field thrusters.

The weakness in both lines of argument—anode starvation or plasma instability—is that while the authors have paid much attention to deriving a limiting value of current or of  $J^2/\dot{m}$ , they have in general paid little attention to the problem of what drives the phenomena observed after that limit. Anode starvation theory does not on its own explain the fluctuations in thruster voltage or plume luminosity, nor the appearance or nature of damage to the anode. Similarly, the mechanism by which plasma instabilities would contribute to voltage fluctuations or anode damage is generally left as unspecified “turbulence”.

An evaluation of the relevance of these theories to the experimental characterization of onset phenomena was given in Chapter 1. Their greatest limitation is that neither can predict the behavior of the MPDT once  $(J^2/\dot{m})^*$  is exceeded—not the existence, nature, or behavior of the voltage hash, the erosion of the anode, or the spotty current attachment. In that sense, the existing theoretical work is not helpful in our study of hash and erosion, but we have included these models in our review for completeness.

## D.4 Other Onset Theories

Besides the onset theories that were reviewed in the last section, a number of additional theories exists in the literature. These theories are generally lacking in one way or another, and we have therefore not addressed them within the scope of this work. For completeness, however, in this section we provide a short description of two of these theories, along with an explanation for why they were left on the periphery of this work.

### D.4.1 Back-EMF Onset

Lawless and Subramaniam [78–80] have suggested that it is possible for the plasma in an accelerator to flow quickly enough to impede current from flowing between the electrodes. A plasma flowing across a magnetic field gives rise to a voltage gradient given by the vector product of the flow velocity and the magnetic field strength,  $\mathbf{u} \times \mathbf{B}$ . This voltage gradient, known as the back-EMF, can be the largest source of voltage drop in a plasma accelerator when both  $\mathbf{u}$  and  $\mathbf{B}$  are large, e.g., when large currents are driven through a self-field MPDT. These authors have argued that, in the event that the inductive voltage drop associated with the back-EMF becomes equivalent to the thruster driving voltage, current will no longer be able to flow between the electrodes and a conduction crisis will ensue.

The fundamental difficulty with this line of reasoning is that, as seen in this work, MPDTs are not voltage-driven devices: they are current-driven devices. An MPDT power supply (such as the PFN used in this study) is stiff, meaning that it has a sufficiently large inductance that voltage variations in the thruster will be met with only small variations in the current through the thruster. In any study cited in this work, and in this work itself, the current does not experience a cutoff when onset is reached: rather, onset manifests itself as a voltage phenomenon, because

the voltage is allowed to assume whatever value is necessary for the passage of the imposed current.

While the cessation of current flow due to back-EMF is important for voltage-driven accelerators such as MHD channels, this concept is not important for the study of onset in MPDTs, and has therefore been kept on the periphery of the study.

#### D.4.2 Unstable Current Channels

Schrade et. al. [81,82] have suggested that onset is a result of a macroscopic instability in a current-carrying channel originating at the tip of the cathode. These authors suggest that at low-current operation, the current-carrying channel is able to conduct electrons to the anode in an axi-symmetric fashion, so that the discharge as a whole is symmetric and stable. On the other hand, at high currents the constriction of the channel causes it to be unstable to small deflections, so that it will bend and cause current to attach asymmetrically to the anode. The asymmetry will then cause the attachment location to rotate about the anode surface.

While the macroscopic channel instability described may exist when a current-carrying channel such as described exists, this condition does not occur in MPDTs in the manner described. Unlike the MPDTs at U. Stuttgart, which inspired this theory, not all MPDTs force the plasma to flow through a constricted nozzle in order to bridge the cathode and anode: that is, not all MPDTs force the current to constrict into a single channel. Perhaps the largest problem with this theory can be seen in some of the photographic documentation in this thesis, and in that of Hoskins [83]: the FSBT discharge becomes *increasingly* symmetric with increasing current, even after onset is reached. Small asymmetries exist in the form of spots or flares on the anode surface; but in no way has the discharge collapsed into a single asymmetric channel the way that the theory of Schrade suggests. Nevertheless, we should point out that Schrade's theory may be relevant to certain MPDT configurations, even if

it does not address the fundamental origin of onset in the most general sense.

Because this theory runs counter to our observations, we leave it on the periphery of our investigation.

# Bibliography

- [1] J. Buursink, “Launch cost reduction by the reuse of the core stage of ariane 5,” *Journal of Reducing Space Mission Cost*, vol. 1, pp. 209–223, September 1998.
- [2] J. R. Wertz, ed., *Space Mission Analysis and Design*. Microcosm Press, 3rd ed., 1999.
- [3] J. E. Foster, T. Haag, M. Patterson, G. J. Williams, J. S. Sovey, C. Carpenter, H. Kamhawi, S. Malone, and F. Elliot, “The high-power electric propulsion (hipec) ion thruster,” *AIAA Joint Propulsion Conference*, 2004.
- [4] R. G. Jahn, *Physics of Electric Propulsion*. McGraw-Hill, 1968.
- [5] E. Choueiri and J. Ziemer, “Quasi-steady magnetoplasmadynamic thruster performance database,” *Journal of Propulsion and Power*, vol. 17, pp. 520–529, Sept/Oct 2001.
- [6] A. C. Ducati, G. M. Giannini, and E. Muehlberger, “Recent progress in high specific impulse thermo-ionic acceleration,” *AIAA 2nd Aerospace Sciences Meeting*, January 1965.
- [7] A. Malliaris, R. John, R. Garrison, and D. Libby, “Performance of quasi-steady MPD thrusters at high powers,” *AIAA Journal*, vol. 10, pp. 121–122, February 1972.

- [8] L. Rudolph, *The MPD Thruster Onset Current Performance Limitation*. PhD thesis, Princeton University, 1980.
- [9] M. J. Boyle, K. E. Clark, and R. G. Jahn, “Flowfield characteristics and performance limitations of quasi-steady magnetoplasmadynamic accelerators,” *AIAA Journal*, vol. 14, pp. 955–962, July 1976.
- [10] H. Hugel, “Flow rate limitations in the self-field accelerator,” *AIAA 10th Electric Propulsion Conference*, vol. AIAA 73-1094, 1973.
- [11] K. Kuriki and H. Iida, “Spectrum analysis of instabilities in MPD arcjet,” *International Electric Propulsion Conference*, no. IEPC84-28, 1984.
- [12] H. L. Kurtz, M. Auweter-Kurtz, W. D. Merke, and H. O. Schrade, “Experimental MPD thruster investigations,” *19th International Electric Propulsion Conference*, no. AIAA-87-1019, 1987.
- [13] D. Ho, “Erosion studies in an MPD thruster,” Master’s thesis, Princeton University, 1981.
- [14] K. D. Diamant, *The Anode Fall in a High Power Pulsed MPD Thruster*. PhD thesis, Princeton University, 1996.
- [15] F. G. Baksht, B. Y. Moizhes, and A. B. Rybakov, “Critical regime of a plasma accelerator,” *Soviet Physics Technical Physics*, vol. 18, p. 1613, June 1974.
- [16] H. P. Wagner, H. J. Kaeppler, and M. Auweter-Kurtz, “Instabilities in MPD thruster flows: 1. space charge instabilities in unbounded and inhomogeneous plasmas,” *Journal of Physics D*, vol. 31, p. 519, 1998.
- [17] A. Shubin, “Dynamic nature of critical regimes in steady-state high-current plasma accelerators,” *Soviet Journal of Plasma Physics*, vol. 2, pp. 18–21, January/February 1976.

- [18] L. Uribarri and E. Y. Choueiri, “Relationship Between Anode Spots and Onset Voltage Hash in Quasi-Steady Magnetoplasdynamic Thrusters,” *30th International Electric Propulsion Conference*, no. IEPC-2007-363, 2007.
- [19] K. D. Diamant, E. Y. Choueiri, and R. G. Jahn, “Spot mode transition and the anode fall of pulsed magnetoplasdynamic thrusters,” *Journal of Propulsion and Power*, vol. 14, pp. 1036–1042, November-December 1998.
- [20] L. Rudolph, R. Jahn, K. Clark, and W. von Jaskowsky, “Onset Phenomena in Self-Field MPD Arcjets,” *13th International Electric Propulsion Conference*, no. IEPC78-653, 1978.
- [21] R. L. Burton, K. E. Clark, and R. G. Jahn, “Measured performance of a multi-megawatt MPD thruster,” *Journal of Spacecraft and Rockets*, vol. 20, no. 3, pp. 299–304, 1983.
- [22] V. A. Nemchinsky and M. S. Showalter, “Cathode erosion in high-current high-pressure arc,” *Journal of Physics D: Applied Physics*, vol. 36, no. 6, pp. 704–712, 2003.
- [23] *The Industrial Graphite Engineering Handbook*. Union Carbide Corporation, 1969.
- [24] W. Gale and T. Totemeier, eds., *Smithell’s Metals Reference Book*. Elsevier, 8 ed., 2004.
- [25] K. E. Clark and R. G. Jahn, “Quasi-steady plasma acceleration,” *AIAA Journal*, vol. 8, p. 216, February 1970.
- [26] L. Uribarri and E. Y. Choueiri, “Corruption of pulsed electric thruster voltage fluctuation measurements by transmission line resonances,” *Journal of Propulsion and Power*, vol. 24, no. 3, p. 637, 2008.



- [27] H. H. Skilling, *Electric Transmission Lines*. McGraw-Hill, 1st ed., 1951.
- [28] National Institute of Standards and Technology, “Atomic spectra database.” Internet Database, 2007.  
<http://physics.nist.gov/PhysRefData/ASD/index.html>.
- [29] M. Zuin, R. Cavazzana, E. Martines, G. Serianni, V. Antoni, M. Bagatin, M. Andrenucci, F. Paganucci, and P. Rossetti, “Critical regimes and magnetohydrodynamic instabilities in a magneto-plasma-dynamic thruster,” *Physics of Plasmas*, vol. 11, p. 4761, October 2004.
- [30] J. W. Barnett and R. G. Jahn, “Onset Phenomena in MPD Thrusters,” *AIAA 18th International Electric Propulsion Conference*, vol. AIAA 85-2038, 1985.
- [31] N. A. Neremina and B. N. Klyarfel’d, “Anode region in a low-pressure gas discharge: II. role of plasma electron temperature, anode surface temperature, and anode molecular accommodation coefficient,” *Soviet Physics Technical Physics*, vol. 4, p. 13, 1959.
- [32] B. N. Klyarfel’d and N. A. Neretina, “Anode region in a low-pressure gas discharge: III. production of additional plasma at the anode (anode spots),” *Soviet Physics Technical Physics*, vol. 5, p. 169, 1960.
- [33] B. Klyarfel’d, N. Neretina, and N. Druzhinina, “Anode region in a low-pressure gas discharge: IV. anode phenomena in a high-current mercury discharge (survey),” *Soviet Physics Technical Physics*, vol. 17, pp. 997–1005, December 1972.
- [34] B. N. Klyarfel’d and N. A. Neretina, “Anode region in a low-pressure gas discharge: I. effect of anode shape on sign and magnitude of the anode fall,” *Soviet Physics Technical Physics*, vol. 3, p. 271, 1958.

- [35] L. Harris, “Small-scale anode activity in vacuum arcs,” *IEEE Transactions on Plasma Science*, vol. PS-10, pp. 173–180, September 1982.
- [36] S. N. Nazarov, V. I. Rakhovsky, and V. G. Zhurbenko, “Voltage drop over a vacuum arc and the cathode-spot brightness,” *IEEE Transactions on Plasma Science*, vol. 18, no. 3, p. 682, 1990.
- [37] J. S. Bendat and A. G. Piersol, *Random Data: Analysis and Measurement Procedures*. Wiley, Third.
- [38] D. L. Tilley, E. Y. Choueiri, A. J. Kelley, and R. G. Jahn, “Microinstabilities in a 10-kilowatt self-field magnetoplasma dynamic thruster,” *Journal of Propulsion and Power*, vol. 12, no. 2, p. 381, 1996.
- [39] P. Manneville, “Intermittency, self-similarity and  $1/f$  spectrum in dissipative dynamical systems,” *J. Physique*, vol. 41, pp. 1235–1243, 1980.
- [40] H. Schuster and W. Just, *Deterministic Chaos*. Wiley-VCH, 2006.
- [41] Y. P. Raizer, *Gas Discharge Physics*. Springer, 2001.
- [42] L. Uribarri and E. Y. Choueiri, “The onset of voltage hash and its relationship to anode spots in magnetoplasma dynamic thrusters,” *29th International Electric Propulsion Conference*, no. IEPC-2005-084, 2005.
- [43] M. M. Milanese, J. J. Niedbalski, and R. L. Moroso, “Filaments in the sheath evolution of the dense plasma focus as applied to intense auroral observations,” *IEEE Transactions on Plasma Science*, vol. 35, no. 4, p. 808, 2007.
- [44] J. Feugeas and O. von Pamel, “Current distribution during the breakdown in a coaxial electrode system,” *Journal of Applied Physics*, vol. 66, no. 3, p. 1080, 1989.

- [45] A. I. Kleev and A. L. Velikovich, “Filamentation instabilities of dynamic z pinches and theta pinches,” *Plasma Physics and Controlled Fusion*, vol. 32, no. 10, p. 763, 1990.
- [46] B. Shokri, S. M. Khorashadi, and M. Dastmalchi, “Ion-acoustic filamentation of a current-driven plasma,” *Physics of Plasmas*, vol. 9, no. 8, p. 3355, 2002.
- [47] S. D. Grishin, A. K. Litvak, S. N. Ogorodnikov, and V. N. Stepanov, “Intermediate-power steady-state plasma accelerator,” *Soviet Physics Technical Physics*, vol. 22, pp. 280–283, February 1977.
- [48] L. Vainberg, G. Lyubimov, and G. Smolin, “High-current discharge effects and anode damage in an end-fire plasma accelerator,” *Soviet Physics Technical Physics*, vol. 23, pp. 439–443, April 1978.
- [49] J. M. Somerville, W. R. Blevin, and N. H. Fletcher, “Electrode Phenomena in Transient Arcs,” *Proceedings of the Physical Society of London Section B*, vol. 65, no. 396, p. 963, 1952.
- [50] J. M. Somerville and N. H. Fletcher, “Ring conduction in the early stages of sparks,” *British Journal of Applied Physics*, vol. 7, p. 419, November 1956.
- [51] J. M. Somerville and J. F. Williams, “The early stages of spark channel expansion,” *Proceedings of the Physical Society of London*, vol. 74, no. 3, p. 309, 1959.
- [52] J. M. Somerville and C. T. Grainger, “Current distribution in an expanding spark channel,” *British Journal of Applied Physics*, vol. 7, p. 109, 1956.
- [53] S. I. Drabkhina *Journal of Experimental and Theoretical Physics, U.S.S.R.*, vol. 21, p. 473, 1951.

- [54] S.-C. Lin, “Cylindrical shock waves produced by instantaneous energy release,” *Journal of Applied Physics*, vol. 25, no. 1, p. 54, 1954.
- [55] G. I. Taylor, “The formation of a blast wave by a very intense explosion,” *Proceedings of the Royal Society of London, Series A*, vol. 201, no. 1065, p. 159, 1950.
- [56] L. Uribarri and E. Y. Choueiri, “Relationship between anode spots and onset voltage hash in magnetoplasdynamic thrusters,” *Journal of Propulsion and Power*, vol. 24, no. 3, p. 571, 2008.
- [57] L. Rudolph, R. Jahn, K. Clark, and W. von Jaskowsky, “Performance Characteristics of Quasi-Steady MPD Discharges,” *AIAA International Electric Propulsion Conference*, no. AIAA 76-1000, 1976.
- [58] E. Y. Choueiri, A. J. Kelly, and R. G. Jahn, “The manifestation of Alfven’s hypothesis of critical ionization velocity in the performance of MPD thrusters,” *18th International Electric Propulsion Conference*, no. AIAA-85-2037, 1985.
- [59] H. Tahara, M. Sasaki, Y. Kagaya, and T. Yoshikawa, “Thruster performance and acceleration mechanisms of a quasi-steady applied-field MPD arcjet,” in *21st International Electric Propulsion Conference*, AIAA, July 18–20 1990.
- [60] C. Qing, L. Hong-bin, Z. Ming-ming, and L. Yan-bin, “Design and characteristics of two rogowski coils based on printed circuit board,” *IEEE Transactions on Instrumentation and Measurement*, vol. 55, pp. 939–943, June 2006.
- [61] L. A. Kojovic, “Pcb rogowski coil designs and performances for novel protective relaying,” in *Power Engineering Society General Meeting*, vol. 2, p. 614, IEEE, July 2003.

- [62] N. Karrer and P. Hofer-Noser, "Pcb rogowski coils for high di/dt current measurement," in *IEEE 31st Power Electronics Specialists Conference*, vol. 3, pp. 1296–1301, June 2000.
- [63] M. Argueso, G. Robles, and J. Sanz, "Implementation of a rogowski coil for the measurement of partial discharges," *Review of Scientific Instruments*, vol. 76, no. 6, p. 065107, 2005.
- [64] R. C. Webber, "Tutorial on beam current monitoring," in *American Institute of Physics Conference Series*, vol. 546, pp. 83–104, Nov. 2000.
- [65] E. S. Wright and R. G. Jahn, "Miniature rogowski coil probes for direct measurement of current density distributions in transient plasmas," *Review of Scientific Instruments*, vol. 36, no. 12, p. 1891, 1965.
- [66] D. D. Villani, *Energy Loss Mechanics in a MPD Arcjet*. PhD thesis, Princeton University, 1982.
- [67] M. Andrenucci, F. Paganucci, P. Grazzini, and F. Pupilli, "Scale and gemetric effects on the performance of MPD thrusters," in *AIAA 28th Joint Propulsion Conference*, July 1992.
- [68] H. Hugel, "Effect of self-magnetic forces on the anode mechanism of a high current discharge," *IEEE Transactions on Plasma Science*, vol. PS-8, December 1980.
- [69] H. Hugel, "Flow rate limitations in the self-field accelerator," *AIAA Journal*, vol. 12, pp. 1461–1462, November 1974.
- [70] R. Oberth and R. Jahn, "Anode phenomena in high-current accelerators," *AIAA Journal*, vol. 10, pp. 86–91, January 1972.

- [71] A. Korsun, “Current limiting by self magnetic field in a plasma accelerator,” *Soviet Physics Technical Physics*, vol. 19, pp. 124–126, July 1974.
- [72] K. Sankaran, *Simulation of Plasma Flows in Self-Field Lorentz Force Accelerators*. PhD thesis, Princeton University, 2005.
- [73] H. P. Wagner, H. J. Kaeppler, and M. Auweter-Kurtz, “Instabilities in MPD thruster flows: 2. investigation of drift and gradient driven instabilities using multi-fluid plasma models,” *Journal of Physics D*, vol. 31, p. 529, 1998.
- [74] F. Bonomo, P. Franz, G. Spizzo, L. Marrelli, P. Martin, F. Paganucci, P. Rosetti, M. Signori, M. Andrenucci, and N. Pomaro, “Ultraviolet tomography of kink dynamics in a magnetoplasma-dynamic thruster,” *Physics of Plasmas*, vol. 12, p. 093301, 2005.
- [75] M. Zuin, R. Cavazzana, E. Martines, G. Serianni, V. Antoni, and M. Bagatin, “Kink instability in applied-field magneto-plasma-dynamic thrusters,” *Physical Review Letters*, vol. 92, June 2004.
- [76] M. Zuin, M. Agostini, R. Cavazzana, E. Martines, P. Scarin, G. Serianni, V. Antoni, M. Bagatin, M. Andrenucci, F. Paganucci, P. Rossetti, and M. Signori, “Experimental investigation of magnetohydrodynamic instabilities in a magneto-plasma-dynamic thruster,” *Il Nuovo Cimento*, vol. 27C, pp. 449–466, September-October 2004.
- [77] F. Paganucci, F. Bonomo, and M. Zuin, “Further experimental evidences of the development of kink instabilities in MPD thrusters,” *AIAA Joint Propulsion Conference*, 2005.
- [78] J. Lawless, “Theory of Onset in Magnetoplasma-dynamic Thrusters,” *Journal of Propulsion and Power*, vol. 3, pp. 121–127, March/April 1987.

- [79] V. V. Subramaniam and J. L. Lawless, “Onset in magnetoplasmadynamic thrusters with finite rate ionization,” no. AIAA-87-1068, 1987.
- [80] V. V. Subramaniam, “Onset and erosion in self-field MPD thrusters,” no. AIAA-91-021, 1991.
- [81] H. O. Schrade, M. Auweter-Kurtz, and H. Kurtz, “Stability problems in magnetoplasmadynamik arc thrusters,” no. AIAA-85-1633, 1985.
- [82] H. Schrade, T. Wegmann, and T. Rosgen, “The onset phenomena explained by run-away joule heating,” *Proceedings of IEPC-1991*, no. 22, 1991.
- [83] W. A. Hoskins, “Asymmetric discharge patterns in the MPD thruster,” Master’s thesis, Princeton University, 1990.